

DEVELOPMENT OF CORE/SHELL STRUCTURED COMPOSITE  
NANOFIBERS VIA COAXIAL ELECTROSPINNING METHOD

A THESIS SUBMITTED TO  
THE GRADUATE SCHOOL OF NATURAL AND APPLIED SCIENCES  
OF  
MIDDLE EAST TECHNICAL UNIVERSITY

BY

REFİK BARIŞ YILMAZ

IN PARTIAL FULFILLMENT OF THE REQUIREMENTS  
FOR  
THE DEGREE OF MASTER OF SCIENCE  
IN  
CHEMICAL ENGINEERING

SEPTEMBER 2019



Approval of the thesis:

**DEVELOPMENT OF CORE/SHELL STRUCTURED COMPOSITE  
NANOFIBERS VIA COAXIAL ELECTROSPINNING METHOD**

submitted by **REFİK BARIŞ YILMAZ** in partial fulfillment of the requirements for  
the degree of **Master of Science in Chemical Engineering Department, Middle  
East Technical University** by,

Prof. Dr. Halil Kalıpçılar  
Dean, Graduate School of **Natural and Applied Sciences**

\_\_\_\_\_

Prof. Dr. Pınar Çalık  
Head of Department, **Chemical Engineering Dept.**

\_\_\_\_\_

Prof. Dr. Göknur Bayram  
Supervisor, **Chemical Engineering Dept., METU**

\_\_\_\_\_

Prof. Dr. Ülkü Yılmaz  
Co-Supervisor, **Chemical Engineering Dept., METU**

\_\_\_\_\_

**Examining Committee Members:**

Prof. Dr. Gülüm Şumnu  
Food Engineering Dept., METU

\_\_\_\_\_

Prof. Dr. Göknur Bayram  
Chemical Engineering Dept., METU

\_\_\_\_\_

Prof. Dr. Ülkü Yılmaz  
Chemical Engineering Dept., METU

\_\_\_\_\_

Assoc. Prof. Dr. İrem Erel Göktepe  
Chemistry Dept., METU

\_\_\_\_\_

Assoc. Prof. Dr. Ayşe Karakeçili  
Chemical Engineering Dept., Ankara University

\_\_\_\_\_

Date: 09.09.2019

**I hereby declare that all information in this document has been obtained and presented in accordance with academic rules and ethical conduct. I also declare that, as required by these rules and conduct, I have fully cited and referenced all material and results that are not original to this work.**

Name, Surname: Refik Barış Yılmaz

Signature:

## **ABSTRACT**

### **DEVELOPMENT OF CORE/SHELL STRUCTURED COMPOSITE NANOFIBERS VIA COAXIAL ELECTROSPINNING METHOD**

Yılmaz, Refik Barış  
Master of Science, Chemical Engineering  
Supervisor: Prof. Dr. Göknur Bayram  
Co-Supervisor: Prof. Dr. Ülkü Yilmazer

September 2019, 134 pages

Electrospinning being a versatile, fast and cost effective method in production of nanofibers, has been considered to be one of the most convenient processes for development of such fine morphologies. The method utilizes the electrostatic forces in developing fibrous morphologies out of polymer melts or solutions. Properties of the nanofiber morphology such as high mechanical stress distribution capability along the direction of alignment and high surface area to volume ratio have been the additional reasons behind the recent popularity of the electrospinning method both in academia and industry.

In this study, optimization of the coaxial electrospinning parameters for production of uniform structured neat core/shell nanofibers and investigation on the effects of halloysite nanotubes (HNTs) and piranha etched HNTs (HNT-P) on the properties of nanofibrous mats were aimed. Firstly, neat core/shell PEG/PA6 nanofibers were produced by changing the core/shell solution concentrations, applied electrical potential and solution feed rates. Morphology, thermal stability, heat storage, surface chemical composition and tensile properties of the nanofibrous mats were characterized by SEM, TGA, DSC, FTIR analyses and tensile testing.

Results revealed that with incorporation of 3 wt. % HNT-P into the core/shell nanofibers, tensile modulus and latent heat of melting values increased by 25% and 21%, respectively compared with the mentioned properties of neat core/shell nanofibrous samples. Moreover, with 3 wt. % HNT-P addition, melting enthalpy of PEG encapsulated in the core/shell nanofibers was increased from 68 J/g to 82 J/g with respect to neat core/shell nanofibers. Additionally, PEG encapsulation efficiency was increased from 78% to 96% with introduction of 3 wt. % HNT-P with respect to the sample without any additive. Finally, as a result of the thermal cyclic test, it was seen that neat, 3 wt. % HNT and HNT-P added nanofibrous samples preserved 88.11%, 93.36% and 92.83% of their initial melting enthalpies, respectively. These results revealed high thermal durability of the core/shell structured nanofibers.

Keywords: Nanocomposite, Coaxial Electrospinning, Polyamide-6, Poly(ethylene glycol), Halloysite Nanotubes, Phase Change Material

## ÖZ

### ÇEKİRDEK/KABUK YAPISINDAKİ KOMPOZİT NANOFİBERLERİN ORTAK EKSENLİ ELEKTROEĞİRME YÖNTEMİ İLE GELİŞTİRİLMESİ

Yılmaz, Refik Barış  
Yüksek Lisans, Kimya Mühendisliği  
Tez Danışmanı: Prof. Dr. Gökür Bayram  
Ortak Tez Danışmanı: Prof. Dr. Ülkü Yılmaz

Eylül 2019, 134 sayfa

Elektroeğirme yöntemi, nanofiberlerin üretiminde çok yönlü, hızlı ve uygun maliyetli bir proses olmasıyla nano boyutta morfolojiye sahip malzemelerin üretilmesinde kullanılan en elverişli metodlardan biri olarak düşünülmektedir. Bu metodda, polimer eriyiklerinden veya çözeltilerinden lifli morfolojilerin geliştirilmesinde elektrostatik kuvvetler kullanılmaktadır. Nanofiber morfolojisinin hizalama yönü boyunca yüksek mekanik gerilim dağıtım kabiliyeti ve yüksek yüzey alanı/hacim oranı gibi özellikleri, hem akademi hem de endüstride elektroeğirme yönteminin popülerliğinin arkasındaki en önemli nedenlerden olmuştur.

Bu çalışmada, düzenli yapılı çekirdek/kabuk yapısına sahip nanofiberlerin üretimi için ortak eksenli elektroeğirme parametrelerinin optimizasyonunun yanında haloysit nanotüplerin (HNT) ve piranha solüsyonu ile aşındırılmış HNT'lerin (HNT-P) eklenmesinin nanofiber dokumalarının özelliklerine olan etkilerinin araştırılması amaçlanmıştır. İlk olarak, çekirdek/kabuk yapılı PEG/PA6 nanofiberler, çözelti konsantrasyonları, elektrik potansiyeli ve çözelti besleme hızları değiştirilerek üretilmiştir. Elde edilen nanofiber dokumaların morfolojisi, ısıl dayanımı, ısı depolaması, yüzey kimyasal bileşimi ve çekme özellikleri SEM, TGA, DSC, FTIR analizleri ve çekme testi ile analiz edilmiştir.

Elde edilen sonuçlara göre, kütlece %3 aşındırılmış HNT'nin nanofiber yapısına eklenmesiyle üretilen malzemenin çekme modülü ve erime entalpisi katkısız çekirdek/kabuk yapıları nanofiberlere kıyasla %25 ve %21 artış göstermiştir. Ek olarak, kütlece %3 HNT-P ilavesiyle, çekirdek/kabuk yapıları nanofiberlerde enkapsüle edilmiş PEG'in erime entalpisi, HNT katkısız çekirdek/kabuk nanofiberlere göre 68 J/g'dan 82 J/g'a yükseltilmiştir. Ayrıca, PEG enkapsülasyon verimliliği, ağırlıkça % 3 HNT-P eklenmesiyle katkı maddesi içermeyen numuneye göre %78'den %96'ya çıkarılmıştır. Son olarak, ısı döngüsel test ile katkısız, kütlece %3 HNT ve %3 HNT-P katkıları numunelerin termal döngüsel test sonrasında başlangıçtaki erime entalpilerinin sırasıyla %88.11, %93.36 ve %92.83'lük bölümünü koruduğu görülmüştür. Bu sonuçlar çekirdek/kabuk yapıları nanofiberlerin yüksek ısı dayanıklılığını ortaya koymuştur.

Anahtar Kelimeler: Nanokompozit, Ortak Eksenli Elektroğirme, Polyamid-6, Poli(etilen glikol), Halosit Nanotüpler, Faz Değişim Malzemesi

To my beloved family...

## ACKNOWLEDGEMENTS

I wish to express my sincere gratitude to my supervisor Prof. Dr. Göknur Bayram for her guidance, never-ending support, and help throughout this study, being closely interested in every phase of my thesis work. Her advices contributed not only my academic improvement but also personal life.

I want to thank my co-advisor Prof. Dr. Ülkü Yılmaz for his valuable comments and critics during this M.Sc. thesis.

This thesis would not have been accomplished without my kindhearted friends in Polymer Engineering Laboratory. I want to thank Selin Şahin, Berrak Erkmen and Merve Özkutlu, for their endless support and friendship.

Middle East Technical University Research Fund Project (YLT-304-2018-3577) and Scientific and Technical Research Council of Turkey (TÜBİTAK) (Project No: 315M018, BİDEP 2210-C) are greatly acknowledged for financial support.

Last but not least I would like to deeply thank my big family for always being there for me. A special thanks goes to Kemal Ege Yılmaz, Ayşen Yılmaz and Gürkan Atıncı Yılmaz who always encouraged and comfort me. It would not be possible without their support. My special thanks go to İrem Demir, for always being there enlightening my life in the darkest days with her endless love and compassion.

## TABLE OF CONTENTS

ABSTRACT .....	v
ÖZ.....	vii
ACKNOWLEDGEMENTS .....	x
TABLE OF CONTENTS .....	xi
LIST OF TABLES .....	xv
LIST OF FIGURES .....	xvii
LIST OF ABBREVIATIONS .....	xxii
CHAPTERS	
1. INTRODUCTION .....	1
2. BACKGROUND .....	5
2.1. Nanofibers .....	5
2.2. Electrospinning.....	5
2.2.1. Uniaxial Electrospinning .....	8
2.2.2. Coaxial Electrospinning.....	9
2.2.3. Multifluidic Electrospinning.....	10
2.3. Thermal Energy Storage (TES) Materials.....	11
2.3.1. Sensible Heat Storage .....	11
2.3.2. Latent Heat Storage .....	13
2.3.3. Thermo-Chemical Heat Storage .....	15
2.4. Thermal Energy Storage Materials by PCM Encapsulation.....	16

2.4.1. Chemical Micro/Nano Encapsulation Methods .....	17
2.4.1.1. In-Situ Polymerization .....	17
2.4.2. Physical Micro/Nano Encapsulation Methods.....	19
2.4.2.1. Physico-Chemical Methods.....	19
2.4.2.2. Physico-Mechanical Methods .....	20
2.5. Coaxial Electrospinning Parameters.....	24
2.6. Composite Nanofibers .....	26
2.7. The Scope of the Thesis.....	28
<b>3. EXPERIMENTAL.....</b>	<b>31</b>
3.1. Materials .....	31
3.1.1. Polyamide-6 (PA6) .....	31
3.1.2. Poly(ethylene glycol) (PEG).....	31
3.1.3. Halloysite Nanotubes (HNTs).....	32
3.1.4. Solvents.....	32
3.2. Experimental Method .....	32
3.2.1. Preparation of Polymer Solutions .....	32
3.2.1.1. Preparation of Shell Solution .....	32
3.2.1.2. Preparation of Core Solution.....	33
3.2.2. Activation of HNTs by Piranha Etching .....	34
3.2.3. Calculation of the PEG/PA6 Weight Ratio in the Nanofiber Mats .....	34
3.2.3.1. Preparation of PEG/HNTs Composite Solution.....	36
3.2.4. Coaxial Electrospinning Process.....	37
3.3. Characterization Methods.....	39
3.3.1. Scanning Electron Microscopy (SEM) Analysis .....	39

3.3.2. Transmission Electron Microscopy (TEM) Analysis .....	39
3.3.3. Fourier Transformed Infrared (FTIR) Spectroscopy .....	39
3.3.4. Thermogravimetric Analysis (TGA) .....	39
3.3.5. Differential Scanning Calorimetry (DSC) Analysis .....	40
3.3.6. X-Ray Powder Diffraction Analysis (XRD).....	40
3.3.7. Tensile Test.....	40
3.3.8. Thermal Cyclic Test.....	42
4. RESULTS AND DISCUSSION .....	45
4.1. Optimization of the Electrospinning Process Parameters .....	45
4.1.1. Preliminary Studies.....	45
4.1.2. Solution Concentration Optimization.....	49
4.1.2.1. Scanning Electron Microscopy (SEM) Analysis .....	50
4.1.2.2. Thermogravimetric Analysis (TGA).....	58
4.1.2.3. Differential Scanning Calorimetry (DSC) Analysis .....	59
4.1.2.4. Fourier Transform Infrared (FTIR) Spectroscopy .....	61
4.1.3. Applied Electrical Potential Optimization.....	63
4.1.3.1. Scanning Electron Microscopy (SEM) Analysis .....	64
4.1.3.2. Thermogravimetric Analysis (TGA).....	67
4.1.3.3. Differential Scanning Calorimetry (DSC) Analysis .....	68
4.1.3.4. Fourier Transform Infrared Spectroscopy (FTIR) Analysis .....	70
4.1.4. Feed Rate Optimization .....	72
4.1.4.1. Scanning Electron Microscopy (SEM) Analysis .....	72
4.1.4.2. Thermogravimetric Analysis (TGA).....	77
4.1.4.3. Differential Scanning Calorimetry (DSC) Analysis .....	79

4.1.4.4. Fourier Transform Infrared Spectroscopy (FTIR) Analysis .....	80
4.2. Development of Composite Core/Shell Nanofibers .....	83
4.3. Characterization of HNTs.....	83
4.3.1. Scanning Electron Microscopy (SEM) Analysis .....	86
4.3.2. Thermogravimetric Analysis (TGA).....	100
4.3.3. Differential Scanning Calorimetry (DSC) Analysis .....	103
4.3.4. Fourier Transform Infrared Spectroscopy (FTIR) Analysis .....	105
4.3.5. Tensile Test Results .....	108
4.3.6. Thermal Cyclic Test.....	112
5. CONCLUSIONS.....	117
REFERENCES.....	118
APPENDICES	
A. THERMAL CYCLIC TEST GRAPHS.....	129
B. FREQUENCY DISTRIBUTION GRAPHS .....	131
C. TENSILE TEST RESULTS .....	134

## LIST OF TABLES

### TABLES

Table 1. Some of the widely used sensible heat storage materials [21].....	12
Table 2. Microencapsulation methods with corresponding average particle size ranges [29].....	22
Table 3. The Properties of PA6 [56]. .....	31
Table 4. The Properties of PEG 6000 [57].....	31
Table 5. The Properties of HNTs [58]. .....	32
Table 6. (PEG:PA6) mass ratio data of nanofibrous samples produced by using different solution concentrations.....	36
Table 7. Technical specifications of Inovenso NE300 electrospinning device. ....	38
Table 8. Parameters of the coaxial electrospinning process. ....	38
Table 9. Decomposition temperature data of the samples produced by using different solution concentrations (AEP: 24 kV, TCD: 10 cm, SFR: 0.1/0.3 ml/h, CT: plate, ED: 30 min). .....	59
Table 10. DSC data of neat PEG and coaxially electrospun nanofibers from different core solution concentrations (AEP: 24 kV, TCD: 10 cm, SFR: 0.1/0.3 ml/h, CT: plate, ED: 30 min).....	61
Table 11. Characteristic FTIR peaks of PA6 and PEG [65, 66, 67]. .....	63
Table 12. Decomposition temperatures of samples produced under 20, 24 and 28 kV of applied electrical potentials (SC: 30 wt. % PEG/12 wt. % PA6, TCD: 10 cm, SFR: 0.1/0.3 ml/h, CT: plate, ED: 30 min). .....	68
Table 13. DSC data of electrospun samples produced under 20, 24 and 28 kV of applied electrical potentials (SC: 30 wt. % PEG/12 wt. % PA6, TCD: 10 cm, SFR: 0.1/0.3 ml/h, CT: plate, ED: 30 min). .....	69

Table 14. Decomposition temperatures of nanofibrous samples electrospun using different core/shell solution feed rates (SC: 30 wt. % PEG/12 wt. % PA6, AEP: 24 kV, TCD: 10 cm, .....	78
Table 15. DSC data of the samples electrospun using different core/shell solution feed rates .....	80
Table 16. Decomposition temperature of nanofibrous samples containing different amounts of HNTs (SC: 30 wt. % PEG/12 wt. % PA6, AEP: 24 kV, TCD: 10 cm, SFR: 0.1/0.35 ml/h, .....	102
Table 17. DSC data of the nanofibrous samples containing different amounts of HNTs and HNT-P (SC: 30 wt. % PEG/12 wt. % PA6, AEP: 24 kV, TCD: 10 cm, SFR: 0.1/0.35 ml/h, .....	105
Table 18. Thermal cyclic test data of neat core/shell nanofibrous sample .....	113
Table 19. Thermal cyclic test data of the 3 wt. % HNT added core/shell structured nanofibrous sample (SC: 30 wt. % PEG/12 wt. % PA6, AEP: 24 kV, TCD: 10 cm, SFR: 0.1/0.35 ml/h, .....	114
Table 20. Thermal cyclic test data of the 3 wt. % HNT-P added core/shell structured nanofibrous sample (SC: 30 wt. % PEG/12 wt. % PA6, AEP: 24 kV, TCD: 10 cm, SFR: 0.1/0.35 ml/h, .....	115

## LIST OF FIGURES

### FIGURES

Figure 1. Illustration of a) uniaxial electrospinning, b) coaxial electrospinning and c) multifluidic electrospinning setups [3]. .....	6
Figure 2. Schematic representation of bottom-up electrospinning setup.....	7
Figure 3. Forces acting on a Taylor cone in bottom- up coaxial electrospinning.....	8
Figure 4. Classification of fibers [15]. .....	9
Figure 5. Representation of the steps of the coacervation method. a) Dispersion of core material in water solution, b) addition of hydrophilic polymer, c) complex formation between the core material and the shell material, d) coacervation of the polymer. ...	20
Figure 6. Schematic representation of coextrusion method. ....	21
Figure 7. Experimental procedure for the preparation of the PA6 solution.....	33
Figure 8. Experimental procedure for the preparation of PEG solution. ....	34
Figure 9. Experimental procedure for the preparation of PEG/HNTs solution. ....	37
Figure 10. Shimadzu Autograph AG-IS 100kN universal testing machine.....	41
Figure 11. SEM micrographs of electrospun neat PEG with concentrations of a) 10, b) 15, c) 25 and d) 40 wt. % (AEP: 24 kV, TCD: 10 cm, SFR: 0.33 ml/h, CT: cylinder, RS: 200 rpm, ED: 30 min). .....	46
Figure 12. SEM micrographs of coaxially electrospun PEG/PA6 nanofibers with a) 20000x and b) 100000x magnifications (SC: 40 wt. % PEG/10 wt. % PA6, .....	49
Figure 13. TEM images of coaxially electrospun PEG/PA6 nanofibers (SC: 40 wt. % PEG/10 wt. % PA6, AEP: 24 kV, TCD: 10 cm, SFR: 0.3/0.9 ml/h, CT: cylinder, RS: 200 rpm, ED: 3 sec). .....	49
Figure 14. SEM micrographs of nanofibers electrospun with 12 wt. % PA6 in the shell solution and a) 30 wt. %, b) 40 wt. % and c) 50 wt. % PEG in the core solution (AEP: 24 kV, TCD: 10 cm, SFR: 0.1/0.3 ml/h, CT: plate, ED: 1 h). .....	51
Figure 15. SEM micrographs of nanofibers electrospun by using solutions with 30 wt. % PEG core and a) 10 wt. %, b) 12 wt. %, c) 15 wt. % PA6 concentrations (AEP: 24 kV, TCD: 10 cm, SFR: 0.1/0.3 ml/h, CT: plate, ED: 1 h). .....	54

Figure 16. SEM micrographs of nanofibers electrospun by using solutions with 40 wt. % PEG core and a) 10 wt. %, b) 12 wt. %, c) 15 wt. % PA6 concentrations (AEP: 24 kV, TCD: 10 cm, SFR: 0.1/0.3 ml/h, CT: plate, ED: 1 h)..... 55

Figure 17. SEM micrographs of nanofibers electrospun by using solutions with 50 wt. % PEG core and a) 10 wt. %, b) 12 wt. %, c) 15 wt. % PA6 concentrations. (AEP: 24 kV, TCD: 10 cm, SFR: 0.1/0.3 ml/h, CT: plate, ED: 1 h)..... 56

Figure 18. Bar chart depicting the average fiber diameters of the nanofibers produced from different electrospinning solutions (AEP: 24 kV, TCD: 10 cm, SFR: 0.1/0.3 ml/h, CT: plate)..... 57

Figure 19. TGA curves of nanofibers produced by coaxial electrospinning with different core solution concentrations (AEP: 24 kV, TCD: 10 cm, SFR: 0.1/0.3 ml/h, CT: plate, ED: 30 min). ..... 59

Figure 20. a) FTIR spectra and b) zoomed FTIR spectra of neat PA6 fibers, PEG flakes and electrospun samples by using 30, 40, 50 wt. % PEG in the core solution and 12 wt. % PA6 in the shell solution (AEP: 24 kV, TCD: 10 cm, SFR: 0.1/0.3 ml/h, CT: plate, ED: 30 min). ..... 62

Figure 21. SEM micrographs of electrospun nanofibers under a-b) 20 kV, c-d) 24 kV, e-f) 28 kV electrical potential difference with 2500x and 20000x magnifications, respectively..... 65

Figure 22. Bar chart depicting the diameter distribution of the nanofibers produced under 20, 24 and 28 kV of applied electrical potentials..... 66

Figure 23. TGA graph of samples produced under 20, 24 and 28 kV of applied electrical potentials with 30 wt. % PEG/ 12 wt. % PA6 core/shell solution concentrations..... 68

Figure 24. FTIR spectra of electrospun samples produced under 20, 24 and 28 kV of applied electrical potentials (SC: 30 wt. % PEG/12 wt. % PA6, TCD: 10 cm, SFR: 0.1/0.3 ml/h, CT: plate, ED: 30 min). ..... 71

Figure 25. Zoomed FTIR spectra of electrospun samples produced under 20, 24 and 28 kV of applied electrical potentials (SC: 30 wt. % PEG/12 wt. % PA6, TCD: 10 cm, SFR: 0.1/0.3 ml/h, CT: plate, ED: 30 min). ..... 71

Figure 26. SEM micrographs of samples produced with 0.1 ml/h PEG solution feed rate and.....	74
Figure 27. SEM micrographs of samples produced with 0.3 ml/h PA6 solution feed rate and.....	76
Figure 28. Bar chart depicting the average fiber diameter of nanofibrous samples electrospun using different solution feed rates (SC: 30 wt. % PEG/12 wt. % PA6, AEP: 24 kV, TCD: 10 cm, CT: plate, ED: 30 min).....	77
Figure 29. TGA data of nanofibrous samples produced using different core/shell solution feed rates using different solution feed rates (SC: 30 wt. % PEG/12 wt. % PA6, AEP: 24 kV, TCD: 10 cm,.....	78
Figure 30. FTIR spectra of nanofibrous samples produced by using different feed..	81
Figure 31. Zoomed FTIR spectra of nanofibrous samples produced by using different feed rates .....	82
Figure 32. Zoomed FTIR spectra of nanofibrous samples produced by using different feed rates (SC: 30 wt. % PEG/12 wt. % PA6, AEP: 24 kV, TCD: 10 cm, CT plate, ED: 30 min).....	82
Figure 33. XRD patterns of dried HNTs and piranha etched HNTs (HNT-P). .....	85
Figure 34. TGA curves of dried HNTs and piranha etched HNTs (HNT-P).....	85
Figure 35. FTIR spectra of dried HNTs and piranha etched HNTs (HNT-P).....	86
Figure 36. SEM micrographs of neat PA6 fibers with a) 2500x and b) 20000x magnifications .....	88
Figure 37. SEM micrographs of neat PEG/PA6 coreshell nanofibers with a) 2500x and b) 20000x magnifications (SC: 30 wt. % PEG/12 wt. % PA6, AEP: 24 kV, TCD: 10 cm, SFR: 0.1/0.35 ml/h, .....	88
Figure 38. SEM micrographs with magnifications a) 2500x, b) 20000x and c) 50000x of composite nanofibers containing 0.5 wt. % HNT (SC: 30 wt. % PEG/12 wt. % PA6, AEP: 24 kV, TCD: 10 cm, SFR: 0.1/0.35 ml/h, CT: cylinder, RS: 100 rpm, ED: 2 h). .....	89
Figure 39. SEM micrographs with magnifications a) 2500x, b) 20000x and c) 40000x of composite nanofibers containing 1 wt. % HNT (SC: 30 wt. % PEG/12 wt. % PA6,	

AEP: 24 kV, TCD: 10 cm, SFR: 0.1/0.35 ml/h, CT: cylinder, RS: 100 rpm, ED: 2 h). .....	90
Figure 40. SEM micrographs with magnifications a) 2500x, b) 20000x and c) 100000x of composite nanofibers containing 3 wt. % HNT (SC: 30 wt. % PEG/12 wt. % PA6, AEP: 24 kV, TCD: 10 cm, SFR: 0.1/0.35 ml/h, CT: cylinder, RS: 100 rpm, ED: 2 h). .....	92
Figure 41. SEM micrographs with magnifications a) 2500x, b) 20000x and c) 200000x of composite nanofibers containing 5 wt. % HNT (SC: 30 wt. % PEG/12 wt. % PA6, AEP: 24 kV, TCD: 10 cm, SFR: 0.1/0.35 ml/h, CT: cylinder, RS: 100 rpm, ED: 2 h). .....	93
Figure 42. SEM micrographs with magnifications a) 2500x, b) 20000x and c) 50000x of composite nanofibers containing 0.5 wt. % HNT-P (SC: 30 wt. % PEG/12 wt. % PA6, AEP: 24 kV, TCD: 10 cm, SFR: 0.1/0.35 ml/h, CT: cylinder, RS: 100 rpm, ED: 2 h).....	96
Figure 43. SEM micrographs with magnifications a) 2500x, b) 20000x and c) 100000x of composite nanofibers containing 1 wt. % HNT-P (SC: 30 wt. % PEG/12 wt. % PA6, AEP: 24 kV, TCD: 10 cm, SFR: 0.1/0.35 ml/h, CT: cylinder, RS: 100 rpm, ED: 2 h). .....	97
Figure 44. SEM micrographs with magnifications a) 2500x, b) 20000x and c) 100000x of composite nanofibers containing 3 wt. % HNT-P (SC: 30 wt. % PEG/12 wt. % PA6, AEP: 24 kV, TCD: 10 cm, SFR: 0.1/0.35 ml/h, CT: cylinder, RS: 100 rpm, ED: 2 h). .....	98
Figure 45. SEM micrographs with magnifications a) 2500x, b) 20000x and c-d) 100000x of composite nanofibers containing 5 wt. % HNT-P (SC: 30 wt. % PEG/12 wt. % PA6, AEP: 24 kV, TCD: 10 cm, SFR: 0.1/0.35 ml/h, CT: cylinder, RS: 100 rpm, ED: 2 h). .....	99
Figure 46. Bar chart depicting the average fiber diameter values of HNT and HNT-P added composite nanofibrous samples (SC: 30 wt. % PEG/12 wt. % PA6, AEP: 24 kV, TCD: 10 cm, .....	100

Figure 47. TGA curves of electrospun samples containing different amounts of HNTs .....	101
Figure 48. TGA curves of electrospun samples containing different amounts of ...	102
Figure 49. FTIR spectra of HNTs added composite nanofibrous samples .....	106
Figure 50. Zoomed FTIR spectra of HNTs added composite nanofibrous samples	107
Figure 51. FTIR spectra of HNT-P added composite nanofibrous samples .....	107
Figure 52. Zoomed FTIR spectra of HNT-P added composite nanofibrous samples .....	108
Figure 53. Bar chart depicting the tensile strength values of the electrospun nanofibrous samples.....	109
Figure 54. Bar chart depicting the tensile modulus values of the electrospun nanofibrous samples.....	110
Figure 55. Bar chart depicting the elongation at break values of the electrospun nanofibrous samples (SC: 30 wt. % PEG/12 wt. % PA6, AEP: 24 kV, TCD: 10 cm, SFR: 0.1/0.35 ml/h, CT: cylinder,.....	111
Figure 56. DSC curves of the neat core/shell structured nanofibrous sample during 1 <sup>st</sup> and 10 <sup>th</sup> heating (SC: 30 wt. % PEG/12 wt. % PA6, AEP: 24 kV, TCD: 10 cm, SFR: 0.1/0.35 ml/h, .....	114
Figure 57. DSC curves of 3 wt. % HNT added core/shell structured nanofibrous sample during 1 <sup>st</sup> and 10 <sup>th</sup> heating (SC: 30 wt. % PEG/12 wt. % PA6, AEP: 24 kV, TCD: 10 cm, SFR: 0.1/0.35 ml/h, .....	115
Figure 58. DSC curves of 3 wt. % HNT added core/shell structured nanofibrous sample during 1 <sup>st</sup> and 10 <sup>th</sup> heating (SC: 30 wt. % PEG/12 wt. % PA6, AEP: 24 kV, TCD: 10 cm,.....	116

## LIST OF ABBREVIATIONS

AED	Applied electrical potential, kV
CA	Cellulose acetate
CT	Collector type
DSC	Differential scanning calorimetry
ED	Electrospinning Duration, sec, min or h
FTIR	Fourier transform infrared spectroscopy
HNT-P	Piranha etched halloysite nanotubes
HNTs	Halloysite nanotubes
MEPCMs	Micro encapsulated phase change materials
NEPCM	Nano encapsulated phase change material
PA6	Polyamide 6
PCMs	Phase change materials
PEG	Poly(ethylene glycol)
PGA	Poly(glycolic acid)
PLA	Poly(lactic acid)
PVA	Poly(vinyl alcohol)
RS	Rotational speed, rpm
SC	Solution concentration, wt. %
SEM	Scanning electron microscopy
SFR	Solution feed rates, ml/h

TCD	Tip to collector distance, cm
TEM	Transmission electron microscopy
TES	Thermal energy storage
TGA	Thermal gravimetric analysis
wt.	Weight
XRD	X-Ray Diffraction



## **CHAPTER 1**

### **INTRODUCTION**

Electrospinning is a versatile, fast and cost effective method in production of nanofibers which utilizes the electrostatic forces in developing fibrous morphologies out of polymer melts or solutions. The versatility, cost effectiveness and applicability in industrial scales make electrospinning a superior method in production of nanofibrous morphologies than other methods such as drawing, template-based synthesis and self-assembly [1]. Advantageous properties of the nanofiber morphology such as high mechanical stress distribution capability along the direction of alignment and high surface area to volume ratio are some of the reasons behind the recent popularity of the electrospinning method both in academia and industry.

Electrospinning method utilizes the electrostatic forces resulting from electrical potential difference between the polymer melt or solution and the collector for development of nanofibrous morphology. In the case of polymer melt electrospinning, nanofiber-shaped polymer solidifies as it cools on the collector surface while in polymer solution electrospinning the polymer stabilizes its fibrous shape after the removal of the solvent by evaporation during the process. Important factors that contribute to electrospinnability are the molecular weight of the polymer and the conductivity of the polymer solution since integrity and formability of the fibrous morphology are determined by such parameters [2].

In terms of the complexity of the produced nanofiber structure, the production method can be categorized as uniaxial, coaxial or multifluidic electrospinning. While uniaxial electrospinning can be regarded as the method of producing nanofibers from a single polymer solution constituting the whole nanofiber structure, in coaxial electrospinning two different polymer solutions are electrospun concentrically having one polymer as the core structure and the other as the shell. On the other hand, in multifluidic

electrospinning even more sophisticated morphologies are produced by introducing more than two polymeric materials in a single nanofiber structure [3].

Coaxial electrospinning has three main types of factors affecting the produced fiber morphology such as process, solution and ambient parameters. Process parameters are applied electrical potential difference between the spinneret and the collector, needle tip to collector distance and collector rotation speed for the cases in which cylindrical collector is used. The solution parameters on the other hand can be mentioned as electrospinning solution concentration, solution conductivity and feed rate. Since two distinct polymer solutions are utilized in coaxial electrospinning, the number of solution parameters naturally increases. Finally, the ambient parameters that affect the produced fiber morphology, process stability and efficiency are relative humidity and temperature of the process medium. In order to obtain uniform nanofiber structures with a stable and efficient electrospinning process, optimization of these parameters are crucial [4].

Phase change materials (PCMs) have the ability of storing thermal energy in the form of latent heat during melting owing to their high melting enthalpy values. At the same time, they possess the ability of releasing significant amount of energy during liquid to solid phase transition. These properties of the phase change materials have been attracting high interest especially in the field of thermal energy storage materials but since the material becomes liquid as it melts the storage and handling pose an important problem. Coaxial electrospinning is one of the most advantageous methods for encapsulating PCMs by using polymeric materials as the shell structure since high surface to volume ratio of nanofibers further enhance the thermal energy storage property by increasing heat transfer rate [3].

In electrospinning many types of materials such as organic and synthetic polymers can be utilized and polyamide 6 (PA6) is one of the engineering polymers that has been widely studied in electrospinning applications in recent years [5, 6]. The reason behind the preference of PA6 as the building material of nanofibrous morphologies is the

superior mechanical properties of PA6 such as tensile strength [7]. On the other hand, poly(ethylene glycol) (PEG) is a bio-compatible and highly promising phase change material having high melting-solidifying enthalpy at temperatures ranging between 4-60°C depending on the molecular weight. Being a polyol, PEG has been used in many areas such as pharmaceutical in toothpastes, medicines or skin creams due to its biologically inert property. More importantly, PEG being a semi-crystalline polymer, possesses a very significant amount of melting-freezing enthalpy making it highly useful as a phase change material. On the other hand, halloysite nanotubes (HNTs) are naturally occurring inorganic nanoclay materials comprised of Si, Al and O elements. They may have several morphologies such as tubular, platy or spherical forms. The nanostructure and unique morphology supplies HNTs high surface areas resulting in many possible areas of utilization such as drug release and catalysis. In addition, HNTs are being widely used as polymer additives due to their unique thermal properties and morphologies [8-10].

In this thesis, firstly, optimization of the coaxial electrospinning process parameters such as solution concentration, applied electrical potential difference and solution feed rate for development of core/shell structured nanofibers from PEG/PA6 materials was done. In the process of developing stable coaxial electrospinning process for production of uniform nanofibers, thermal, chemical properties and morphologies were characterized by Thermogravimetric Analysis (TGA), Differential Scanning calorimetry (DSC), Fourier Transform Infrared Spectroscopy (FTIR) and Scanning Electron Microscopy (SEM) methods. With addition of HNTs into the core structure, development of multifunctional properties of nanofibers such as mechanical and thermal energy storage characteristics were aimed. Different HNTs additive amounts in PEG such as 0.5, 1.0, 3.0, and 5.0 wt. % were tested and piranha etching onto the HNTs surfaces with the aim of increasing interaction between nano additive and PEG was done. There are studies about development of PEG/PA6 core/shell nanofibers by using coaxial electrospinning but there has been absence of research on introduction

of HNTs into the core/shell nanofibers with the aim of enhancing the mechanical and thermal energy storage properties in the literature [11, 12].

## CHAPTER 2

### BACKGROUND

#### 2.1. Nanofibers

Fibers are one dimensional morphologies with characteristic structural features such as high length to cross-sectional diameter ratio. In further enhancing this characteristic, decreasing the fiber diameter to nanometer scale has been seen to be extremely beneficial. To that end, there have been many methods developed for production of nanofibers such as self-assembly, template-based synthesis, solution blow spinning, centrifugal jet spinning and electrospinning [12]. Having high length to cross-sectional diameter ratio, nanofibers possess several outstanding properties such as high specific surface area, high surface area to volume ratio and ability of forming highly interconnected mesh structure. Owing to their advantageous properties and encouraging potential, nanofibers have been developed from many materials such as natural polymers, synthetic polymers, semi-conducting nanomaterials and carbon based nanomaterials [12]. At first being only commercialized for filtration applications, with increasing raw material options and mechanical properties, nanofibers have been used as protective textiles, reinforcement in composite materials, energy storage materials, wound dressing materials and drug delivery systems [1].

#### 2.2. Electrospinning

Among many nanofiber production methods such as drawing, template-based synthesis and self-assembly technique, electrospinning has gained increasing attention since 1990s due to its versatility, simplicity, producibility of continuous fibers and cost effectiveness [1]. A basic electrospinning method consists of a syringe where solution is kept, a needle where material is fed to the system, a pump being used for controlling the material feeding strategy and a collector. In this method, the polymer solution or

melt with certain amount of conductivity is fed to the needle where it is subjected to an electrical potential difference. Having needle charged with electrical voltage and collector being grounded, the polymer solution is subjected to certain level of electrostatic force which drives the material into a conical shape (Taylor cone) and when the critical voltage is exceeded that is necessary to overcome the surface tension of the solution, nanofibrous structure forms on the collector. In terms of the resulting nanofiber structure, electrospinning can be categorized into three classes such as uniaxial, coaxial and multifluidic electrospinning. The schematic representation of the three different electrospinning setups can be seen in Figure 1. Uniaxial electrospinning can be regarded as the standard production of nanofibers from a single material whereas in coaxial electrospinning core/shell structured nanofibers can be produced by using two different materials. Multifluidic electrospinning on the other hand can be acknowledged as an even more sophisticated method in which more than two materials are used in production of complex structured nanofibers [3].

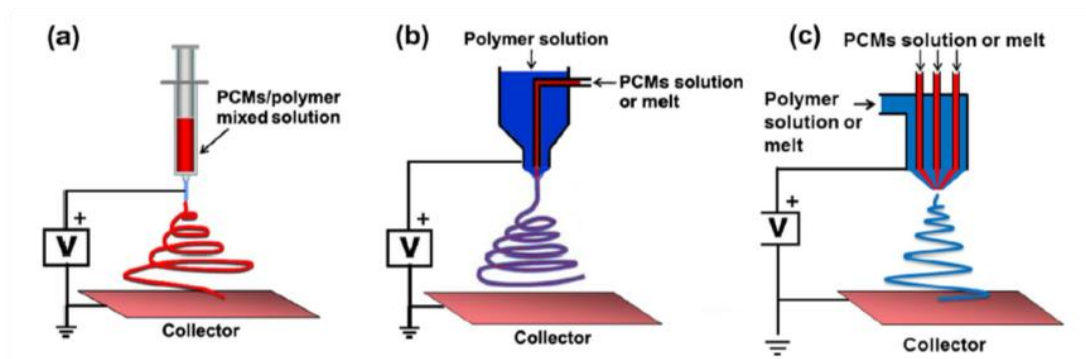
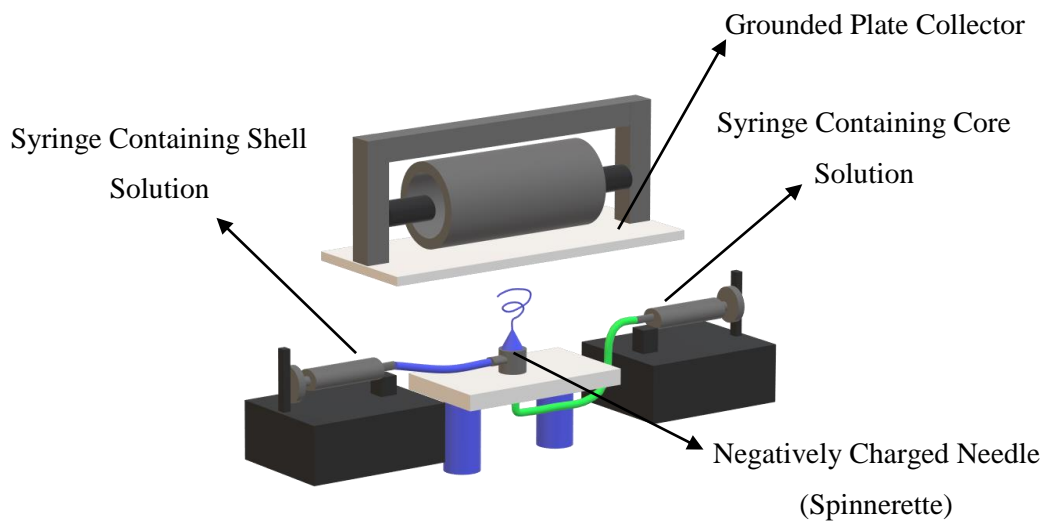


Figure 1. Illustration of a) uniaxial electrospinning, b) coaxial electrospinning and c) multifluidic electrospinning setups [3].

There have been several different electrospinning configurations in the literature having different needle-collector orientations such as horizontal, vertical and bottom-up which indicate the electrospinning direction. In the case of bottom-up electrospinning the polymer solution acts under the effect of four forces. Electrostatic

force acts in the direction of the electrical potential difference and stretches the polymer into the desired morphology whereas gravitational force, interfacial tension and viscoelastic force act in the opposite direction preventing the stretching motion of the solution. The Taylor cone under the influence of four forces can be seen in Figure 3. In coaxial electrospinning under the influence of electrical potential difference, the negative ions in the solutions accumulate on the outer surface of the outer solution. Thus no electrostatic force is applied to the inner solution, but due to the surface tension between the inner and outer solutions a drag force is utilized in the collection of the inner solution while outer solution is pulled towards the collector by electrostatic force [13].



*Figure 2.* Schematic representation of bottom-up electrospinning setup.

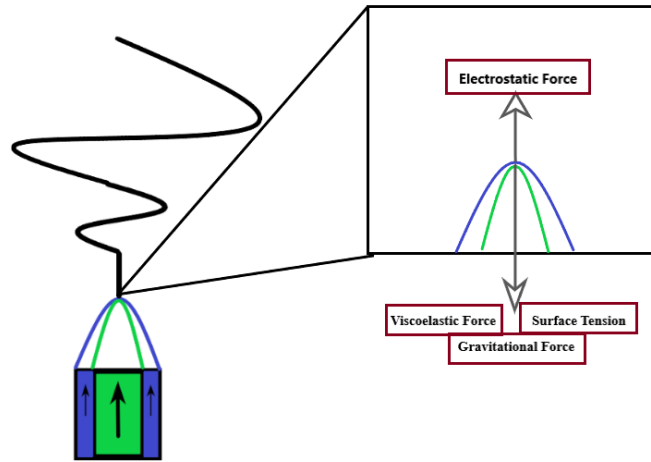


Figure 3. Forces acting on a Taylor cone in bottom- up coaxial electrospinning.

The parameters of electrospinning method can be divided into three main sections that are process, solution and ambient parameters. Process parameters can be mentioned as electrical voltage, solution feed rate, needle to collector distance and collector type whereas solution parameters are solution concentration, conductivity, viscosity and surface tension. The ambient parameters on the other hand are ambient temperature and relative humidity [4]. In coaxial electrospinning, number of solution parameters are duplicated as two solution systems are present.

### 2.2.1. Uniaxial Electrospinning

Nanofiber is a one dimensional structure having very high length to diameter ratio with respect to other nano materials such as zero dimensional nanoparticles, quantum dots or two dimensional sheets. Having outstanding properties such as high surface to volume ratio and ability to form highly interconnected mesh structure, nanofibers have many advanced applications in areas such as electronics, protective clothing, reinforcement composites and regenerative medicine [14].

Uniaxial electrospinning is one of the most widely used nanofiber production methods in recent years both in industry and academia due to the high versatility, cost

effectiveness and simplicity. A single material either dissolved in a solvent or melted is shaped into nanofiber morphology by using electrostatic effect as the driving force. As the free charges in the polymer solution or melt are subjected to electrostatic forces induced due to electrical potential difference between charged solution and grounded collector, the formation of nanofibrous structure occurs [15]. There are several types of materials either organic or synthetic that have been used for production of nanofibers via uniaxial electrospinning. The classification of the fibers with respect to the type of their raw materials can be seen in Figure 4.

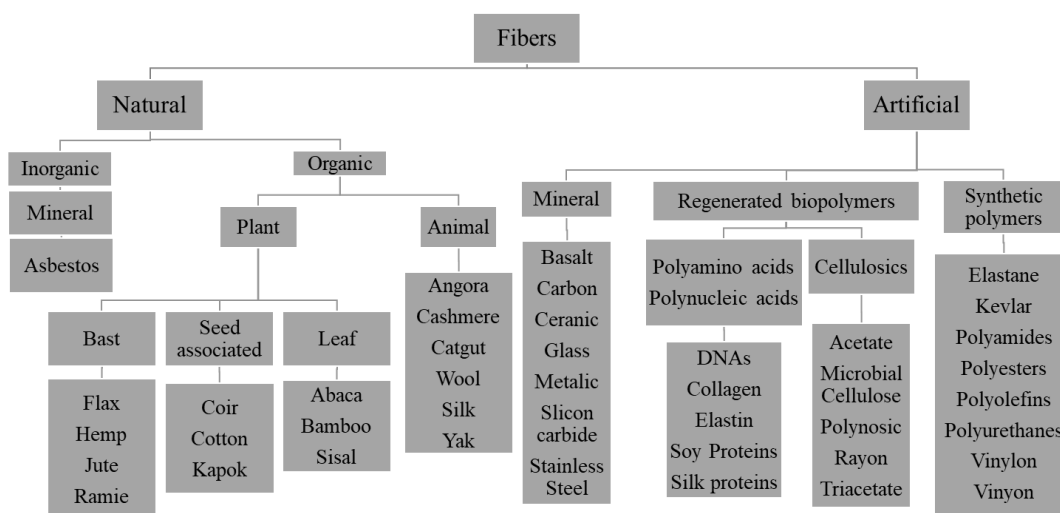


Figure 4. Classification of fibers [15].

### 2.2.2. Coaxial Electrospinning

In coaxial electrospinning, two polymeric materials are fed to a needle having coaxially adjusted concentric tubes. Through this method, formation of ultrafine nanofiber structures by using two different materials as the building blocks is enabled. This leads nanofibrous morphology towards many new potential applications such as energy storage materials, controlled drug releasing agents and self-healing structures.

In contrast to uniaxial electrospinning, the presence of two different materials in the needle tip also results in differences in terms of Taylor Cone formation. In uniaxial electrospinning, Taylor Cone forms at the needle tip as the free charges in the polymer solution accumulates on the outer surface due to the electrical potential difference between the solution and the collector. But in the coaxial electrospinning method although two solutions reside at the needle tip concentrically, all the free charges in both solutions accumulate on the outer surface of the shell solution during the fiber production process. This means that the inner solution does not experience any force resulting from the electrical potential difference but as the shell solution acts under the stretching effect of electrostatic force it induces drag force to the inner solution [13]. Owing to this property of coaxial electrospinning, even non-spinnable materials due to lack of sufficient conductivity and molecular entanglements can also be used as the core material in nanofiber production.

### **2.2.3. Multifluidic Electrospinning**

The multifluidic electrospinning method is the process in which more than two polymeric materials can be used in production of nanofibrous structures. As more than two materials are utilized in construction of a single nanofiber structure, multifluidic electrospinning can be acknowledged as a more sophisticated version of coaxial electrospinning. In this method, needles having coaxial multichannel tubular structure are utilized in feeding multiple polymer solutions or melts to the process [16]. As a consequence, the number of solution parameters increase proportional to the number of solutions utilized. Although more sophisticated morphologies result in multi-responsive materials, there are several drawbacks of the multifluidic electrospinning method. Firstly, as more complex setup and technological process is used, this method has a higher chance of resulting in unstable morphology and low reproducibility [3]. Secondly, the content of the encapsulated material in the nanofibers is lower with respect to coaxially produced core/shell nanofibers.

### 2.3. Thermal Energy Storage (TES) Materials

Considering the projections suggest that the energy consumption will rise by 48% by the year 2040, the necessity in orienting the industry towards the renewable energy sources is undeniable [17]. Although developments in harnessing energy from natural and renewable sources such as wind, solar radiation and ocean waves have drawn tremendous interest in the recent years, a low cost and efficient storage of the energy has been the main obstacle in the widespread implementation. At this stage, thermal energy storage (TES) systems which stock energy by heating or cooling a medium have been the most convenient solution to energy storage problems. Some of the advantages of TES systems are reliability, efficiency and less pollution such as less CO<sub>2</sub> emission with respect to other methods. For example, in harnessing the solar radiation, solar panels constitute the majority of the market, but in the cases of low solar radiations such as nights, the efficiency of the system decreases drastically. This problem can be eliminated by implementing TES systems for both harnessing the low solar radiations and storing the energy [18].

TES systems can be categorized with respect to the means of energy storage such as sensible heat storage, latent heat storage and thermo-chemical heat storage.

#### 2.3.1. Sensible Heat Storage

The most widely used and the simplest form of thermal energy storage is sensible heat storage. In this method, the energy is stored by increasing the temperature of the medium in which the main parameter determining the efficiency is the specific heat of the medium. In determining the amount of energy stored by sensible heat storage Equation 2.1 can be utilized [19].

$$Q_s = \int_{t_i}^{t_f} m \cdot C_p \cdot dt = m \cdot C_p \cdot (t_f - t_i) \quad (2.1)$$

Where  $Q_s$  is the amount of energy stored, in Joules;  $m$  is the mass of the storage material, in kg;  $C_p$  is the specific heat of the material, in  $J/kg \cdot K$ ;  $t_f$  is the final and  $t_i$  is the initial temperature of the heat storing material, in K. It can be said that water is one of the most widely used heat storing material in terms of sensible heat storage at low temperatures (temperatures lower than  $100^\circ C$ ) due to its high specific heat and low cost. But in the cases where operating temperature exceeds  $100^\circ C$ , oils, molten salts or liquid metals may be used as sensible heat storage materials [18]. As the heat storage systems can be compared by determining the storage density ( $J/g$ ) values which indicate the amount of energy stored per unit volume or mass, the main disadvantage of the sensible heat storage is the low storage density value resulting from the low specific heat capacities of the heat storing materials. This problem results in necessity of large storage units which in turn increases both the installation and the operating costs [20]. Important properties such as specific heat capacity, density and working temperatures of some of the most widely used sensible heat storage materials are listed in Table 1.

Table 1. *Some of the widely used sensible heat storage materials* [21].

<b>Material</b>	<b>Working Temperature (<math>^\circ C</math>)</b>	<b>Density (<math>g/cm^3</math>)</b>	<b>Specific Heat (<math>J/g \cdot K</math>)</b>
Water	0-100	1.000	4.19
Calorie HT43 (Oil)	12-260	0.867	2.20
Engine Oil	$\leq 160$	0.888	1.88
Ethanol (Organic Liquid)	$\leq 78$	0.790	2.40
Sand-Rock Minerals	200-300	1.700	1.30
Cast Iron	200-400	7.200	0.56
NaCl	200-500	2.160	0.85
Silica Fire Bricks	200-700	1.820	1.0
Magnesia Fire Bricks	200-1200	3.000	1.15

### 2.3.2. Latent Heat Storage

Another type of TES system is latent heat storage system. In this method, the thermal energy is stored in the form of latent heat as the energy storing material changes its phase. The materials to be used in such systems, due to their characteristic melting and freezing properties are known as PCMs. Since all materials are able to experience phase change under certain circumstances, the term PCM has very distinctive qualifications. Firstly, a PCM should be able to undergo phase change in desired temperature ranges under reasonable pressures so that the operation can be considerable in terms of industrial specifications such as cost efficiency and feasibility. Secondly, in order to be considered in thermal energy storage applications, the PCM should possess relatively high latent heat with respect to other materials [22].

Latent heat storage systems have several advantages over sensible heat storage systems such as higher energy storage densities and isothermal heat absorption/emission process. Since PCMs possess high latent heats, the energy absorbed or released in melting/solidification process is much higher than the heat transferred during heating or cooling processes. This results in much more mass/volume efficient heat storage systems with respect to sensible heat storage systems such as water tanks or packed bed storage units. Moreover, as no temperature difference occur during heat absorbing or releasing process, even higher efficiency in means of energy usage is enabled.

The latent heat energy storage capacity is mainly determined by the dominating effect of latent heat of fusion rather than the specific heat value of the utilized PCMs [21]. The energy storage capacity of latent heat storage systems can be determined by using Equation 2.2.

$$Q_s = \int_{t_i}^{t_m} m \cdot C_p \cdot dt + m \cdot f \cdot \Delta q + \int_{t_m}^{t_f} m \cdot C_p \cdot dt \quad (2.2)$$

Where  $Q_s$  is the energy storage capacity of the system, in J;  $m$  is the mass of the PCM in the system, in g;  $C_p$  is the specific heat of the PCM, in J/g·K;  $f$  is the fraction of the PCM melted,  $\Delta q$  is the latent heat of the PCM, in J/g;  $t_i$ ,  $t_m$ ,  $t_f$  are initial, melting and final temperatures of the PCM, in K, respectively.

In terms of the phase change modes, PCMs can be classified as solid-solid, solid-gas or solid-liquid types. The solid-solid PCMs absorb energy during the change in crystallization forms while preserving the solid state. In liquid-gas type of PCMs, although the latent heat is higher than the other types, due to the significant amount of volume change during the vaporization of the material, it generates problems in storage of the phase changing material within the system. Solid-liquid type of latent heat storage systems on the other hand shows both high latent heat values and isochoric behavior with respect to other systems. Thus majority of the latent heat storage systems in the industry utilizes solid-liquid type PCMs [19, 21].

Solid-liquid type PCMs can be further categorized with respect to their chemical structure such as organic, inorganic and eutectic [22]. Organic PCMs exhibit enhanced reusability with only small degradation in latent heat over several thermal cycles and preserve their melting/freezing temperature perfectly. When the chemical structure is concerned, even organic PCMs can be further categorized as paraffin waxes comprised of straight n-alkene chains and non-paraffin compounds such as esters, fatty acids, alcohols and glycols [23]. Since paraffin waxes have methyl group in their structure they reveal higher amounts of latent heat energies from crystallization of (CH<sub>3</sub>)- chain. Inorganic PCM can be investigated under two main examples as salt hydrates and metallic ones. Salt hydrates are generally hydrates of inorganic salts and the heat storage or retrieval mechanism occurs as the dehydration or hydration reaction takes place at the melting temperature of the inorganic salt crystals [24]. They can be classified with respect to the dehydration mechanism as congruent, incongruent or semi-congruent. During the melting process, anhydrous salts, water molecules and salt hydrates with less moles of water in their structure are produced and dissolved by the released water molecules from hydrate crystals. When the released water during the

dehydration of the salt hydrates is not enough to dissolve all the solid phase, due to the density difference, phase separation occurs. This type of melting is termed as incongruent melting. On the other hand, when no phase separation occurs with all the salt being dissolved by the water molecules released from the salt hydrates, congruent melting is said to be present [23]. Although phase separation during dehydration poses a problem in terms of reusability and handling of the PCM, salt hydrates also have several advantages with respect to organic PCMs such as usability at higher temperatures, nonflammability and relatively higher thermal conductivity. Some examples to salt hydrates being utilized as PCMs can be given as magnesium sulfate ( $\text{MgSO}_4 \cdot 7\text{H}_2\text{O}$ ) and gypsum ( $\text{CaSO}_4 \cdot 2\text{H}_2\text{O}$ ) [19, 26].

Another type of inorganic latent heat storage material is metallic PCM which consists of low melting point metals and metal alloys such as gallium and bismuth-indium alloy. Although metal PCMs have advantages such as high thermal conductivity, high energy storage density per unit volume and nonflammability, low energy storage density per unit mass is a main problem in utilization of this type of PCMs [26].

Finally, eutectic materials are produced by combination of more than two of low melting point latent heat storage materials. By adjusting the composition of the eutectic, the melting temperature and the latent heat of the material can be changed according to the desired values. On the other hand, they possess lower latent heat with respect to other types of PCMs [24, 28].

### **2.3.3. Thermo-Chemical Heat Storage**

In thermo-chemical heat storage, heat is absorbed or released by utilizing reversible endothermic/exothermic reactions. The heat absorption occurs in the process of separating the feed chemical into products which can further be easily separated and purified. The reverse reaction can be initialized under suitable pressure and temperature conditions upon request by re-introducing the products of the previous endothermic reaction thus releasing certain amount of energy [27]. This type of thermal energy storage is suitable for conditions where one or more products of the

endothermic reaction are desirable chemicals or high temperature processes are being utilized. Decomposition of potassium oxide can be given as an example of thermochemical heat storage process where oxygen is produced during the endothermic reaction. The formula of the reversible decomposition of potassium oxide is given in Equation 2.3. The reaction occurs in the temperature range of 300-800°C with reaction enthalpy of 2.1 MJ/kg [18].



#### **2.4. Thermal Energy Storage Materials by PCM Encapsulation**

Utilization of phase change materials in terms of thermal energy storage vessels has been proven to be a promising method for solving the current global energy consumption problem. In investigating the types of PCMs with the aim of determining the most convenient one for industrial applications, organic PCMs become prominent due to their “no super cooling” effect and noncorrosive nature.

Although organic phase change materials are classified with respect to the phase change modes such as solid-solid, solid-liquid and solid-gas, they all have several advantages and disadvantages in terms of convenience in industrial applications. As solid-gas type of phase change materials possess higher specific latent heat values with respect to solid-solid and solid-liquid PCMs, the drastic volume change during the phase change process introduces many handling and process complications. On the other hand, solid-liquid type of PCMs have higher specific latent heat values with respect to solid-solid PCMs but again the conservation of the liquid state poses a challenge for the applicability of such materials [9]. In order to overcome this problem, several PCM encapsulation methods have been developed for production of thermally intelligent materials named as micro encapsulated phase change materials (MEPCM) and nano encapsulated phase change materials (NEPCM) [28].

Encapsulation methods of PCMs can be analyzed under two main titles as physical and chemical methods. Chemical encapsulation methods can be given as types of in-situ polymerization such as interfacial polycondensation, suspension polymerization and emulsion polymerization method. Physical methods on the other hand can be further analyzed under the titles of physico-chemical and physico-mechanical techniques. Some examples to physico-mechanical encapsulation are spray cooling, spray drying, multi-nozzle spraying, co-extrusion, fluid bed coating, centrifugal techniques and electrospinning. Additionally, examples of physico-chemical encapsulation methods can be given as coacervation, layer by layer assembly, sol-gel encapsulation and supercritical CO<sub>2</sub> assisted microencapsulation [29]. There have been many studies about development of thermal energy storage materials from various polymeric substances by using these encapsulation methods.

#### **2.4.1. Chemical Micro/Nano Encapsulation Methods**

##### **2.4.1.1. In-Situ Polymerization**

This type of encapsulation method involves polymerization at the interface between two liquid water soluble and oil soluble phases. The process generally has 4 steps such as: preparation of water/oil emulsion, preparation of the prepolymer mixture, addition of prepolymer mixture into water/oil emulsion and encapsulation of core materials and washing/drying of micro/nano encapsulated materials. In-situ polymerization can be further investigated under several titles such as interfacial polycondensation, suspension polymerization and emulsion polymerization.

Wei et al. [30] encapsulated n-octadecane by using melamine formaldehyde as the shell material by emulsifying and mixing at 8000 rpm. They obtained microcapsules with average diameter of 2.2  $\mu\text{m}$  having latent heat capacity of 144 J/g.

Hong and Park [31] produced a microencapsulated phase change material by using fragrant oil and melamine formaldehyde as the core/shell material, respectively and used 3000 rpm as the stirring rate. They have achieved MECPMs with average diameters less than 10  $\mu\text{m}$ .

Salaün et al. [32] used melamine formaldehyde as the shell material to encapsulate n-hexadecane and n-eicosane mixture with different concentrations. Phase change temperature of the resulting microencapsulated PCMs ranged between the -5°C and 30°C with latent heat of 163-170 J/g even after 13 heating-cooling cycles.

#### **2.4.1.1.1. Interfacial Polycondensation**

As the name suggests, in interfacial polycondensation, the microcapsule shell is formed at the interface between the oil and the water phase. Multifunctional monomer is initially introduced to the core material and then the resulting mixture is added to an aqueous solution containing emulsifiers and stabilizers. The polymerization reaction takes place at the interface of the oil and water (hydrophobic/hydrophilic). The reaction is controlled by addition of the other reactants at the final step in another aqueous solution [29].

#### **2.4.1.1.2. Suspension Polymerization**

In suspension polymerization method, the monomer to be polymerized into forming the shell structure is dispersed in the organic core material while the oil/water emulsion is prepared separately. As opposed to the interfacial polycondensation method, the polymerization does not take place at the interface but occurs in the core medium. Finally, the produced polymeric particles are precipitated at the interface forming the shell structure of the microcapsule [29].

#### **2.4.1.1.3. Emulsion Polymerization**

In this method, the monomer is directly mixed with the aqueous solution containing emulsifiers and surfactants. When the solution is subjected to high pressure or ultrasound homogenization, through the aliphatic nature of the surfactants binding to the monomer from the hydrophilic side, monomer droplets form in the aqueous medium with desirably monodisperse nature. The monomers in the form of monodisperse droplets are polymerized by continuous homogenization process at

specific temperature and atmospheric conditions making up the micro/nano capsules [29].

Chaiyasat et al. [33] prepared MEPCM by using suspension polymerization as the encapsulation method. They have used poly(divinyl benzene) as the shell material in order to encapsulate octadecane. Poly(vinyl alcohol) and dodecyl sulfate were used as the surfactant and co-surfactant. They have achieved microencapsulation with average particle size of 1.5  $\mu\text{m}$ . The latent heat of melting value of the MEPCMs was 192 J/g at a temperature of 22.6°C.

Alay et al. [34] developed MEPCM by using poly(methyl methacrylate) as the shell material and n-hexadecane as the phase change material constituting the core structure. They have used emulsion polymerization method and utilized allyl methacrylate and ethylene glycol dimethacrylate as the crosslinkers in producing uniform polymer particles. The microcapsules had average particle diameters between 0.22 to 1.05  $\mu\text{m}$  and the PCM encapsulation was between 29.04% and 61.42%. The resulting latent heat values of the mentioned encapsulation efficiencies were 68.89 J/g and 145.61 J/g, respectively. After development of MEPCMs, they have also investigated the thermal properties of these microparticles after impregnation onto woven fabrics. By using pad-cure method they have successfully impregnated the fabrics with microcapsules and achieved enthalpy values between 3.14 J/g and 10.02 J/g for the woven fabric materials.

## **2.4.2. Physical Micro/Nano Encapsulation Methods**

### **2.4.2.1. Physico-Chemical Methods**

#### **2.4.2.1.1. Coacervation Method**

Coacervation method is developed on the basis that in polymer solutions as the solubility of the polymer is decreased by addition of another solvent or cooling the solution, insoluble polymer particles start to precipitate. In this method, the organic core material is dispersed in the water solution. Then hydrophilic polymer is added to

the solution and a complex formation occurs between the polymer and the organic core material. Finally, coacervation of the polymer is induced by adjusting various parameters such as solution pH, solution temperature or further dilution [35]. The process is visualized in Figure 5.

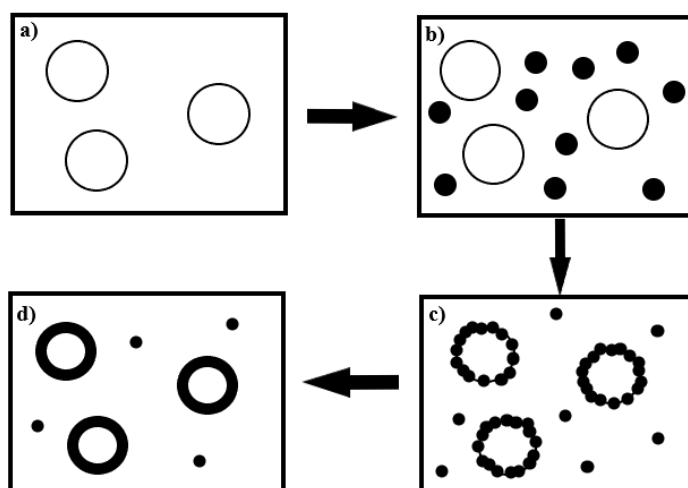


*Figure 5.* Representation of the steps of the coacervation method. a) Dispersion of core material in water solution, b) addition of hydrophilic polymer, c) complex formation between the core material and the shell material, d) coacervation of the polymer.

#### **2.4.2.1.2. Layer by Layer Electrostatic Assembly**

Layer by layer assembly is conducted by immersing the material to be covered into positively and negatively charged polyelectrolyte solutions in a cyclic manner. The number of layers and the multilayer shell thickness can be controlled by adjusting the overall number of immersion cycles [36].

#### **2.4.2.2. Physico-Mechanical Methods**

##### **2.4.2.2.1. Coextrusion**

In coextrusion method, two or more types of polymeric fluids are pumped from concentric (coaxial) tubes and fed through a die into the collecting medium. By

applying certain vibration to the die, core/shell structure polymeric droplets are formed and hardened by crosslinking, cooling or solvent removal [29]. The process is shown in Figure 6.

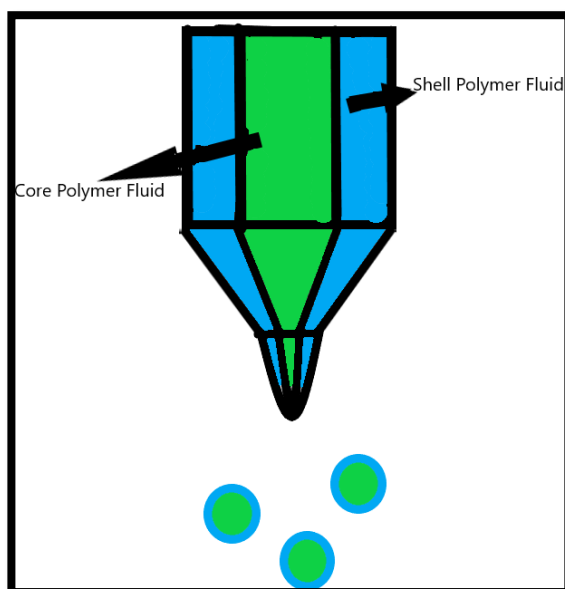


Figure 6. Schematic representation of coextrusion method.

#### 2.4.2.2.2. Spray Drying

Spray drying is a low cost microencapsulation method that has been extensively used in industry for coating oils or flavors. In this method, the material to be coated is dissolved in the polymer solution. The resulting solution is fed to a hot chamber where the solvent evaporates and the polymer holds onto the core material. In such systems, water soluble polymers are generally preferred due to the hazardous properties of volatile chemicals. In spray drying method, the most important parameter is the polymer to core material ratio in the solution system because excess amount of polymer may cause agglomeration of the microcapsules or insufficient polymer may result in uncoated core materials [29]. Several microencapsulation methods and their respective average particle sizes can be seen in Table 2.

Table 2. *Microencapsulation methods with corresponding average particle size ranges* [29].

<b>Encapsulation Method</b>	<b>Particle Size (<math>\mu</math>)</b>
In-situ polymerization	0.5 – 1100
Interfacial polycondensation	0.5 – 1000
Emulsion polymerization	0.1 – 0.5
Coacervation	2 - 1200
Layer by layer electrostatic assembly	0.02 - 20
Co-extrusion	250 - 2500
Spray drying	5 - 5000

#### **2.4.2.2.3. Electrospinning**

In thermal energy storage materials, some of the most important properties are high encapsulation efficiency of the phase change material and durability of the core/shell structure under different external effects. Thus, fiber morphology which introduces enhanced tensile properties in the direction of fiber alignment and high PCM encapsulation efficiency have been found to be highly desirable for such applications [37]. Although there have been several methods such as coating and wet/melt spinning for production of microfibers, electrospinning has proved itself to be the most versatile and cost effective method for nanofiber production [3]. Additionally, nanofiber morphology also exhibits advantageous properties in terms of heat exchange with the surrounding such as high specific surface area and length to diameter ratio [12].

Electrospinning method can be classified into three categories such as uniaxial electrospinning, coaxial electrospinning and multifluidic electrospinning with respect to the structure of the produced fibers. As described in Section 2.2, in uniaxial electrospinning a single spinneret is used. Thus, encapsulation is achieved by mixing two immiscible or semi-miscible PCMs and polymeric materials in either melt or dissolved state in uniaxial electrospinning method [38]. In such cases, the shell material is generally in excess amount with respect to the PCMs in order to maximize the encapsulation efficiency. On the other hand, in coaxial electrospinning, polymer/PCM couple is fed to the needle tip from two concentric tubes. PCM being fed to the inner tube, the resulting fibers exhibit complete encapsulation when

compared to fibers produced by uniaxial electrospinning. Lastly, in multifluidic electrospinning one or more than one type of PCM may be encapsulated in a single fiber structure by using multi-channel needle configuration.

Fiber morphology exhibits several properties making it suitable for energy storage purposes such as high specific surface area and high length to diameter ratio [39]. Having high specific surface area, in fibrous materials, transmission of heat to/from the structure is much faster than in bulk materials. Thus, heat can be absorbed in the form of latent heat and released back to the exterior more rapidly, giving the material less reaction time to the environmental temperature changes. Also, fiber structure has been widely used in reinforcement materials due to its enhanced tensile properties, especially against the forces in the direction of the fiber alignment. As the fiber length to diameter ratio decreases, tensile properties are further enhanced since fiber density increases resulting in better stress distribution [40]. There have been many studies utilizing the electrospinning method for development of thermal energy storage materials.

Arecchi et al. [38], developed emulsion electrospinning for encapsulation of hexadecane by using poly(vinyl alcohol) (PVA) as the shell material. An emulsion was prepared by mixing hexadecane oil with water and addition of PVA. The amount of hexadecane in the polymer-emulsion blend was 0.5 to 1.5 wt. %, whereas PVA concentration was 8 wt. %. It was found that bead like formations were present in the resulting nanofibers with average diameter of about 181 nm where no coalescence of droplets was observed.

Chen et al. [41] investigated the effects of PEG with different number average molecular weights on the morphology and thermal properties of nanofibers. They have used cellulose acetate (CA) as the shell material and uniaxial electrospinning as the fiber production method. By using PEG with molecular weight of 2000, 4000, 6000, 10000 and 20000 they have produced core/shell structured fibers with average fiber diameter ranging from 1029 to 1752 nm with increasing molecular weight whereas

neat CA fibers had average diameter of 720 nm. They have also observed that with increasing PEG molecular weight, the thermal energy storage capacity of the nanofibrous mats also increased from 47.93 J/g to 73.48 J/g. This was due to the fact that the degree of crystallization of the fibers was increased with the presence of higher molecular weight PEG.

Wang et al. [42] developed a multicomponent thermal energy storage material by using multifluidic electrospinning. In the study, poly(vinyl pyrrolidone) was utilized as the shell material and two hydrocarbons, hexadecane and eicosane as the PCMs were used. In the experimental setup, the needle was comprised of a big outer tube and two inner tubes located side by side coaxially in the big tube. This way, a thermal energy storage material with two distinct melting/freezing characteristics was developed with a single continuous process. The average diameter of the resulting fibers was 2.6  $\mu\text{m}$  and the melting/freezing temperatures of the hexadecane/eicosane were 17°C/9°C and 36°C/30°C, respectively. The latent heat values of hexadecane and eicosane were found to be 11.5 J/g and 11.8 J/g, respectively.

## **2.5. Coaxial Electrospinning Parameters**

Electrospinning method has three main types of factors affecting the nanofibrous product properties. These factors are process parameters, solution parameters and ambient parameters. Process parameters can be mentioned as applied electrical potential and tip to collector distance. Solution parameters on the other hand are solution concentration and solution feed rate. Lastly, ambient parameters are temperature and the relative humidity of the electrospinning environment. Since more than one polymer solutions are utilized in coaxial electrospinning, the number of solution parameter that requires optimization increases proportionally to the number of solutions. Additionally, not only the individual solution properties, but also the proportion of the solution parameters are important for a stable coaxial electrospinning process. There have been many studies investigating the effects of coaxial electrospinning parameters on the final fiber morphology.

In coaxial electrospinning, two concentric polymer solution are fed to the needle in order to form core/shell structured nanofibers. As different from the uniaxial electrospinning, the electrostatic forces derived from applied electrical potential difference accumulates on the outer surface of the shell polymer solution [13]. Thus, the inner polymer solution does not face electrostatic forces but stretches towards the collector under the effect of viscous drag at the interface of the two polymer solutions. As a consequence, unlike uniaxial electrospinning, the inner polymer solution in coaxial electrospinning does not necessarily has to be electrospinnable [43]. Although critical molecular entanglement is necessary for fiber production by electrospinning, the core solution need not to have such limitation due to the above mentioned condition. In addition, the ratio of the core/shell solution viscosities is also important in coaxial electrospinning. Since the most significant parameter affecting the solution viscosity is the concentration, it presents high importance for production of core/shell structure.

Tiwari et al. [44] investigated the effect of viscosity ratios of core/shell solutions on the fiber structure. PLA-PGA copolymer was used as the building material. It was found that as the viscosity ratio of the core/shell solutions exceeded 1.7, the electrospinning was unsuccessful because of the rapid evaporation of the scarce shell solvent. On the other hand, when the viscosity ratio was below 0.55, no continuous core structure was formed due to the insufficient entanglements.

A study by Kaerkitcha et al. [45] revealed that the viscosity ratio of the core/shell solutions not only affects the spinnability but also has a significant impact on the fiber morphology. It was found that as the core solution viscosity increased, the wall thickness of the core/shell nanofibers increased since less amount of core polymer could be dragged by viscous drag during the electrospinning process. The total diameter of the fibers also increased with increasing solution viscosities.

As in the electrospinning method, nanofiber morphology can be generated when the electrostatic forces which are consequences of applied electrical potential difference,

can overcome the polymer solution surface tension. Thus, there exists a minimum amount of applied electrical potential that is necessary for nanofiber production [43]. On the other hand, as the electrostatic force applied on the spinning solution exceeds certain limits, the increased stretching of the polymer solution results in thinner nanofibers. When the stretching is increased even more, it may overcome the molecular entanglements and result in electrospraying of droplet morphologies rather than fibers [46].

When the feed rate of the core/shell solutions are concerned in coaxial electrospinning, it is known that the shell solution feed rate needs to be higher in order to better cover the core solution and induce higher viscous drag force due to increasing contact area [43].

In a study conducted by Gonçalves et al. [47] poly(vinyl acetate) (PVA) and PLA ultrafine fibers were produced by using coaxial electrospinning method. They have observed the effect of core solution feed rate. They have determined that defect free nanofibers were able to be produced only when the shell solution feed rate was four times greater than the core solution feed rate. When the flow rates of core/shell solutions were equal, no uniform fiber was produced. This was due to the lack of encapsulation of the core material. Finally, it was determined that the shell solution flow rate should be at least two times greater than that of the core solution for production of core/shell nanofibers.

## **2.6. Composite Nanofibers**

One of the common methods of enhancing multi-functional properties of various materials is introduction of additives into their matrices. Although nanofiber morphology introduces enhanced properties in various aspects, development of composite structures has been broadly practiced in academia and industry [48]. The ability of alignment of additives in the fiber matrix has been accepted to be another advantage of the composite fibers [46, 50].

Özdemir et al. [50] investigated the effect of an organically modified montmorillonite, Cloisite 30B on the poly(lactic acid) PLA/PEG nanofibers. The polymers were melt mixed by using a twin-screw extruder. While phase separation throughout the electrospinning process was observed in melt mixed PLA/PEG nanofibers, with introduction of nano-clay additive this problem was eliminated. This was due to the fact that both PLA and PEG had diffused into the silicate layers of the nanoclay material enhancing the interactions between polymeric substances. Additionally, presence of quaternary ammonium salts with organically modified clay addition, contributed to the electrical conductivity of the melt electrospun mixture and thus the resulting fiber diameter distribution became narrower.

Babapoor et al. [11] investigated the effect of various inorganic additives ( $\text{SiO}_2$ ,  $\text{Al}_2\text{O}_3$ ,  $\text{Fe}_2\text{O}_3$ , and  $\text{ZnO}$ ) and their concentration on the coaxially electrospun PEG/PA6 core/shell nanofibers. They observed that with the introduction of inorganic additives into the fiber structure the average fiber diameter decreased. This was due to the increase in the conductivity of the electrospinning solution resulting in induction of higher electrostatic forces (higher surface charge density). When the latent heat values of the nanofibers were investigated, it was seen that the thermal energy storage property decreased for the composite structure. This was attributed to the retardation of the crystallization of PCM during electrospinning in the presence of particles.

Golestaneh et al. [51] developed thermal energy storage material by incorporating eutectics of capric acid, lauric acid and palmitic acid as the PCMs. They utilized poly(ethylene terephthalate) (PET) as the shell material and  $\text{SiO}_2$ ,  $\text{Al}_2\text{O}_3$ ,  $\text{Fe}_2\text{O}_3$ ,  $\text{ZnO}$  as the inorganic additives. It was observed that with increasing additive content, the onset of the melting temperature as well as latent heat value of the PCMs were decreasing. This was attributed to the retardation of the PCMs crystallization in the presence of additives. On the other hand, thermal stabilities of the core/shell fiber composites increased with inorganic additive introduction. This was due to the local heat barrier effect of the nanoparticles in the PCM matrix.

## **2.7. The Scope of the Thesis**

Electrospinning has proven itself to be one of the most versatile and cost efficient production method of ultrafine polymeric nanofibrous materials over the last decade. Additionally, nanofiber structure is known to possess several advantages in terms of tensile properties and high specific surface area [52]. Such properties of ultrafine fibers make them highly suitable for utilization in development of many multifunctional engineering polymeric materials such as thermal energy storage fabrics.

PA6 is known both in the industry and the academia as an engineering polymer having superior mechanical properties such as tensile strength and toughness. These features qualify PA6 as an excellent material for utilization in development of reinforcing structures. Thus, in this study, PA6 was chosen to be utilized in the shell structure of the nanofibers as the encapsulating material. PEG on the other hand is widely known for its high latent heat values at temperature ranges depending on the molecular weight [53]. Thus usage of PEG as the PCM in the core/shell nanofiber structure demonstrated advanced thermal energy storage properties. Halloysite nanotubes (HNTs) is a low cost, natural and inorganic material depicting nanotube structure. Due to its structure, it has very high thermal stability with respect to the organic polymeric substances [54]. Thus, usage of HNTs as the nano additive has revealed enhanced thermal stability properties in the final composite nanofibrous material [55].

As a result of the literature survey, it has been seen that there is an absence of study concentrating on incorporation of HNTs into the PEG/PA6 core/shell nanofibrous materials by using coaxial electrospinning method and optimization of the electrospinning parameters. It has been thought that HNTs have high potential in improving the thermal stability and affecting the thermal characteristics of core/shell nanofibers due to their inorganic nanotube structure.

In this thesis, PEG as an organic solid-liquid PCM, was encapsulated by PA6 in the fiber morphology by using coaxial electrospinning method. Additionally, a comprehensive study on optimization of the electrospinning parameters such as

solution concentration, applied electrical potential and solution feed rate was done in order to acquire uniform core/shell structured nanofibers. Thermal energy storage properties, thermal stability and morphologies of the electrospun samples were determined by DSC, TGA and SEM analyses. Finally, with the aim of further enhancing these properties of the core/shell structured nanofibers, composite structure was developed by introduction of HNTs into the nanofibers. The HNTs were introduced into the PEG solution with the aim of encapsulating in the core structure of fibers. Activation of the surface of HNTs were also done by piranha etching in order to enhance the interaction between the additive and the polymer. It was known that the surface defects at the outer surface of the HNTs contain hydroxyl groups. Thus, by acid etching, the affinity between PEG and HNTs was aimed to be increased with hydroxylation of the nanotube surfaces.



## CHAPTER 3

### EXPERIMENTAL

#### 3.1. Materials

##### 3.1.1. Polyamide-6 (PA6)

Polyamide-6, PA6 (Tecomid NB40,  $M_v$ : 26000 g/mol) was obtained from Eurotec Engineering Plastics. The specifications for the material are given in Table 3.

Table 3. *The Properties of PA6* [56].

Properties	Value
Density ( $\text{g/cm}^3$ )	1.13
Melting Temperature ( $^{\circ}\text{C}$ )	223
Processing Temperature ( $^{\circ}\text{C}$ )	240-260
Color	Natural
Moisture Absorption (%) (50% RH, 23 $^{\circ}\text{C}$ )	3

##### 3.1.2. Poly(ethylene glycol) (PEG)

Molecular biology grade poly(ethylene glycol) (PEG) ( $M_n$ : 6000 g/mol) was purchased from Merck. The specifications for the material are given in Table 4.

Table 4. *The Properties of PEG 6000* [57].

Properties	Value
Density ( $\text{g/cm}^3$ )	1.2
Melting Temperature ( $^{\circ}\text{C}$ )	60-65
Color	White

### 3.1.3. Halloysite Nanotubes (HNTs)

Halloysite Nanotubes (HNTs) having chemical formula of  $\text{Al}_2\text{Si}_2\text{O}_5(\text{OH})_4 \cdot 2\text{H}_2\text{O}$  were acquired from Sigma-Aldrich (685445). Properties of HNTs are given in Table 5.

Table 5. *The Properties of HNTs* [58].

Property	Value
Average Diameter (nm)	30-70
Length ( $\mu\text{m}$ )	1-3
Surface Area ( $\text{m}^2/\text{g}$ )	64
Color	White

### 3.1.4. Solvents

Formic acid (Merck, 98-100% purity) and acetic acid (Sigma-Aldrich, 99.8-100.5% purity) were used as solvents in the electrospinning process. For the surface activation of HNTs, sulfuric acid (Sigma-Aldrich, 95-97% purity) and hydrogen peroxide solution (Sigma-Aldrich, 34.5-36.5% purity) were used through preparation of the piranha solution.

## 3.2. Experimental Method

### 3.2.1. Preparation of Polymer Solutions

#### 3.2.1.1. Preparation of Shell Solution

In the preparation of the shell solution, formic acid and acetic acid with 4:1 by volume (v/v) ratio was used as the solvent system. In all experiments, 12.5 ml of solvent was used to dissolve PA6 pellets. Amounts of PA6 pellets that were necessary for preparation of the predetermined polymer concentrations (10, 12 and 15 wt. %) were weighed with high precision balance (Precisa-XB220A) and dissolved in the solvent system at room temperature. The resulting mixture was stirred for 5 hours at room temperature by using a magnetic stirrer (Velp Scientifica, Arex heating magnetic). The schematic representation of the procedure is given in Figure 7.

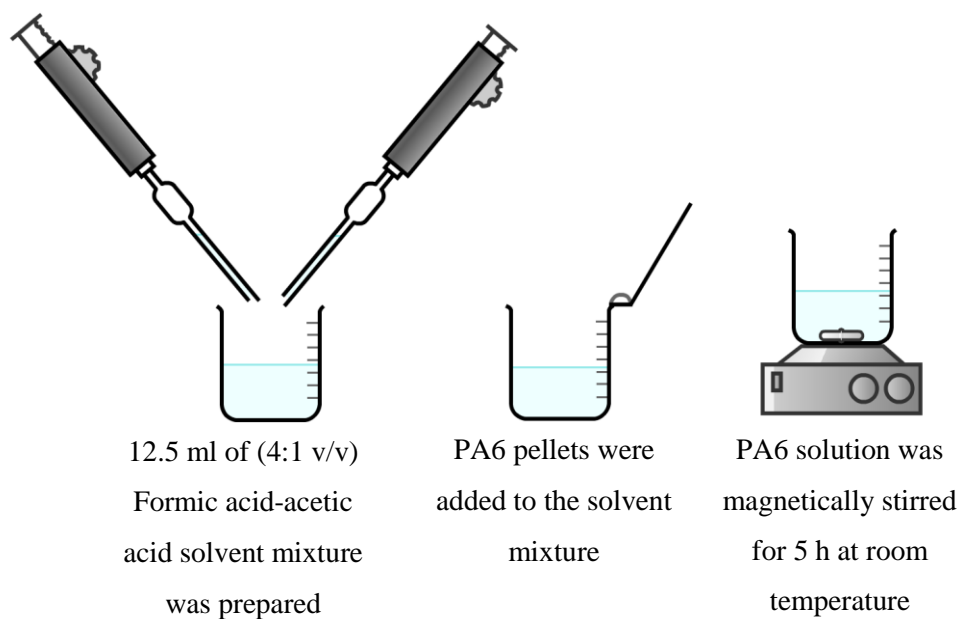


Figure 7. Experimental procedure for the preparation of the PA6 solution.

### 3.2.1.2. Preparation of Core Solution

In the preparation of the core solution, formic acid and acetic acid with 4:1 by volume (v/v) ratio was used as the solvent system. In all experiments, 10 ml of solvent was used to dissolve the PEG flakes. Amount of PEG that was necessary for preparation of the predetermined polymer concentrations (30, 40 and 50 wt. %) were weighed with high precision balance (Precisa-XB220A) and dissolved in the solvent system at room temperature. The resulting mixture was stirred for 2 hours using the magnetic stirrer until homogeneous solution was observed. The schematic representation of the procedure is given in Figure 8.

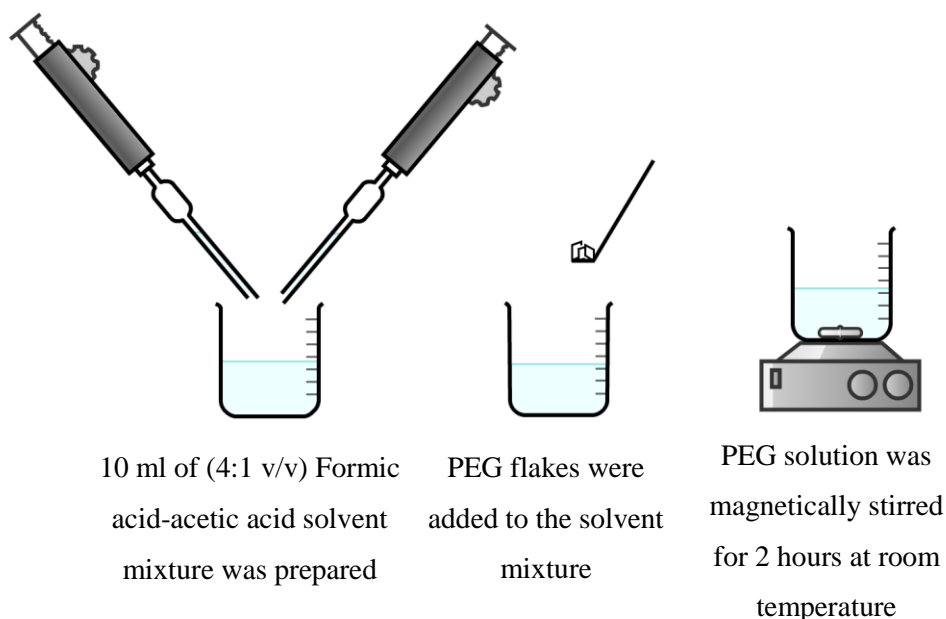


Figure 8. Experimental procedure for the preparation of PEG solution.

### 3.2.2. Activation of HNTs by Piranha Etching

In order to activate the HNTs surfaces with more –OH bond formation on the surface defects, piranha etching was conducted. Piranha solution was prepared by mixing sulfuric acid and hydrogen peroxide solution in 7:4 (v:v) ratio. The piranha solution was then heated up to 90°C by using a water bath on a hot plate. HNTs were previously vacuum dried for five hours at 110°C. Dried HNTs were introduced into the piranha solution and subjected to etching for one hour. The solution was then vacuum filtered by using acid resistant sintered glass gooch. The HNTs remaining after the filtering operation was rinsed by excess amount of ultra-pure water. Finally, the HNTs were dried in a vacuum oven at 110°C for five hours.

### 3.2.3. Calculation of the PEG/PA6 Weight Ratio in the Nanofiber Mats

In calculation of the PEG and PA6 content of the nanofibrous mats, electrospinning process parameters such as electrical potential difference, feed rate of the core and shell solutions, needle tip to collector distance were kept constant as 24 kV, 0.1 ml/h, 0.35 ml/h and 10 cm, respectively. Since during the electrospinning process the

solutions are introduced to the system by adjusting the volumetric feed rate values, the final densities of the PEG and PA6 solution were calculated. In calculation of the individual amounts of PEG and PA6 in the electrospun mat, the electrospinning time, solution density, solution concentration and volumetric flow rate of the solution were taken into account. The respective calculation of solution densities and polymer ratios in the nanofibrous sample are shown in Equations 3.1-3.3.

$$\text{Solution Density} = \frac{\text{Total Solution Mass}}{\text{Total Solution Volume}} \quad (3.1)$$

$$\text{PEG, PA6 Amount After "t" Amount of Time} = t \times \rho \times v \times C \quad (3.2)$$

$$(\text{PEG: PA6}) = \frac{m_{\text{PEG}}}{m_{\text{PEG}} + m_{\text{PA6}}} \times 100 \quad (3.3)$$

In Equation 3.2, t is the amount of time electrospinning was conducted for, in hours;  $\rho$  is the solution density, in g/ml; v is the volumetric feed rate of the solution, in ml/h, and C is the solution concentration, in weight percent. In Equation 3.3,  $m_{\text{PEG}}$  is the PEG mass and  $m_{\text{PA6}}$  is the PA6 mass in the electrospun mat. By using Equations 3.1, 3.2 and 3.3 the PEG/PA6 mass ratios were calculated for all the concentration pairs of core and shell solutions. The calculated mass ratios of polymers are presented in Table 6.

Table 6. (PEG:PA6) mass ratio data of nanofibrous samples produced by using different solution concentrations.

PEG Solution Concentration (wt. %)	PA6 Solution Concentration (wt. %)	(PEG:PA6)
30	10	(51:49)
	12	(46:54)
	15	(40:60)
40	10	(58:42)
	12	(53:47)
	15	(47:53)
50	10	(64:36)
	12	(59:61)
	15	(53:47)

### 3.2.3.1. Preparation of PEG/HNTs Composite Solution

In preparation of the composite solution, formic acid and acetic acid with 4:1 (v/v) ratio was used as the solvent system. The total volume of the two solvents was always prepared as 10 ml. Knowing the amount of the solvent used, the desired amounts of the HNT and PEG were determined by solving Equations 3.4 and 3.5 simultaneously using the MATHCAD software. The equations are given below.

$$\text{PEG Concentration (wt. \%)} = \frac{m_{\text{PEG}}}{m_{\text{PEG}} + m_{\text{HNTs}} + m_{\text{solvent}}} \quad (3.4)$$

$$\text{HNTs Concentration (wt. \%)} = \frac{m_{\text{HNTs}}}{m_{\text{PEG}} + m_{\text{HNTs}}} \quad (3.5)$$

Desired amount of HNTs (0.5, 1, 3 and 5 wt. % concentrations) were weighed with respect to the predetermined PEG amount in the solution and the resulting solution was ultrasonicated in an ultrasonic bath (Bandelin Sonorex RK 100) at room temperature for at least 30 min or until homogeneous dispersion of the HNTs particles were observed. Afterwards, the predetermined amount of PEG to acquire designated

weight percentages in the form of flakes was added and magnetically stirred for 2 hours until homogeneous solution was observed. The schematic representation of the procedure is given in Figure 9.

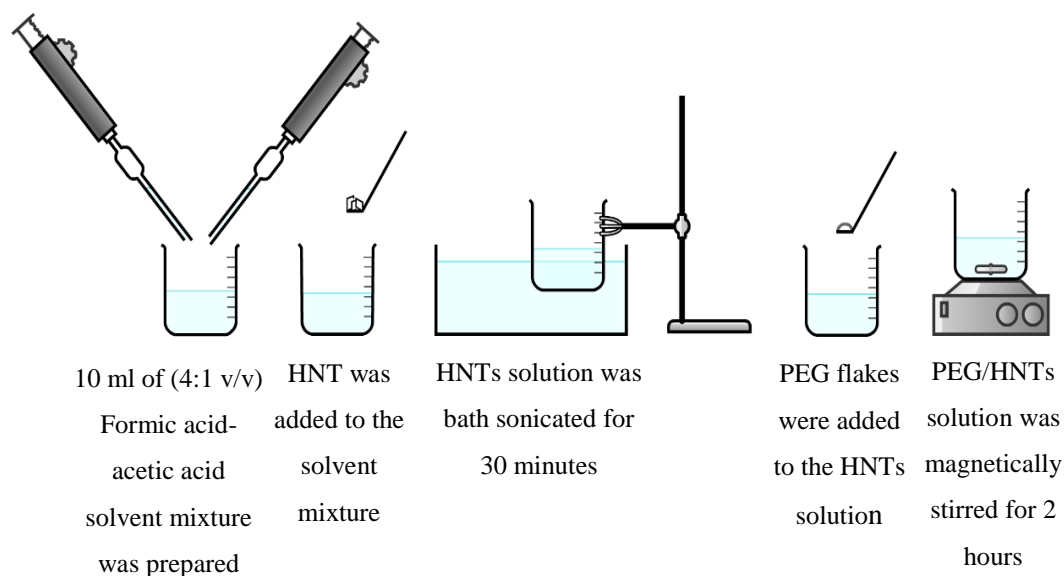


Figure 9. Experimental procedure for the preparation of PEG/HNTs solution.

### 3.2.4. Coaxial Electrospinning Process

Coaxial electrospinning experiments were conducted using a bottom-up type Invenso NE300 electrospinning device. In order to acquire core/shell structured nanofibers, coaxial needle was used with 0.8 mm of core needle and 1.6 mm of shell needle diameter. Technical specifications of the device are seen in Table 7. Coaxial electrospinning parameters that were used in both the neat and composite nanofiber production can be seen in Table 8. All the electrospinning experiments were conducted at room temperature ( $22 \pm 3^\circ\text{C}$ ) and under  $35 \pm 5\%$  relative humidity. The temperature and relative humidity values were determined by using a digital hygro-thermometer in the electrospinning chamber.

Table 7. Technical specifications of Inovenso NE300 electrospinning device.

Property	Value
Electrical Potential Difference Range (kV)	0-40
Feed Rate Range (ml/h)	0.01-1000
Inner Needle Diameter (mm)	0.8
Outer Needle Diameter (mm)	1.6
Collector Types	Rotating Cylinder
	Flat Plate
Cylindrical Collector Dimensions (diameter×length)	100 mm × 200 mm
Collection Surface	Aluminum Foil

The parameters optimized in this study include core/shell solution concentration, applied electrical potential difference, core/shell solution feed rates and HNTs concentration.

Table 8. Parameters of the coaxial electrospinning process.

Optimized Parameters	Variables	Fixed Parameters
Solution Concentration (Core/Shell) (wt. %)	<b>PEG Concentration</b> 30, 40, 50	24 kV, 0.1/0.3 ml/h, 10 cm, no HNTs, 30 mins, plate collector
	<b>PA6 Concentration</b> 10, 12, 15	
Applied Electrical Potential Difference (kV)	20, 24, 28	30/12 wt. %, 0.1/0.3 ml/h, 10 cm, no HNTs, 30 mins, plate collector
Solution Feed Rate (Core/Shell) (ml/h)	<b>PEG Solution Feed Rate</b> 0.1, 0.15, 0.2	24 kV, 30/12 wt. %, 10 cm, no HNTs, 30 mins, plate collector
	<b>PA6 Solution Feed Rate</b> 0.3, 0.35, 0.4, 0.5	
HNTs Concentration (wt. %)	0.5, 1.0, 3.0, 5.0	24 kV, 30/12 wt. %, 0.1/0.35 ml/h, 10 cm, 1 h, rotating cylinder collector (100 rpm)

### **3.3. Characterization Methods**

#### **3.3.1. Scanning Electron Microscopy (SEM) Analysis**

The morphologies of the produced nanofibers were analyzed using a QUANTA 400 F Field Emission high resolution Scanning Electron Microscope. Nanofibers were collected onto aluminum foils and 1x1 cm<sup>2</sup> pieces were cut from every sample to adhere on the stubs using carbon band. Afterwards, the samples were coated with gold-palladium alloy to introduce conductivity on the polymeric nanofiber surface. Average fiber diameter measurements were conducted using ImageJ (Fiji) (NIH, USA) software. In order to determine the average fiber diameter of a nanofibrous sample, three images were analyzed by taking 100 fiber diameter measurements from each, making 300 measurements in total.

#### **3.3.2. Transmission Electron Microscopy (TEM) Analysis**

Morphologies of the core/shell structure of the nanofibers were analyzed using FEI brand (Tecnai G<sup>2</sup> Spirit Biotwin) high contrast transmission electron microscope (C-TEM) which was at an acceleration voltage of 120 kV. In the preparation step of the samples, 400 mesh copper grid was placed on the flat plate collector and electrospinning was conducted for 2-3 seconds.

#### **3.3.3. Fourier Transformed Infrared (FTIR) Spectroscopy**

A Perkin Elmer FTIR-ATR instrument was utilized in order to determine the chemical structures of PEG, PA6 polymers and HNTs in core/shell morphology to investigate the potential changes in the structures. Samples were analyzed in the wavenumber range of 600-4000 cm<sup>-1</sup> with 32 scans. HNTs and HNT-P were pressed into KBr pellets and analyzed using a Shimadzu IRPrestige 21 instrument.

#### **3.3.4. Thermogravimetric Analysis (TGA)**

A Shimadzu DTG-60 instrument was used in order to observe the thermal stability of the samples by detection of the degradation temperatures. Both neat and composite

nanofibrous materials were heated from 25°C to 800°C with a rate of 10°C/min under 50 ml/min N<sub>2</sub> flow rate.

### 3.3.5. Differential Scanning Calorimetry (DSC) Analysis

Differential scanning calorimetry analysis of the samples was conducted by heating from 25°C to 150°C with heating rate of 10°C/min using Shimadzu DSC-60A. Approximately 10 mg of sample was placed into the aluminum pan and heating program was implemented on each sample to analyze the melting temperature, latent heat of melting and PEG encapsulation efficiency characteristics. PEG encapsulation efficiency is calculated by using Equation 3.6.

$$\text{PEG encapsulation efficiency} = \frac{\Delta H_{\text{exp}}}{210 \times \text{PEG Mass Ratio}} \quad (3.6)$$

### 3.3.6. X-Ray Powder Diffraction Analysis (XRD)

XRD analysis was performed on the dried and piranha etched HNTs in order to determine any effect of surface activation on the crystal structure of the HNTs. Rigaku Miniflex X-ray Diffractometer instrument with CuK<sub>α</sub> (30 kV, 15 mA, λ= 1.54051 Å) source was used. 2θ range was selected between 3°- 60°. Scanning speed was set to 2° min<sup>-1</sup>.

### 3.3.7. Tensile Test

The mechanical properties of the nanofibrous samples were determined using a Shimadzu Autograph AG-IS 100kN universal tensile test machine. A photograph of the device can be seen in Figure 10.



*Figure 10.* Shimadzu Autograph AG-IS 100kN universal testing machine.

Tensile testing on the nanofibrous samples was conducted based on the specification from ASTM D882-02 standard. Nanofibrous mats to be subjected to tensile testing had length of 50 mm, width of 10 mm and gauge length of 30 mm. The thickness of all the samples were in the range of 60-130  $\mu\text{m}$  and were determined by using a micrometer (Micromar Micrometer 4 EWR) with a precision of 0.0001 mm. The cross-sectional area of the mats was calculated by using the average thickness and width values. Considering the dimension of the nanofibrous samples, a load cell with maximum load capacity of 1 kN and crosshead speed of 15 mm/min was used. For every sample subjected to tensile testing, 5 measurements were taken in order to acquire both the average values and standard deviations. The sample frames were prepared by drawing the sample sizes on A4 papers. After cutting sample sized papers, double sided tape was used to stick them on the electrospun samples having aluminum foils on the other side. The samples were cut from the aluminum foil with paper frame on the one side and aluminum foil on the other. The electrospun samples were peeled off from the

aluminum foil carefully without harming the samples. In order to end up with 10x10 mm<sup>2</sup> frames on both ends of the samples, the papers remaining between the two frames were cut with scissor. Since the nonwoven fibrous mats were subjected to the tensile testing, the resulting tensile strength, modulus and elongation at break values represent the properties of the porous mat structure with nanofibrous morphology rather than the individual nanofiber's.

### 3.3.8. Thermal Cyclic Test

In determination of the thermal energy storage property of the core/shell structured nanofibrous samples, heating above the melting temperature of PEG and cooling below the freezing temperature of PEG was done. The freezing temperature of PEG 6000 was known to be at about 42°C when cooled with rate of 10°C/min [59]. The neat core/shell, 3 wt. % HNTs and 3 wt. % HNT-P added nanofibrous samples were weighed between 5-10 mg and put into aluminum pans. DSC analysis was conducted on the samples by heating up to 150°C with 10°C/min heating rate and cooling down to 28°C. The melting enthalpy and melting temperature values were recorded for every heating. After ten successive heating over the melting temperature and cooling below the freezing temperature of PEG, the final melting enthalpy values were used in calculation of the percent melting enthalpy maintained by comparing with the enthalpy value obtained from initial heating cycle. Calculation of the melting enthalpy maintained was done by using Equation 3.7

$$\text{Enthalpy Maintained (\%)} = \frac{\Delta H_{10^{\text{th}} \text{ Heating}}}{\Delta H_{1^{\text{st}} \text{ Heating}}} \times 100 \quad (3.7)$$

Although no cooling program was used during the thermal cyclic test, temperature versus time data was recorded for every 10°C. The cooling rates of the samples were determined by taking the average of the first and last cooling data of every sample. The exponential curve was split into twelve linear lines by taking a data point every 10°C while cooling, their slopes were calculated and the average of these slopes was taken in order to specify the cooling rate of the samples. The average cooling rate was

calculated to be 18°C/min. A representative temperature versus time graph can be seen in Figure A.1 in Appendix A. The temperature and time data are also given in Table A.1 in Appendix A.



## CHAPTER 4

### RESULTS AND DISCUSSION

#### 4.1. Optimization of the Electrospinning Process Parameters

In this study, in order to produce bead free, fine and uniform fiber structures, parameters such as solution concentration, applied electrical potential and solution feed rates were optimized. In the preliminary experiments, many attempts were made in order to find the suitable parametric ranges by which considerable fibrous morphologies were acquired using coaxial electrospinning method.

##### 4.1.1. Preliminary Studies

Before the actual parameter optimization studies, it was necessary to determine the parameter ranges where nanofiber production from PEG and PA6 was possible. For this reason, firstly, electrospinning of PEG was experimented by changing the polymer concentration while keeping the applied electrical potential, solution feed rate and tip to collector distance constant. In the beginning of the preliminary studies, it was necessary to determine the electrospinning properties of neat PEG. Thus, PEG solutions with different concentrations were prepared by using dichloroethane (DCE) as the solvent. DCE was chosen as the solvent according to the literature studies in which the same core/shell materials (PEG/PA6) were utilized [10, 11]. Electrospinning experiments were conducted with the parameters of 0.33ml/h solution feed rate, 24 kV applied electrical potential, 10 cm tip to collector distance and 200 rpm rotating cylinder speed. The polymer concentration on the other hand was varied as 10, 15, 25 and 40 wt. %.

The SEM micrographs of the resulting samples can be seen in Figure 11. It can be clearly seen that PEG alone, cannot form fiber structure even at high electrospinning solution concentrations. This is due to the low molecular weight of the polymer. As the molecular entanglements are too low, the polymer cannot maintain a fiber structure but fragmentize into smaller micro particles. This experiment revealed that electrospinning of PEG did not result in polymer fibers.

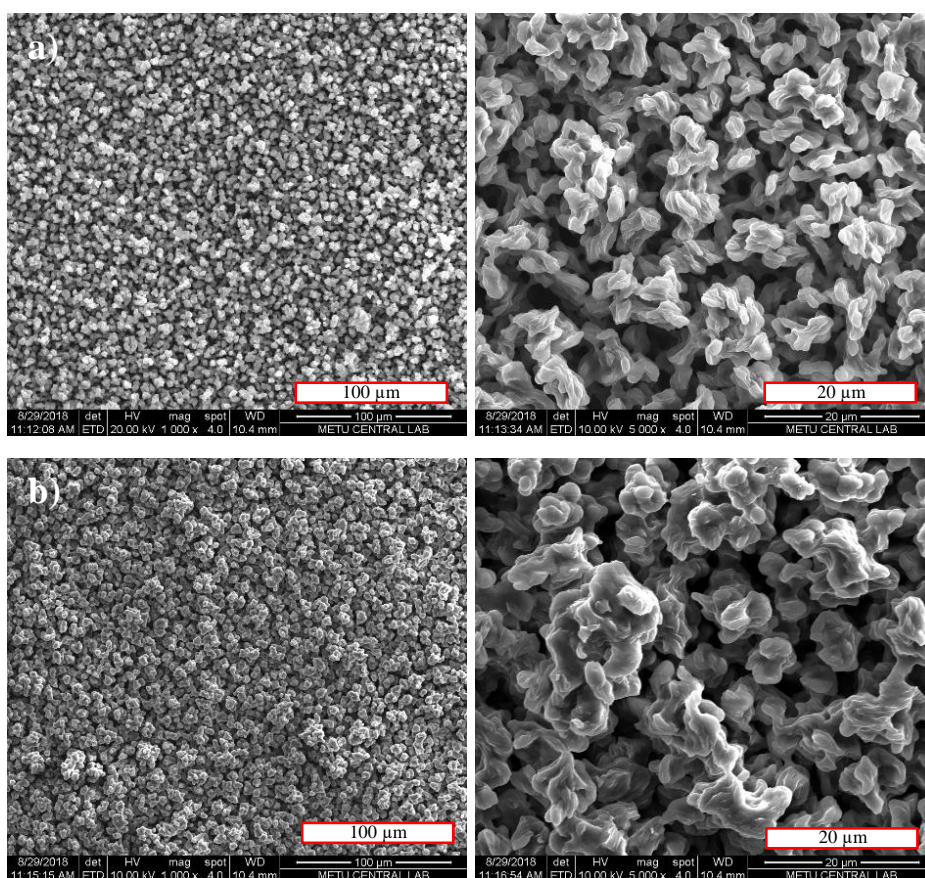


Figure 11. SEM micrographs of electrospun neat PEG with concentrations of a) 10, b) 15, c) 25 and d) 40 wt. % (AEP: 24 kV, TCD: 10 cm, SFR: 0.33 ml/h, CT: cylinder, RS: 200 rpm, ED: 30 min).

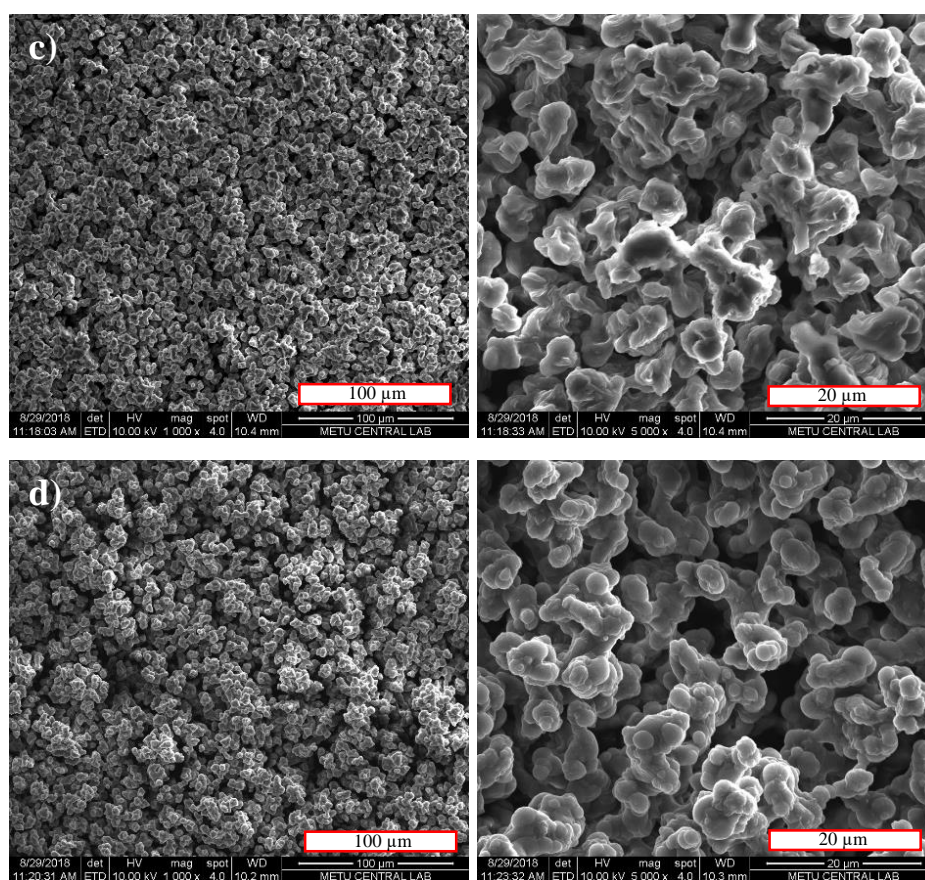


Figure 11. (continued) SEM micrographs of electrospun neat PEG with concentrations of a) 10, b) 15, c) 25 and d) 40 wt. % (AEP: 24 kV, TCD: 10 cm, SFR: 0.33 ml/h, CT: cylinder, RS: 200 rpm, ED: 30 min).

Although neat PEG was not able to preserve a fiber structure during the electrospinning process, from the previous studies it was known that ultra-fine, uniform PA6 nanofibers could be electrospun [7, 61]. Thus, in this study, for production of fine, uniform and core/shell structured PEG/PA6 nanofibers, optimization of coaxial electrospinning parameters were conducted. Afterwards, HNTs were introduced into the core structure and the multifunctional properties of the composite nanofibers were investigated. In the study by Şahin [62], electrospinning parameters for nanofiber production from PA6 were optimized. The optimum solvent system for electrospinning of PA6 fibers was found to be comprised of formic acid and acetic acid with volume ratio of 4:1. The formic acid was utilized in order to

dissolve PA6, but unstable spinning was present due to the high conductivity of the solvent. Acetic acid having lower dielectric constant, was added to the solvent system in order to obtain a stable electrospinning process. This solvent system was also used in PEG and PA6 core/shell solutions in this study. Core/shell solution concentrations were chosen to be 40 wt. % PEG and 10 wt. % PA6, respectively. The core/shell solution feed rates were 0.05 ml/h and 0.5 ml/h. The applied electrical potential was 24 kV, and tip to collector distance was 10 cm. The SEM micrographs of the coaxially electrospun PEG/PA6 nanofibers can be seen in Figure 12. The average fiber diameter of the coaxially electrospun nanofibers was measured and found to be 96 nm with standard deviation of  $\pm 17$  nm.

After smooth and uniform nanofiber production by using coaxial electrospinning method was obtained, the core/shell structure was investigated by using TEM analysis. The coaxial electrospinning parameters used in production of samples subjected to TEM imaging were as 40 wt. % PEG, 10 wt. % PA6 solution concentrations, 24 kV applied electrical potential, 0.3/0.9 ml/h core/shell solution feed rates and 10 cm of tip to collector distance. The TEM micrograph can be seen in Figure 13. As a result of the TEM analysis, it was seen that very distinct core structure was successfully formed inside the PA6 nanofibers. The difference in color between core and shell structure is a result of the density difference between PEG and PA6 polymers accompanied by thickness difference due to the PEG presence at particular locations inducing distinct electron beam diffractions during the imaging [61]. The darker color in the nanofibers suggests the PEG presence and the lighter color in the outer regions of the nanofibers is due to the PA6 presence.

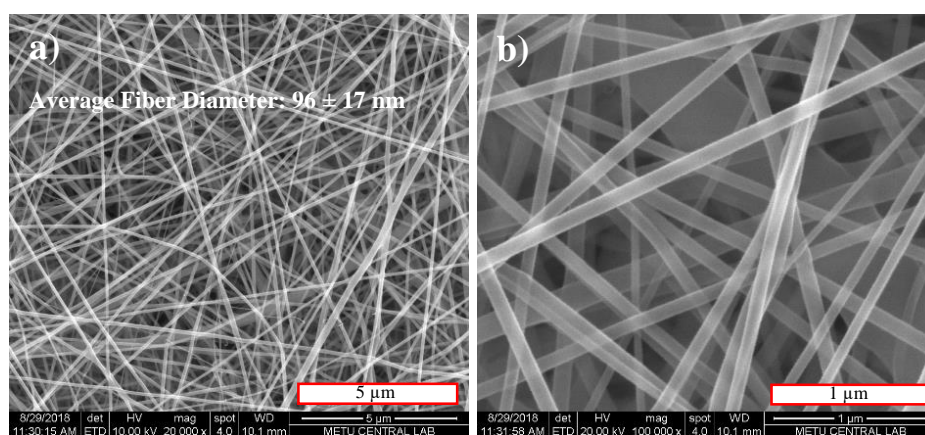


Figure 12. SEM micrographs of coaxially electrospun PEG/PA6 nanofibers with a) 20000x and b) 100000x magnifications (SC: 40 wt. % PEG/10 wt. % PA6, AEP: 24 kV, TCD: 10 cm, SFR: 0.05/0.5 ml/h, CT: cylinder, RS: 200 rpm, ED: 30 min).

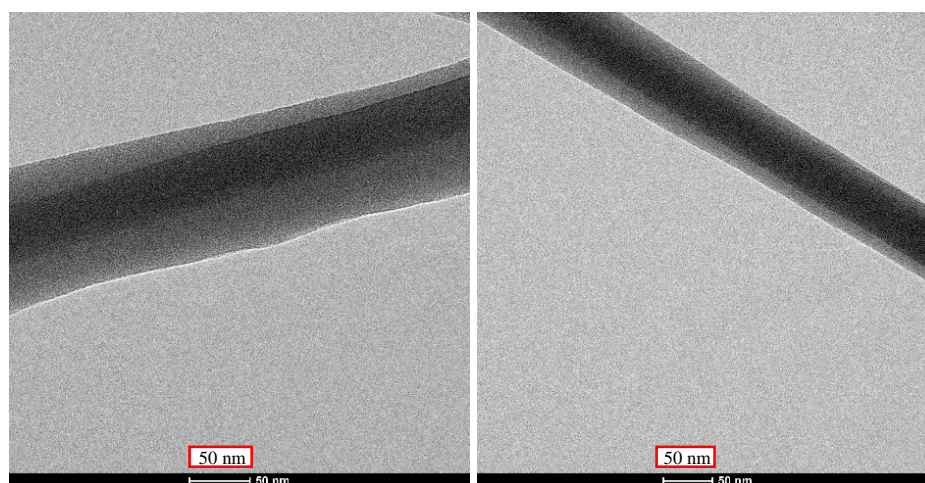


Figure 13. TEM images of coaxially electrospun PEG/PA6 nanofibers (SC: 40 wt. % PEG/10 wt. % PA6, AEP: 24 kV, TCD: 10 cm, SFR: 0.3/0.9 ml/h, CT: cylinder, RS: 200 rpm, ED: 3 sec).

#### 4.1.2. Solution Concentration Optimization

After the core/shell structure was obtained, optimization of the electrospinning parameters was done to increase the electrospinning efficiency and acquire smoother and uniform nanofibers. As a result of the literature survey and the preliminary experiments, it was found that among the electrospinning parameters, solution concentration, applied electrical potential and solution feed rates have the most significant effects on the final nanofiber morphology [60]. Thus, the first electrospinning parameter to be optimized was chosen as the solution concentration.

In order to determine the morphology, thermal stability, energy absorption characteristics and chemical structure of the nanofibers, several characterization methods such as SEM, TGA, DSC and FTIR were used.

#### **4.1.2.1. Scanning Electron Microscopy (SEM) Analysis**

The effect of core solution concentration on the fiber morphology was investigated by keeping the shell solution concentration, applied electrical potential, tip to collector distance and solution feed rates constant. During these experiments, the shell solution concentration was 12 wt. % PA6, applied electrical potential was 24 kV, core/shell solution feed rates were 0.1/0.3 ml/h and the tip to collector distance was 10 cm while core solution concentration was changed as 30, 40 and 50 wt. % PEG. The electrospinning experiments were conducted for half an hour using plate collector. The SEM micrographs of the resulting nanofibers can be seen in Figure 14 and the frequency distribution graph of the fiber diameter measurements is given in Figure B.1 in Appendix B. From the SEM analysis and the average fiber diameter measurements, it was seen that as the PEG concentration in the core solution increased from 30 to 50 wt. %, the average fiber diameter also increased without any significant change in the uniformity of the fibers. This was attributed to the increasing PEG solution viscosity with increasing polymer concentration. As the viscosity of the core solution increased, the molecular entanglements also increased which led to less stretching of the spinning solution during the electrospinning process. Thus, thicker nanofibers were produced [11, 61].

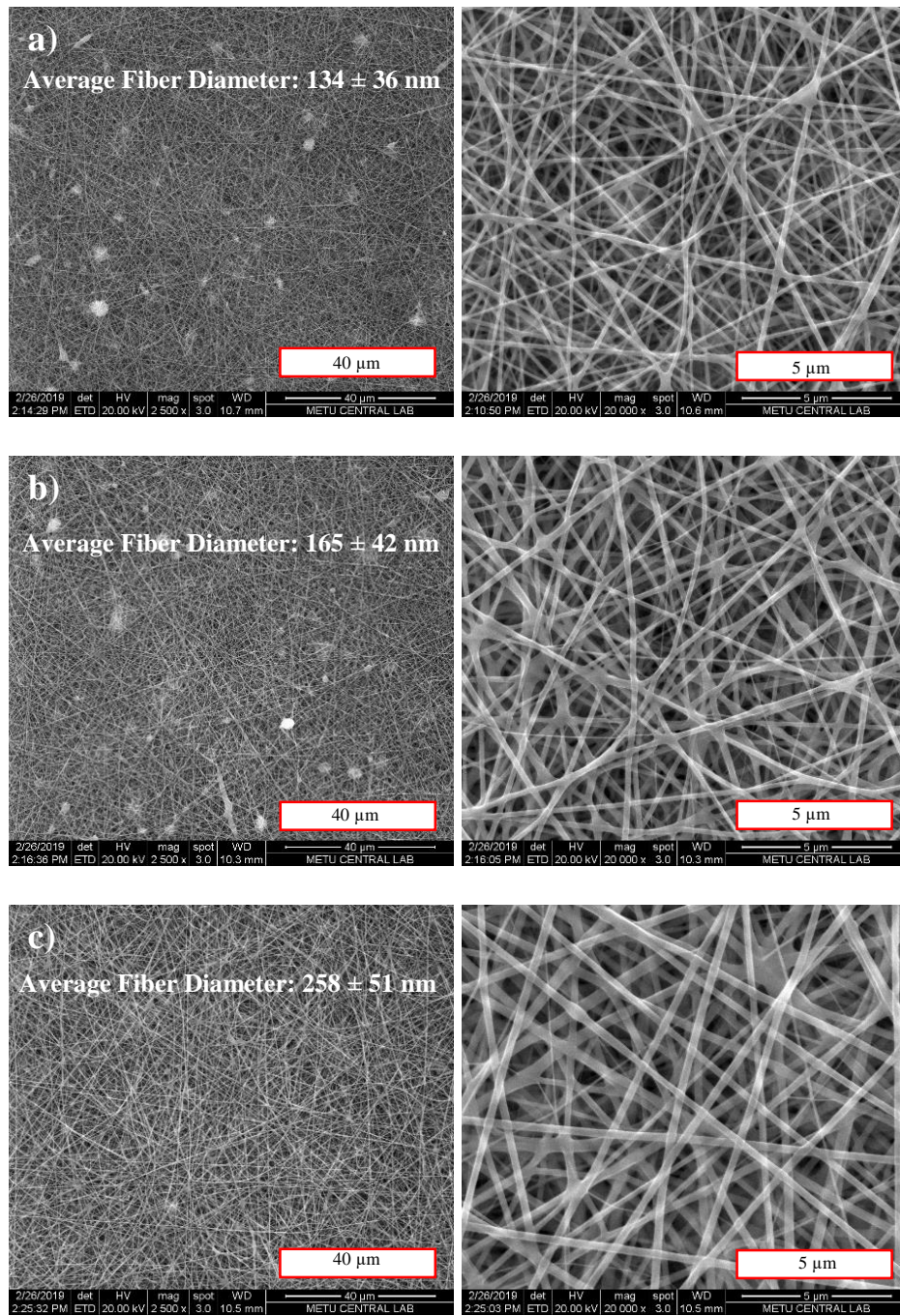


*Figure 14.* SEM micrographs of nanofibers electrospun with 12 wt. % PA6 in the shell solution and a) 30 wt. %, b) 40 wt. % and c) 50 wt. % PEG in the core solution (AEP: 24 kV, TCD: 10 cm, SFR: 0.1/0.3 ml/h, CT: plate, ED: 1 h).

After determining the effect of increasing core solution concentration on the nanofiber morphology, the effect of different shell solution concentrations was investigated by applying different core/shell solution concentrations. After this, by increasing the duration of experiment to one hour, the effect of electrospinning duration on the fiber morphology was also determined. All the other parameters were kept the same as in the previous experiment. The SEM micrographs of the resulting nanofibers can be seen in Figures 15-17. In Figure 15, the SEM images of the nanofibers produced by using 30 wt. % PEG as the core and 10, 12, 15 wt. % PA6 as the shell solution concentrations are illustrated. From the morphology analysis, it was observed that the average fiber diameters increased when the shell solution concentrations were increased while keeping the core solution concentrations constant. This effect can be observed in Figures 15-17 (a), (b) and (c). It can be seen in Figure 15 that at 30 wt. % PEG solution concentration, the average fiber diameter increased from 114 nm to 176 nm when the shell solution concentration was increased from 10 wt. % to 15 wt. % PA6. As can be seen in Figure 16, the most significant increase in fiber diameters occurred when 40 wt. % PEG was used as the core solution concentration. The average fiber diameter increased from 136 nm to 305 nm when the shell solution concentration was increased from 10 to 15 wt. % PA6. This increase was due to the higher level of entanglements in more concentrated PA6 solutions. As the molecular entanglements increased, more polymer was collected on the collector by Coulomb forces at unit time and less stretching occurred during the electrospinning process resulting in thicker nanofibers [6]. Ribbon shaped nanofibers were observed when the core solution concentrations were increased up to 40 wt. % PEG and 50 wt. % PEG as can be seen in Figures 16 and 17. This was due to the fast evaporation of the scarce solvent on the surface of the fibers. Fibers collapsed due to the evaporation of the solvent remaining inside the structure [49]. As can be seen in the bar chart in Figure 18 and frequency distribution graph in Figure B.1, when the PEG concentration was 40 and 50 wt. %, wide distribution in the nanofiber diameters was present. This was due to the fact that the core solution was not exposed to the electrostatic forces directly but the drag force between the core solution and the shell solution was the main force driving the PEG

onto the collector during the coaxial electrospinning method [13]. As the PEG concentration in the inner solution increased, the molecular chain mobility decreased which resulted in less PEG stretching during the electrospinning process. Thus, instable Taylor cone was formed leading to formation of non-uniform nanofiber structures. The uniformity of the nanofibers produced by using different core/shell solution concentrations can be evaluated from the bar chart in Figure 18 and frequency distribution graph in Figure B.1. The increase in standard deviations of the average fiber diameter measurements depicted in Figure 18 and the widening of the frequency distribution curves in Figure B.1 can be considered as proof of the negative effect of excess core solution concentration on the nanofiber uniformity.

Additionally, by increasing the electrospinning duration from half an hour to an hour, the stability of the process was evaluated. In order to see the time effect more clearly, the 30, 40 and 50 wt. % PEG was electrospun with 12 wt. % PA6 concentration in the shell solution for an hour. It can be seen from Figure 18 that the uniformity of the nanofibers decreased as the electrospinning time was extended. The standard deviation values increased with increasing electrospinning duration. Meaning that the variation in the diameter values of the produced nanofibers increased. This was due to the decrease in effect of coulomb forces on the polymer solution since accumulation of polymer on the collector acted as an insulating coating. More polymer accumulated on the collector as the electrospinning duration was extended resulting in better insulation effect. It was also seen from Figure 18 that as the PEG concentration increased, non-uniformity also increased at prolonged electrospinning duration. Both average fiber diameter and standard deviation values increased as the PEG concentration was increased. Also the variances in average fiber diameter values were more significant with increasing electrospinning duration when high PEG concentrations were utilized in the core solution. This was due to the fact that as the reduced molecular chain mobility and electrostatic forces occurred, stretching the core solution by drag force during the electrospinning process became difficult. When the uniformity of the nanofibers produced at both 30 minutes and 1-hour experiment times were considered,

the most stable electrospinning was decided to be achieved by using 30 wt. % PEG and 12 wt. % PA6 core/shell solution concentrations.

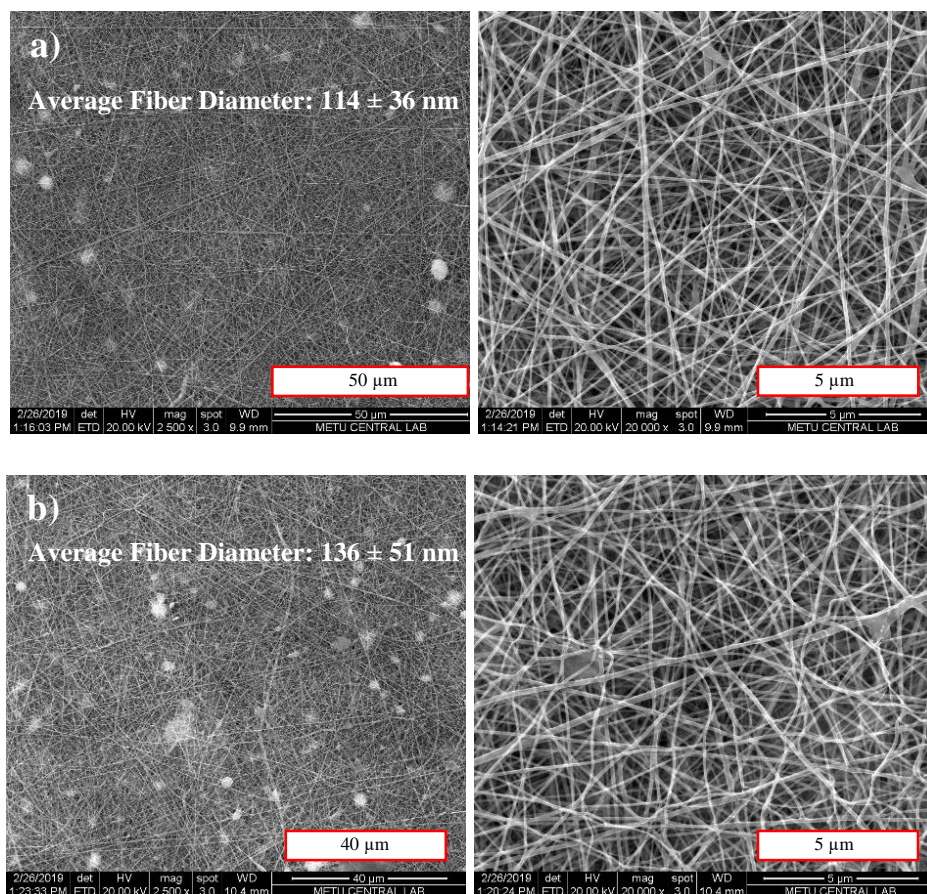


*Figure 15.* SEM micrographs of nanofibers electrospun by using solutions with 30 wt. % PEG core and a) 10 wt. %, b) 12 wt. %, c) 15 wt. % PA6 concentrations (AEP: 24 kV, TCD: 10 cm, SFR: 0.1/0.3 ml/h, CT: plate, ED: 1 h).

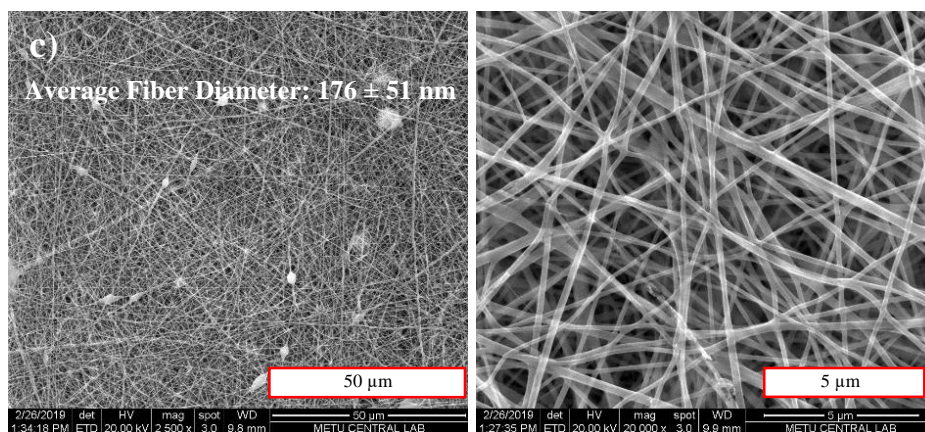


Figure 15. (continued) SEM micrographs of nanofibers electrospun by using solutions with 30 wt. % PEG core and a) 10 wt. %, b) 12 wt. %, c) 15 wt. % PA6 concentrations (AEP: 24 kV, TCD: 10 cm, SFR: 0.1/0.3 ml/h, CT: plate, ED: 1 h).

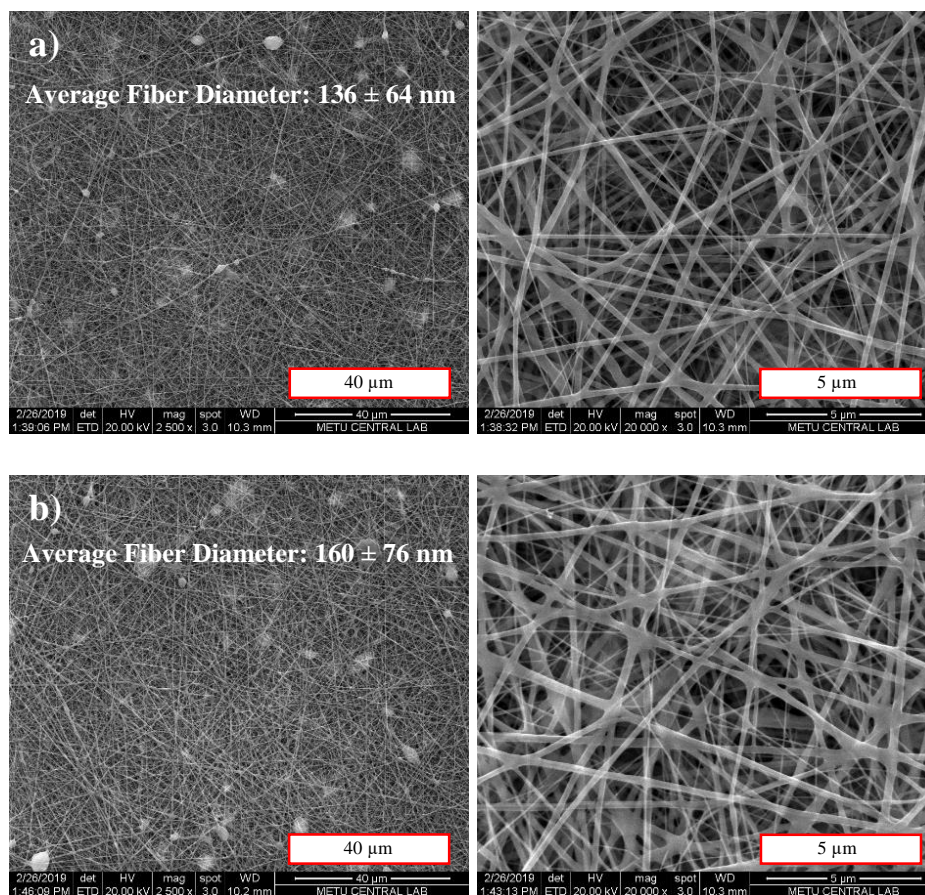


Figure 16. SEM micrographs of nanofibers electrospun by using solutions with 40 wt. % PEG core and a) 10 wt. %, b) 12 wt. %, c) 15 wt. % PA6 concentrations (AEP: 24 kV, TCD: 10 cm, SFR: 0.1/0.3 ml/h, CT: plate, ED: 1 h).

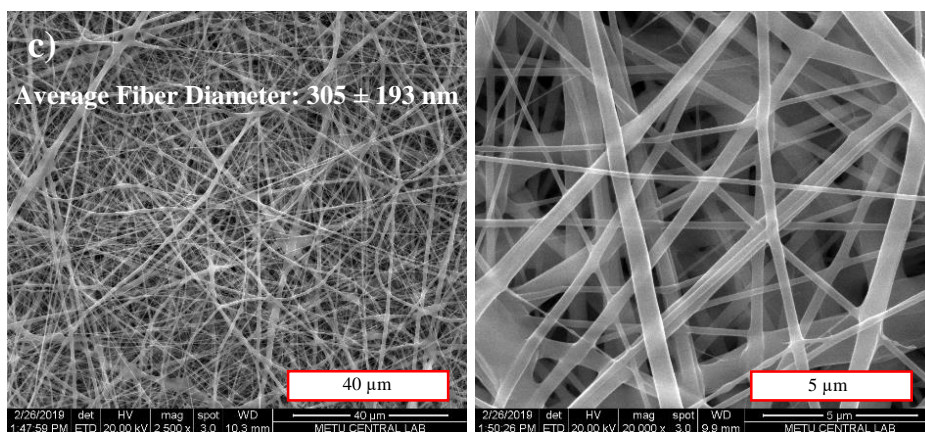


Figure 16. (continued) SEM micrographs of nanofibers electrospun by using solutions with 40 wt. % PEG core and a) 10 wt. %, b) 12 wt. %, c) 15 wt. % PA6 concentrations (AEP: 24 kV, TCD: 10 cm, SFR: 0.1/0.3 ml/h, CT: plate, ED: 1 h).

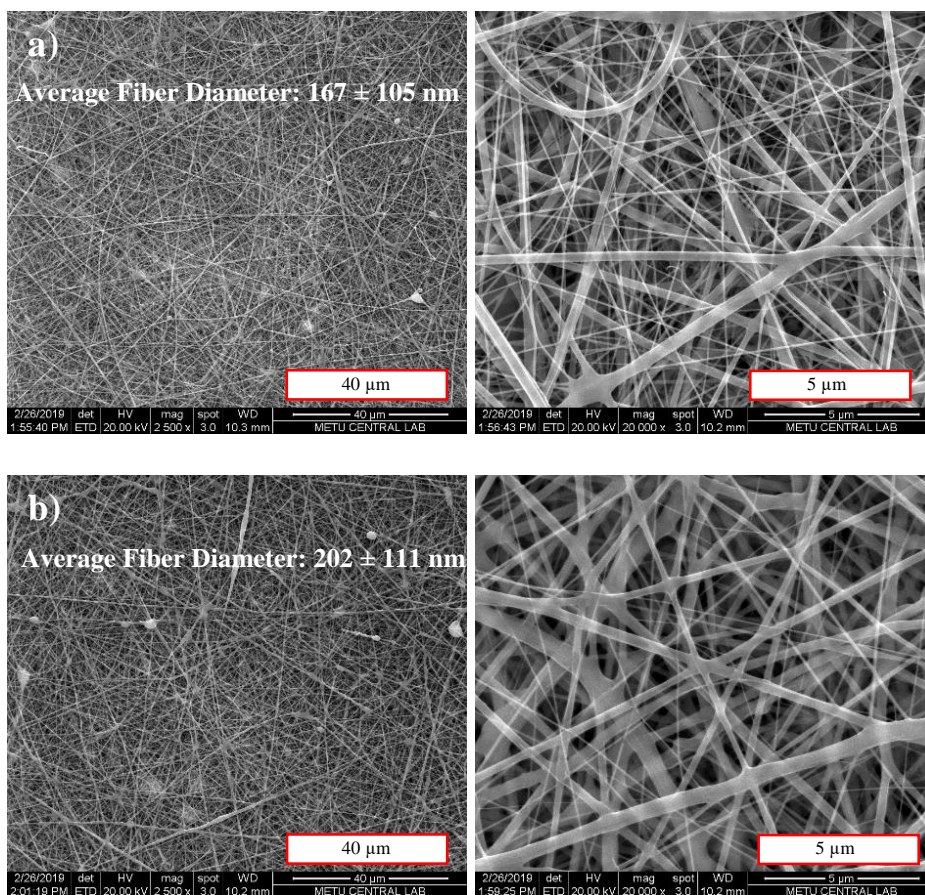


Figure 17. SEM micrographs of nanofibers electrospun by using solutions with 50 wt. % PEG core and a) 10 wt. %, b) 12 wt. %, c) 15 wt. % PA6 concentrations. (AEP: 24 kV, TCD: 10 cm, SFR: 0.1/0.3 ml/h, CT: plate, ED: 1 h)

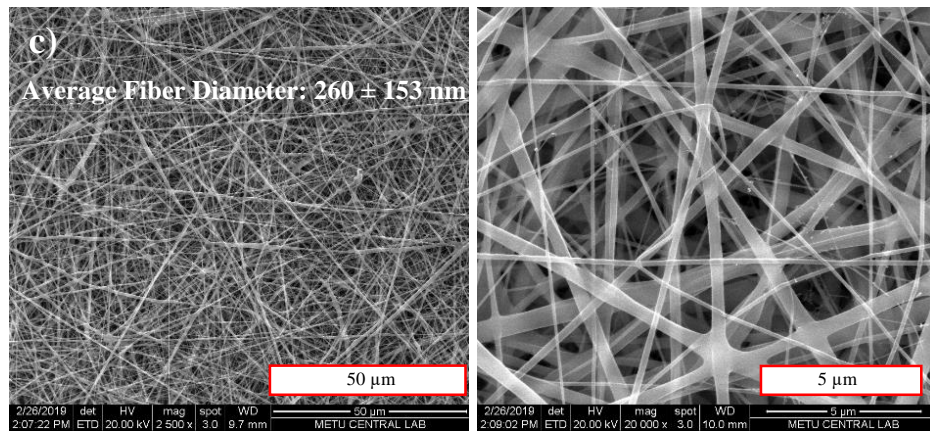


Figure 17. (continued) SEM micrographs of nanofibers electrospun by using solutions with 50 wt. % PEG core and a) 10 wt. %, b) 12 wt. %, c) 15 wt. % PA6 concentrations. (AEP: 24 kV, TCD: 10 cm, SFR: 0.1/0.3 ml/h, CT: plate, ED: 1 h)

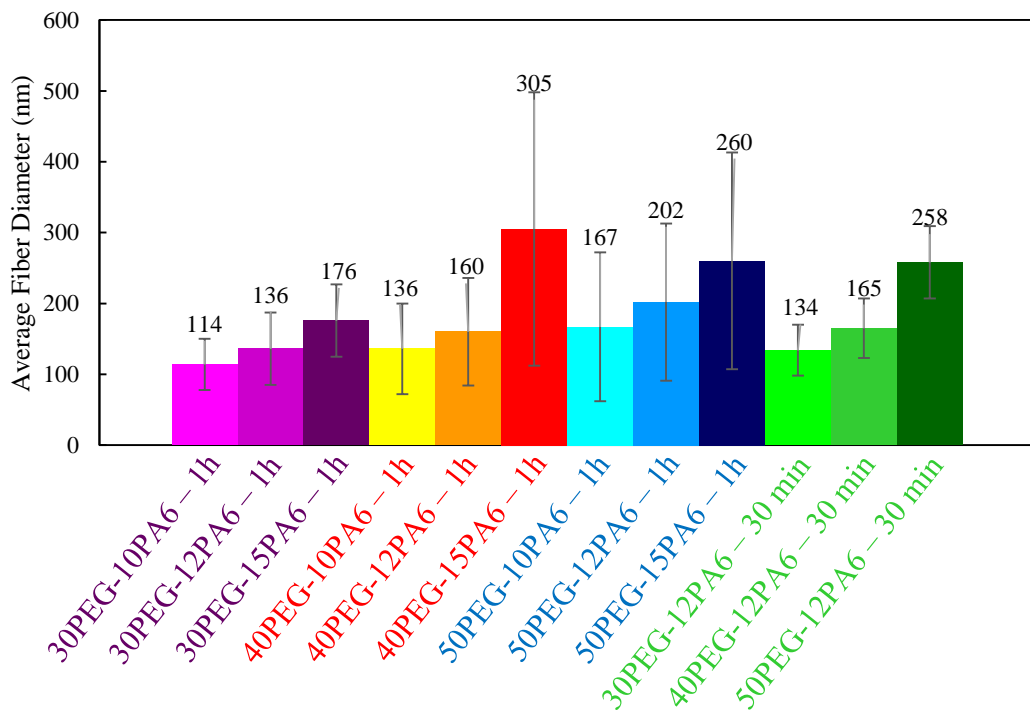


Figure 18. Bar chart depicting the average fiber diameters of the nanofibers produced from different electrospinning solutions (AEP: 24 kV, TCD: 10 cm, SFR: 0.1/0.3 ml/h, CT: plate).

#### 4.1.2.2. Thermogravimetric Analysis (TGA)

Thermogravimetric analysis was performed to the samples produced with 12 wt. % PA6 as the shell, 30, 40 and 50 wt. % PEG as the core solutions concentrations, 24 kV of applied electrical potential, 0.1/0.3 ml/h core/shell feed rates and 10 cm tip to collector distance in order to investigate the thermal stability of the nanofibrous samples produced with different core solution concentrations. The decomposition temperatures of the samples were taken to be at the peak value of the 1<sup>st</sup> order derivative curve obtained from percent mass loss data with respect to temperature increase. Weight percent versus temperature graphs of neat PEG flakes, neat PA6 fibers and coaxially electrospun samples can be seen in Figure 19. The decomposition temperature of the neat PEG flakes was found to be 400°C and the neat PA6 nanofibers produced by using the same electrospinning parameters as the rest of the experiments revealed a decomposition temperature of 453°C. All of the coaxially electrospun samples showed similar decomposition characteristics. The decomposition temperature of the nanofibrous samples were around 425°C. The single weight loss characteristic of the coaxially electrospun samples at temperatures between the decomposition temperature of the neat materials reveals that decomposition temperatures of the fiber constituents were relatively close to each other [62]. In Table 9, it can be seen that the decomposition temperature of nanofibrous sample 30PEG/12PA6 was 426°C, whereas the sample 50PEG/12PA6 had a decomposition temperature of 423°C. Although no significant change was present, the increasing amount of PEG in the nanofibrous structure with increasing core solution concentration resulted in slight decrease in decomposition temperature.

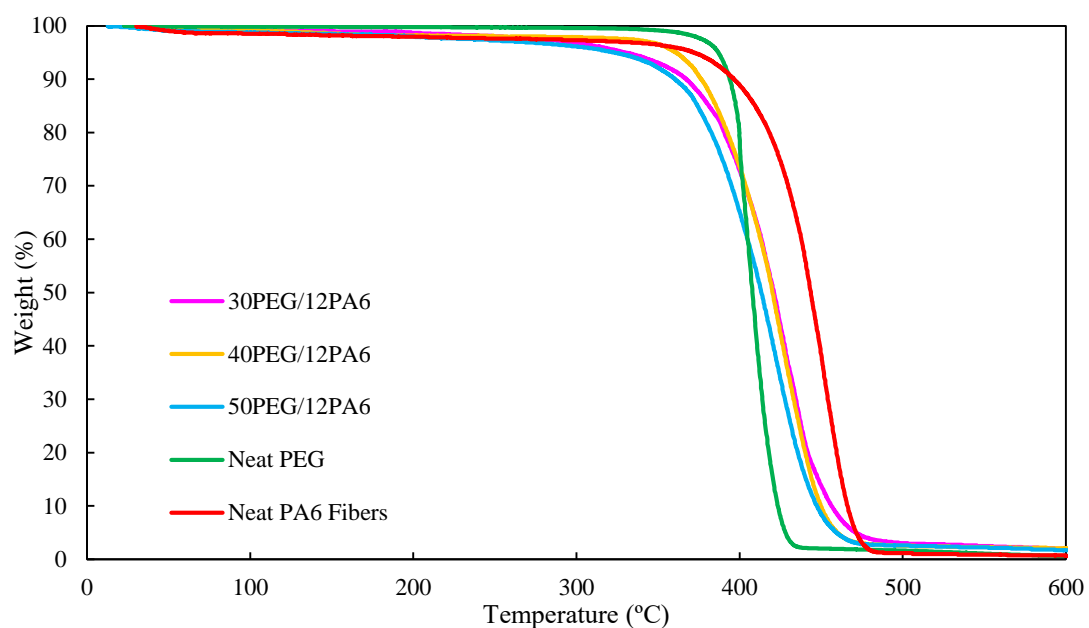


Figure 19. TGA curves of nanofibers produced by coaxial electrospinning with different core solution concentrations (AEP: 24 kV, TCD: 10 cm, SFR: 0.1/0.3 ml/h, CT: plate, ED: 30 min).

Table 9. Decomposition temperature data of the samples produced by using different solution concentrations (AEP: 24 kV, TCD: 10 cm, SFR: 0.1/0.3 ml/h, CT: plate, ED: 30 min).

Sample	Decomposition Temperature (°C)
Neat PA6 Fibers	453
Neat PEG	400
30PEG/12PA6	426
40PEG/12PA6	427
50PEG/12PA6	423

#### 4.1.2.3. Differential Scanning Calorimetry (DSC) Analysis

DSC analysis was performed to determine the effect of PEG concentration in the core solution on the melting temperature and the enthalpy of the coaxially electrospun samples. The melting onset, peak, endset temperatures, the melting enthalpies of the neat PEG and PEG encapsulation efficiency values of the core/shell nanofibers are given in Table 10.

Results indicated that the enthalpy of melting was decreased significantly in electrospun samples with respect to neat PEG. This was due to the fact that during electrospinning process, solidification of PEG took place in a very short moment that it limited the degree of crystallization [41, 3]. Additionally, presence of PA6 in the samples acted as a diluent in terms of melting enthalpy values of the samples. Thus, lower melting enthalpy values were observed for electrospun samples [10]. Moreover, PA6 has glass transition temperature at about 45°C, but from the DSC curve analysis it was seen that the onset temperature of the PEG melting was higher than this value in all samples. Thus presence of PA6 did not affect the melting enthalpy values acquired from the sample at 60°C. On the other hand, it can be seen from the DSC analysis results that the melting enthalpy increased with increasing PEG concentration in the core solution. The higher amount of PEG in the nanofibrous sample resulted in higher melting enthalpy since PA6 does not melt at the same temperature as PEG, thus did not contribute to the energy absorption at the specific temperature. It can be seen in Table 10 that PA6 has a melting enthalpy value of 83 J/g at 222°C. On the other hand, no significant change in the melting temperature of PEG was observed with changing core solution concentration. PEG encapsulation efficiency values reveal that as the PEG solution concentration increased the experimental melting enthalpy value of the sample was closer to the theoretical value which is calculated by multiplying the calculated PEG amount in the samples and melting enthalpy of the neat PEG (210 J/g) shown in Equation 3.6 [64]. For example, the theoretical melting enthalpy of the neat core/shell structured nanofibrous sample produced by using 30 wt. % PEG (PEG content: 46%) and 12 wt. % PA6 solution concentrations is calculated as 96.6 J/g. The ratio of experimental latent heat of melting result belonging to the above mentioned sample (76 J/g) and theoretical latent heat of melting (96.6 J/g) was found to be 80%.

Table 10. DSC data of neat PEG and coaxially electrospun nanofibers from different core solution concentrations (AEP: 24 kV, TCD: 10 cm, SFR: 0.1/0.3 ml/h, CT: plate, ED: 30 min).

Samples	Melting Temperature (°C)			Latent Heat of Melting (J/g)	PEG Encapsulation Efficiency (%)
	Onset	Peak	Endset		
Neat PA6 Fibers	213	222	229	83	-
Neat PEG	58	64	70	210	100
30PEG/12PA6	51	59	67	76	80
40PEG/12PA6	51	58	66	99	89
50PEG/12PA6	52	60	69	113	92

#### 4.1.2.4. Fourier Transform Infrared (FTIR) Spectroscopy

FTIR analysis was conducted on neat PEG, PA6 fibers and coaxially electrospun nanofibers in order to determine the changes in their chemical structure after electrospinning process. The FTIR spectra of the samples produced with 12 wt. % PA6 in the core, 30, 40, 50 wt. % PEG in the shell solution, 24 kV applied electrical potential, 01/0.3 ml/h core/shell feed rate and 10 cm tip to collector distance can be seen in Figure 20. The characteristic FTIR peaks of PA6 and PEG are given in Table 11. It can be seen from the FTIR spectra of the electrospun samples that the characteristic peaks of PA6 such as at  $3300\text{ cm}^{-1}$  corresponding to N-H stretching, at  $2930\text{ cm}^{-1}$  and  $2858\text{ cm}^{-1}$  belonging to  $\text{CH}_2$  axial deformation are present in all the nanofibrous samples suggesting presence of PA6 as expected. The characteristic peaks of PEG such as at  $1097$ ,  $960$  and  $1466\text{ cm}^{-1}$  corresponding to C-O, C-C stretching,  $\text{CH}_2$  twisting and  $\text{CH}_2$  scissoring were present in all nanofibrous samples. This was due to the fact that PEG was not fully encapsulated but a trace of PEG was also present on the surface of the nanofibers. Additionally, the triple peaks between  $1000$  and  $1200\text{ cm}^{-1}$  which was also present in all the FTIR spectra suggested the presence of crystalline PEG region [65]. FTIR peaks of PEG between  $840$  and  $1540\text{ cm}^{-1}$  were observed as expected in all samples and can be seen in Figure 20 (b).

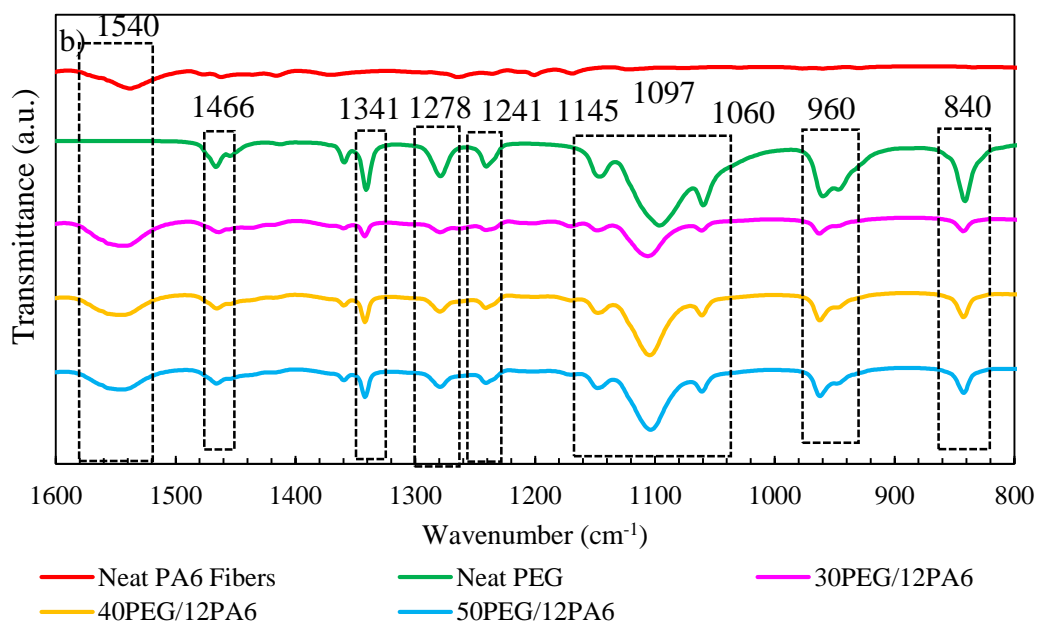
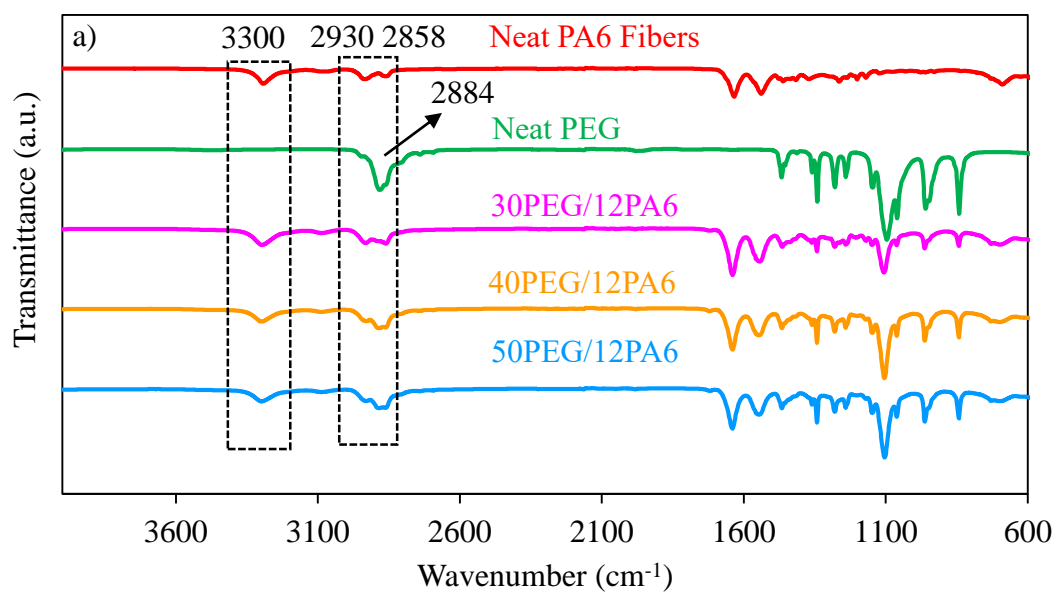


Figure 20. a) FTIR spectra and b) zoomed FTIR spectra of neat PA6 fibers, PEG flakes and electrospun samples by using 30, 40, 50 wt. % PEG in the core solution and 12 wt. % PA6 in the shell solution (AEP: 24 kV, TCD: 10 cm, SFR: 0.1/0.3 ml/h, CT: plate, ED: 30 min).

Table 11. Characteristic FTIR peaks of PA6 and PEG [65, 66, 67].

Wavenumber (cm <sup>-1</sup> )	Definition	Polymer
840, 1060, 1097	C-O, C-C stretching, CH <sub>2</sub> vibration	PEG
951	Absorption peak of -CH <sub>2</sub> - bond	PEG
1145	CH <sub>2</sub> vibration	PEG
1201	Amide III, crystalline peak	PA6
1263	C-O stretching	PA6
960, 1241, 1278	CH <sub>2</sub> twisting	PEG
1341	CH <sub>2</sub> vibration	PEG
1460	C=C atomic stretching	PA6
1466	CH <sub>2</sub> scissoring	PEG
1540	N-H bending vibration and C-N axial deformation	PA6
1640	C=O axial deformation, amide I	PA6
2858	CH <sub>2</sub> axial deformation	PA6
2884	Absorption peak of C-O bond	PEG
2930	CH <sub>2</sub> axial deformation	PA6
3080	N-H angular deformation	PA6
3300	N-H stretching	PA6

#### 4.1.3. Applied Electrical Potential Optimization

After determination of the optimum solution concentrations for production of more uniform nanofibers via coaxial electrospinning method, the second most significant parameter which is “applied electrical potential” was optimized. The most promising core and shell solution concentrations were chosen to be 30 wt. % PEG, 12 wt. % PA6 as the core/shell solution concentrations and used in all applied electrical potential optimization experiments. The feed rates were determined to be 0.1/0.3 ml/h for the core/shell solutions and the tip to collector distance was 10 cm for all the nanofiber productions. Electrospinning was conducted for half an hour for all experiments. Before starting the experiments, minimum and maximum values for applied electrical potentials were determined by preliminary experiments. Under 20 kV, the electrostatic forces applied on the PA6 solution in the needle tip was not sufficient to ensure an efficient and stable electrospinning process but was enough to overcome the surface tension of the PA6 solution at the needle tip. Thus, the Taylor cone hardly formed and

easily lost its form resulting in very little amount of fiber production per unit time. On the other hand, above 28 kV of applied electrical potential, the Taylor cone was highly instable often resulting in electrospaying or multi cone formation. This instability was the reason behind increased standard deviation values in average fiber diameter measurements.

#### **4.1.3.1. Scanning Electron Microscopy (SEM) Analysis**

The SEM analysis results of the samples produced by using 12 wt. % PA6 in the core, 30 wt. % PEG in the shell solution, 20, 24 and 28 kV of applied electrical potentials, 0.1/0.3 ml/h core/shell solution feed rates, 10 cm tip to collector distance are given in Figure 21 (a), (b) and (c), respectively. After SEM imaging of the electrospun samples, it was seen that under insufficient and excess electrostatic forces, a stable Taylor cone could not be formed. This resulted in non-uniform nanofiber structures. Nanofibrous morphology of the sample produced under 20 kV of applied electrical potential can be seen in Figure 21 (a). In the case of 20 kV applied electrical potential, the resulting nanofibers were thicker with respect to the ones produced with higher voltages. Due to the insufficient electrostatic forces, less stretching occurred during the electrospinning process, resulting in thicker nanofibers [66]. Also instability of the Taylor cone under such condition resulted in formation of too thick and too thin nanofibers. At this voltage, average fiber diameter was found to be 186 nm with standard deviation of  $\pm 72$  nm. When the applied electrical potential was adjusted to 28 kV, formation of more than one Taylor cone was observed. This was due to the excess electrostatic forces subjected on the PA6 solution. As can be seen in Figure 21 (c), very thin nanofibers were produced besides thick ones. This was due to the formation of multiple instable Taylor cones. Since excess electrostatic forces were acting on the PA6 solution during the process, the stretching of the electrospinning solution was increased resulting in thinner nanofibers [69, 70]. The average fiber diameter under 28 kV applied electrical potential was measured to be 147 nm with standard deviation of 63 nm. Finally, under 24 kV of applied electrical potential, the electrostatic forces were just enough to overcome the surface tension of the solution

and preserve a stable Taylor cone. Thus more uniform nanofiber morphology was produced. The resulting morphology can be seen in Figure 21 c-d). Average fiber diameter was measured to be 134 nm with a standard deviation of 36 nm. The bar chart depicting the average fiber diameters are given in Figure 22. Also, frequency distribution graph of the fiber diameter measurements is given in Figure B.2 in Appendix B.

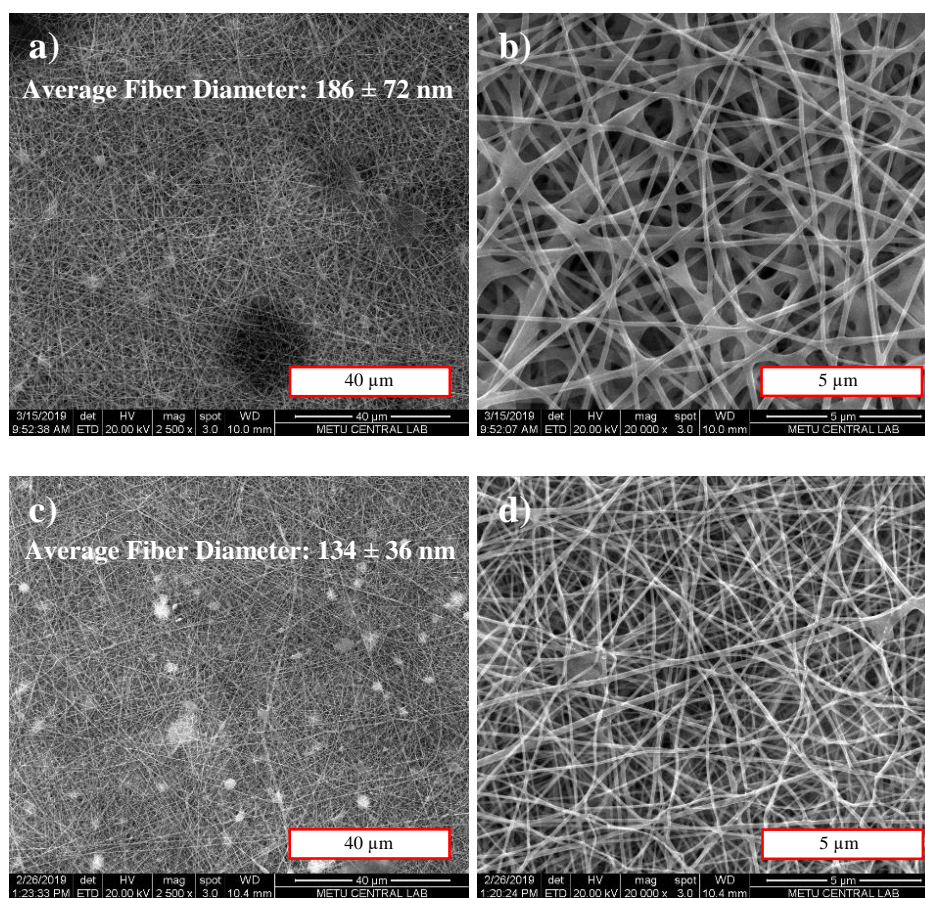


*Figure 21.* SEM micrographs of electrospun nanofibers under a-b) 20 kV, c-d) 24 kV, e-f) 28 kV electrical potential difference with 2500x and 20000x magnifications, respectively (SC: 30 wt. % PEG/12 wt. % PA6, TCD: 10 cm, SFR: 0.1/0.3 ml/h, CT: plate, ED: 30 min).

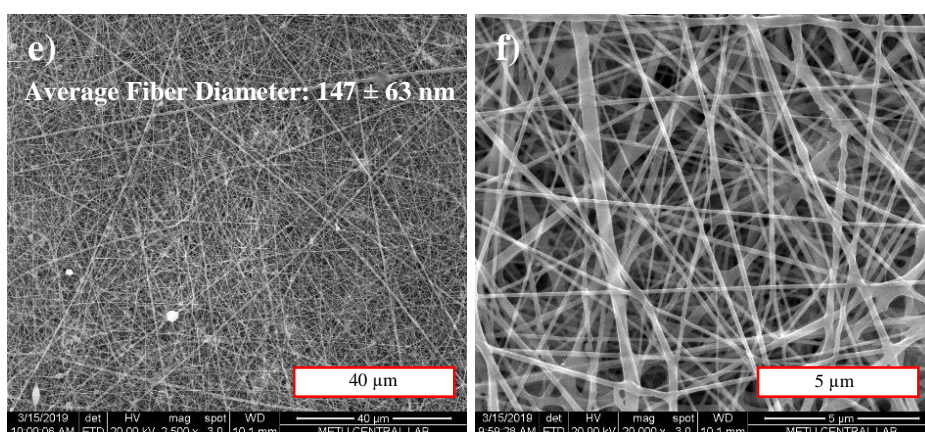


Figure 21. (continued) SEM micrographs of electrospun nanofibers under a-b) 20 kV, c-d) 24 kV, e-f) 28 kV electrical potential difference with 2500x and 20000x magnifications, respectively (SC: 30 wt. % PEG/12 wt. % PA6, TCD: 10 cm, SFR: 0.1/0.3 ml/h, CT: plate, ED: 30 min).

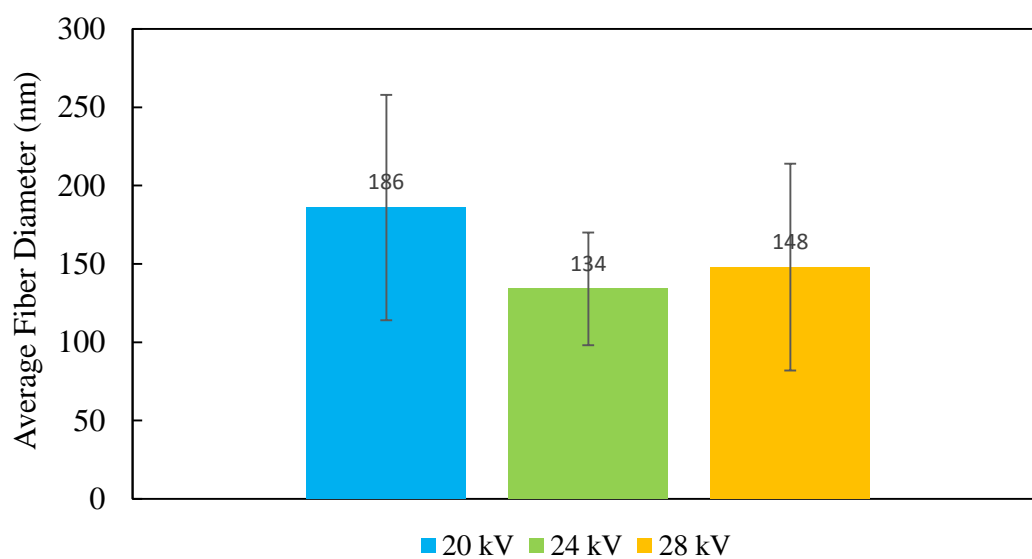


Figure 22. Bar chart depicting the diameter distribution of the nanofibers produced under 20, 24 and 28 kV of applied electrical potentials (SC: 30 wt. % PEG/12 wt. % PA6, TCD: 10 cm, SFR: 0.1/0.3 ml/h, CT: plate, ED: 30 min).

#### 4.1.3.2. Thermogravimetric Analysis (TGA)

In order to determine the thermal stability of the samples produced under different applied electrical potentials, thermogravimetric analysis was conducted. The TGA results and the weight percent versus temperature curves of the samples can be seen in Table 12 and Figure 23, respectively. In addition to neat PEG and PA6 fibers, the decomposition temperatures of samples produced with 12 wt. % PA6 in the shell, 30 wt. % PEG in the core solution, 20, 24, 28 kV of applied electrical potentials, 0.1/0.3 ml/h core/shell solution feed rates and 10 cm tip to collector distance are given in Table 12. As observed in solution concentration optimization experiments, the core/shell structured nanofibers produced under different electrical potentials had single drop in their masses at temperatures between the degradation temperature of neat PEG and PA6 fibers. This was due to the mass loss of two different materials with relatively close degradation temperatures acting at the same time. The decomposition temperature of the sample produced under 20 kV electrical potential difference is higher than the other electrospun samples. This can be explained by the dynamics of the coaxial electrospinning method. Since the electrostatic forces are only exerted on the outer solution during electrospinning, the inner solution is only collected by the drag forces exerted by the outer solution [13]. In the case of insufficient electrostatic forces, the shell solution cannot exert enough drag force to overcome the surface tension of the inner solution. Thus the fibers are mainly formed from the shell material [66]. In this case, the fibers were mainly comprised of PA6 so the degradation temperature was closer to the degradation temperature of the neat PA6 fibers. Fibers produced under 24 and 28 kV showed similar thermal stability characteristics with decomposition temperature of 426°C.

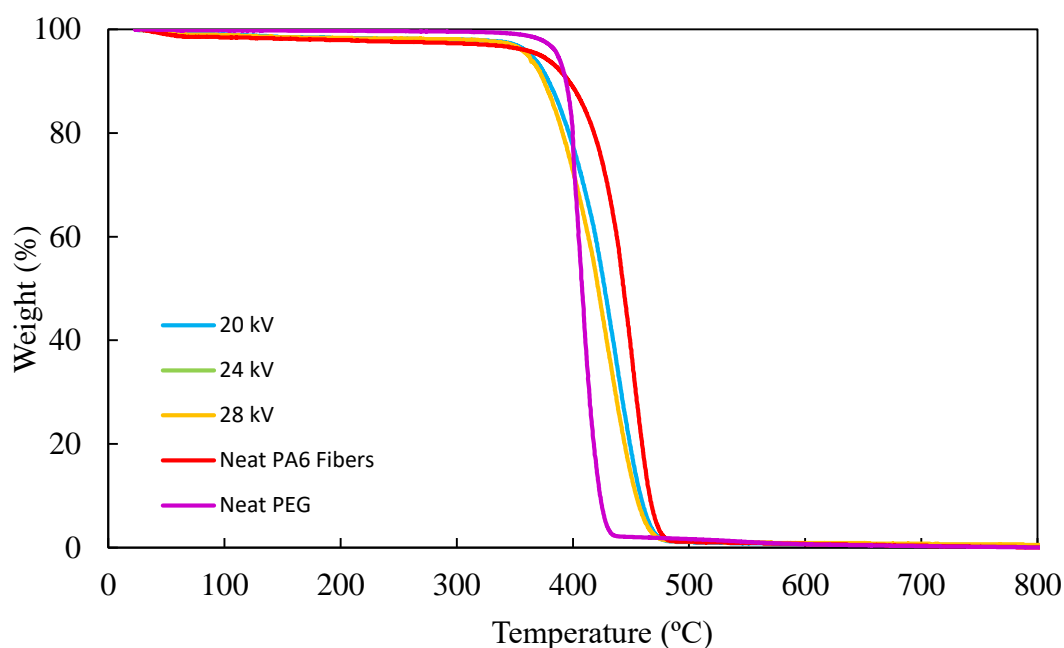


Figure 23. TGA graph of samples produced under 20, 24 and 28 kV of applied electrical potentials with 30 wt. % PEG/ 12 wt. % PA6 core/shell solution concentrations (SC: 30 wt. % PEG/12 wt. % PA6, TCD: 10 cm, SFR: 0.1/0.3 ml/h, CT: plate, ED: 30 min).

Table 12. Decomposition temperatures of samples produced under 20, 24 and 28 kV of applied electrical potentials (SC: 30 wt. % PEG/12 wt. % PA6, TCD: 10 cm, SFR: 0.1/0.3 ml/h, CT: plate, ED: 30 min).

Sample	Decomposition Temperature (°C)
Neat PA6 Fibers	453
Neat PEG	400
30PEG/12PA6 – 20 kV	438
30PEG/12PA6 – 24 kV	426
30PEG/12PA6 – 28 kV	426

#### 4.1.3.3. Differential Scanning Calorimetry (DSC) Analysis

Differential scanning calorimetry analysis was performed on the samples electrospun under different electrical potentials to observe the changes in melting characteristics of the PEG content of the samples. The DSC data of the samples can be seen in Table 13. The results suggest that the sample produced under 24 kV of electrical potential difference showed highest melting enthalpy value with 76 J/g. Since the electrostatic

forces were insufficient to exert enough driving force onto PA6 solution to drag enough PEG along with itself into the fibrous structure under 20 kV of electrical potential difference, the latent heat of the sample was lower than the others. When 28 kV of electrical potential difference was applied onto the solutions, due to the excess electrostatic forces exerted on the PA6 solution no stable Taylor cone was present and less PEG could be dragged into the nanofiber structure. Thus, excess applied electrical potential during electrospinning resulted in lower melting enthalpy value than the case of 24 kV. The melting temperatures of PEG again showed a decrease with respect to the neat PEG due to the lower level of crystallinity. But no significant effect of applied electrical potential during the electrospinning process on the melting temperatures was observed. PEG encapsulation efficiency values reveal that when 24 kV of electrical potential was applied during coaxial electrospinning, the experimental melting enthalpy value of the sample was closer to the theoretical one determined by multiplying the melting enthalpy of neat PEG with calculated PEG content of the samples. Thus, when the electrospinning was conducted under 24 kV, the PEG encapsulation efficiency value was 80%. On the other hand, when 20 and 28 kV of applied electrical potential was used, this value was 63 and 75%, respectively.

Table 13. DSC data of electrospun samples produced under 20, 24 and 28 kV of applied electrical potentials (SC: 30 wt. % PEG/12 wt. % PA6, TCD: 10 cm, SFR: 0.1/0.3 ml/h, CT: plate, ED: 30 min).

Samples	Melting Temperature (°C)			Latent Heat of Melting (J/g)	PEG Encapsulation Efficiency (%)
	Onset	Peak	Endset		
Neat PA6 Fibers	213	222	229	83	-
Neat PEG	58	64	70	210	100
30PEG/12PA6-20 kV	52	59	67	61	63
30PEG/12PA6-24 kV	51	59	67	76	80
30PEG/12PA6-28 kV	53	60	69	72	75

#### 4.1.3.4. Fourier Transform Infrared Spectroscopy (FTIR) Analysis

The FTIR spectra of the electrospun samples produced under different electrical potentials are given in Figures 24 and 25. When the FTIR spectra of the samples were analyzed, it can be seen that the electrospun samples had the characteristic peaks of PA6 such as the ones at wavenumbers of 1640, 3300, 2930, 2858, 1540  $\text{cm}^{-1}$  corresponding to C=O axial deformation, N-H stretching,  $\text{CH}_2$  axial deformation and N-H bending vibration or C-N axial deformation, respectively. Observation of the characteristic peaks of PA6 is desired since encapsulation of PEG is the main objective, but the resulting FTIR spectra also showed traces of characteristic peaks of PEG. For example, peaks at wavenumbers between 1000-1200  $\text{cm}^{-1}$  indicating the crystalline region in PEG suggested that full encapsulation is not the case [65]. On the contrary, resulting FTIR spectra indicated that some of the electrospun PEG resided at the surface of the nanofibers due to the lack of encapsulation, forming a blend with PA6. But the low intensity values of the characteristic peaks at 1060, 1097 and 1145  $\text{cm}^{-1}$  corresponding to C-O, C-C stretching and  $\text{CH}_2$  vibration indicated that the amount of PEG on the surface decreased as the applied electrical potential was optimized. When the applied electrical potential was 20 kV, the characteristic peaks of PEG at 1060, 1097 and 1145  $\text{cm}^{-1}$  had the lowest intensity which was also in parallel with the DSC analysis results. On the other hand, when the FTIR spectrum of the sample produced under 28 kV of electrical potential difference was analyzed it could be clearly seen that the characteristic peaks of PEG at 1060, 1097 and 1145  $\text{cm}^{-1}$  again had lower intensity values with respect to the sample produced under 24 kV applied electrical potential difference.

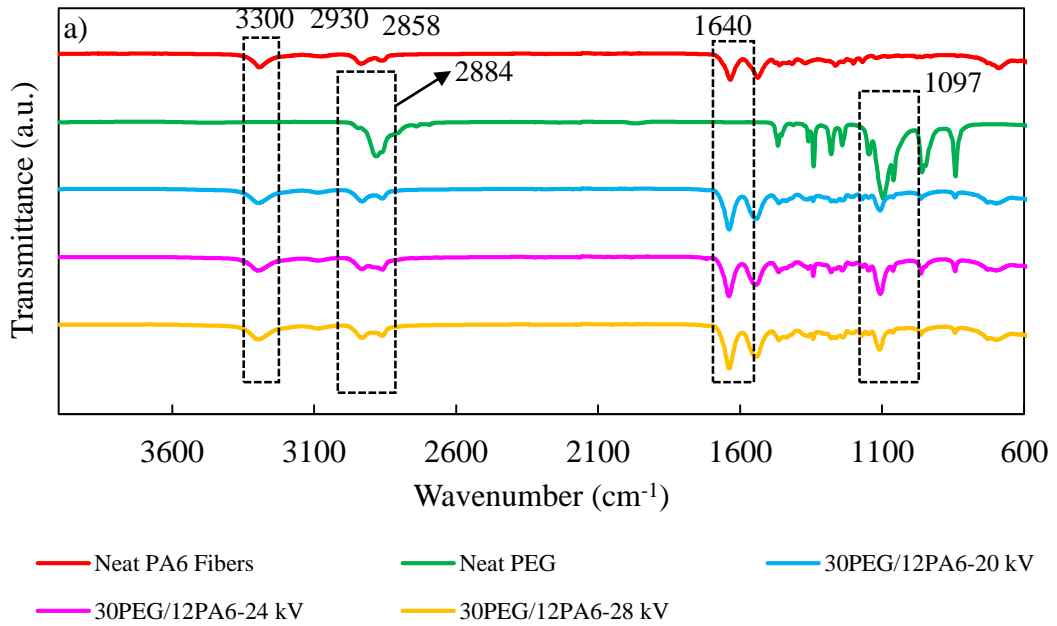


Figure 24. FTIR spectra of electrospun samples produced under 20, 24 and 28 kV of applied electrical potentials (SC: 30 wt. % PEG/12 wt. % PA6, TCD: 10 cm, SFR: 0.1/0.3 ml/h, CT: plate, ED: 30 min).

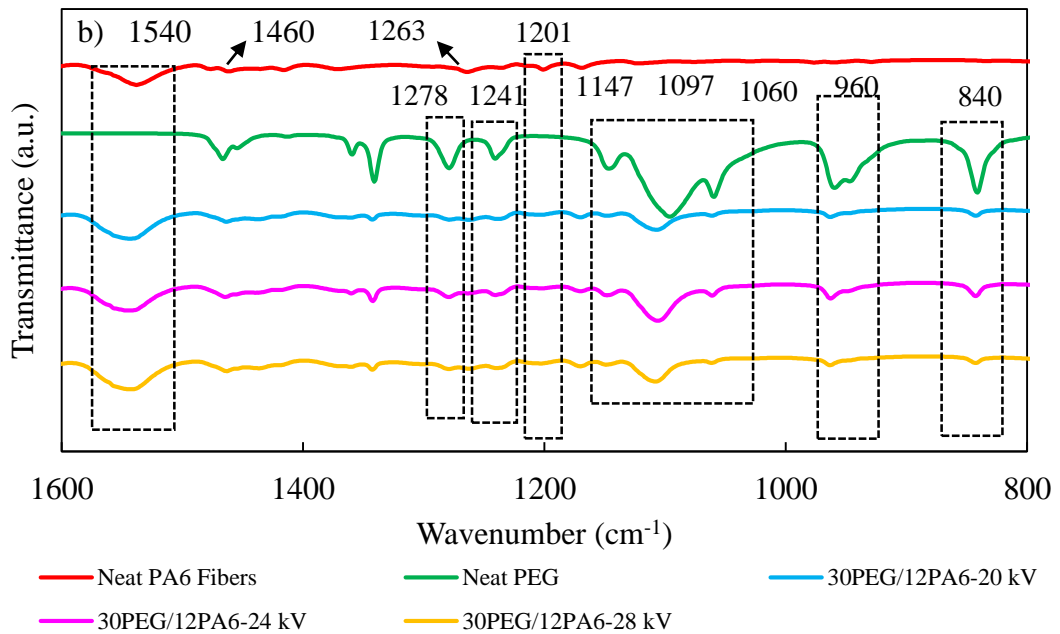


Figure 25. Zoomed FTIR spectra of electrospun samples produced under 20, 24 and 28 kV of applied electrical potentials (SC: 30 wt. % PEG/12 wt. % PA6, TCD: 10 cm, SFR: 0.1/0.3 ml/h, CT: plate, ED: 30 min).

#### **4.1.4. Feed Rate Optimization**

Optimization of the solution feed rates were done by using 30 wt. % PEG as core, 12 wt. % PA6 as shell solution concentration, 24 kV as the applied electrical potential and 10 cm as the tip to collector distance. Electrospinning was conducted for half an hour. The core solution feed rate was increased from 0.1 to 0.2 ml/h, whereas shell solution feed rate was increased from 0.2 to 0.5 ml/h. Different solution feed rate combinations were tried in order to observe the effect of feed rate ratios of core to shell solution on the nanofiber structure.

##### **4.1.4.1. Scanning Electron Microscopy (SEM) Analysis**

SEM micrographs of nanofibers produced by using different core and shell solution flow rates can be seen in Figures 26 and 27. In electrospinning, it is important to feed sufficient amount of solution to the needle tip so that a successful Taylor cone can be formed [41, 71]. Thus, the range of feed rates that could support Taylor cone formation was determined by preliminary experiments. Additionally, other than the total solution feed rate, in coaxial electrospinning, ratio of the shell solution feed rate to the core solution feed rate is more important for ensuring a stable Taylor cone formation and formation of core/shell structure. Thus, different ratios were experimented where shell solution feed rate was 1.5, 2, 3, 3.5, 4 and 5 times greater than the core solution feed rate. Firstly, the core solution feed rate was fixed at 0.1 ml/h and the shell solution feed rate was increased in a manner of 0.2, 0.3, 0.35, 0.4 and 0.5 ml/h. The SEM micrographs of nanofibers produced by these increasing shell solution feed rates can be seen in Figure 26. Secondly, the shell solution feed rate was fixed at 0.3 ml/h and the core solution feed rate was adjusted as 0.15 and 0.2 ml/h. The SEM micrographs of the respective nanofibers can be seen in Figure 27. Bar chart depicting the average fiber diameter of nanofibrous samples electrospun with different solution feed rates is given in Figure 28. Frequency distribution graph depicting the uniformity of the fiber diameters is given in Figure B.3 in Appendix B.

Analyses of the SEM micrographs reveal that there are both minimum and maximum values of shell to core solution feed rate ratios for more stable coaxial electrospinning processes. When the ratio was lower than the optimum value by which successful and uniform core/shell fibers can be formed, since PEG amount in the needle tip increased with respect to PA6, the Taylor cone became highly unstable resulting in higher standard deviations in average fiber diameter measurements [66]. A non-uniform nanofiber structure formed due to the excess PEG amount in the needle tip during the process. Since PEG could not form fibrous structure, excessive feeding caused instability in the process. On the other hand, when the shell solution feed rate was excessively higher than the core solution feed rate, the Taylor cone formed mainly from the shell polymer or blends rather than core/shell structured nanofibers resulting in thinner nanofibers [66]. These fibers are comprised of mainly shell polymer as can be seen in the case of 0.1 ml/h to 0.5 ml/h core/shell solution feed rate ratios. The reduced average fiber diameter value and the highly smooth fiber structures in Figure 26 (e) reveal that the morphology comprised of mainly PA6 when 0.1/0.5 ml/h feed rate was used in coaxial electrospinning process. For these samples DSC analysis results showed lower PEG melting enthalpy values revealing presence of less PEG in the nanofibrous structure. According to the average fiber diameter measurements, the most uniform nanofiber structure was observed in the case of 0.1 ml/h core solution feed rate and 0.35 ml/h shell solution feed rate. It can be seen that all the average fiber diameter measurements resulted in similar standard deviations revealing that feed rate does not have as significant effect on the uniformity of the fibers as other electrospinning parameters such as solution concentration and applied electrical potential.

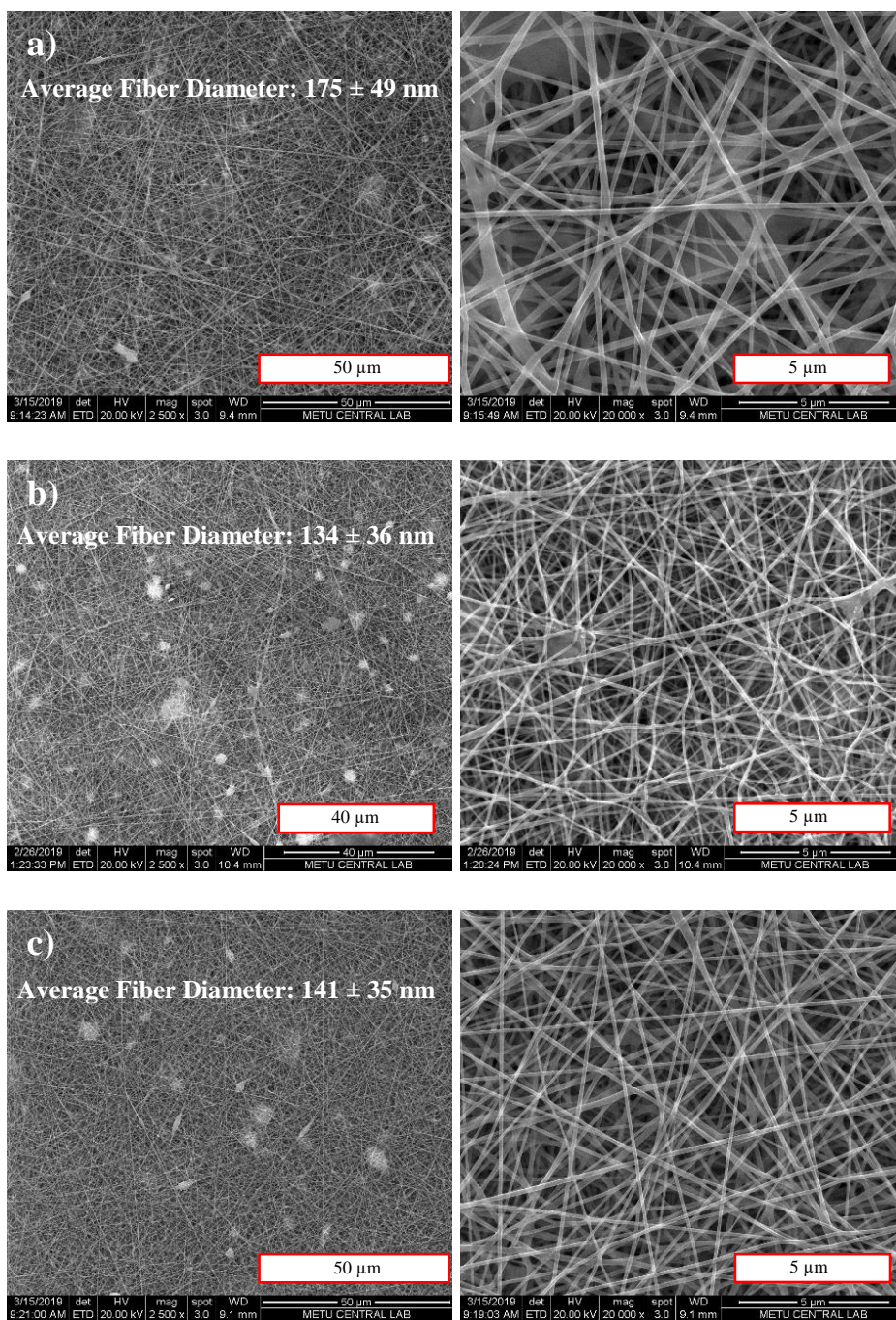


*Figure 26.* SEM micrographs of samples produced with 0.1 ml/h PEG solution feed rate and a) 0.2, b) 0.3, c) 0.35, d) 0.4 and e) 0.5 ml/h PA6 solution feed rates (SC: 30 wt. % PEG/12 wt. % PA6, AEP: 24 kV, TCD: 10 cm, CT: plate, ED: 30 min).

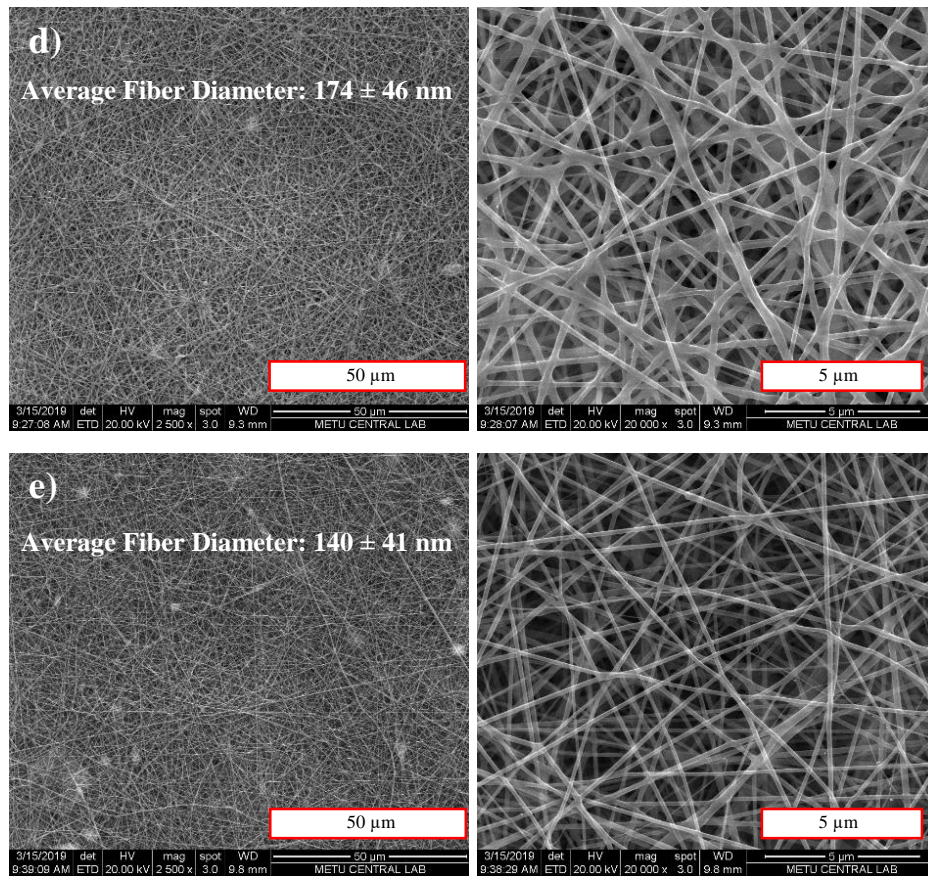


*Figure 26.* (continued) SEM micrographs of samples produced with 0.1 ml/h PEG solution feed rate and a) 0.2, b) 0.3, c) 0.35, d) 0.4 and e) 0.5 ml/h PA6 solution feed rates (SC: 30 wt. % PEG/12 wt. % PA6, AEP: 24 kV, TCD: 10 cm, CT: plate, ED: 30 min).

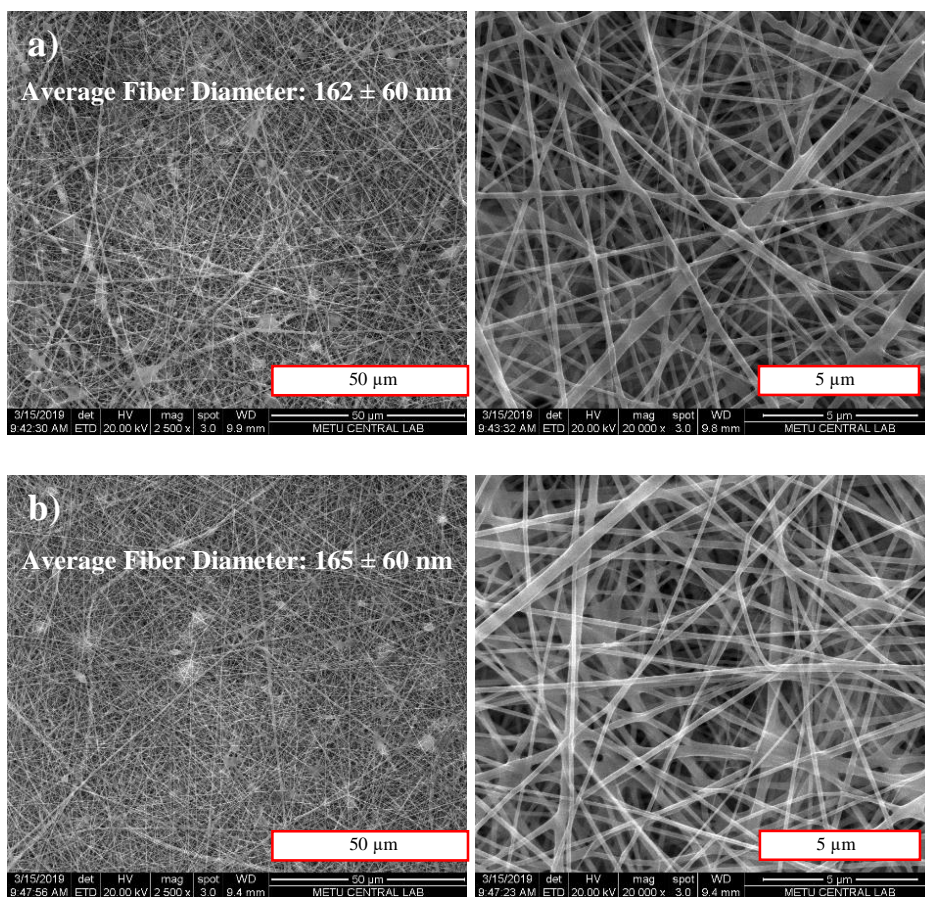


*Figure 27.* SEM micrographs of samples produced with 0.3 ml/h PA6 solution feed rate and a) 0.15 and b) 0.2 ml/h PEG solution feed rates (SC: 30 wt. % PEG/12 wt. % PA6, AEP: 24 kV, TCD: 10 cm, CT: plate, ED: 30 min).

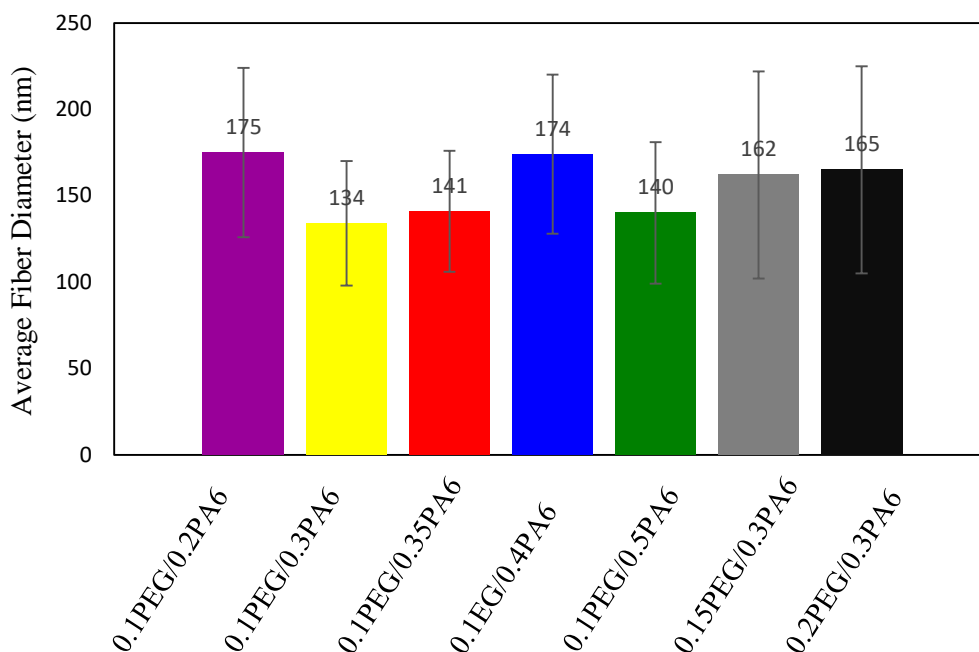


Figure 28. Bar chart depicting the average fiber diameter of nanofibrous samples electrospun using different solution feed rates (SC: 30 wt. % PEG/12 wt. % PA6, AEP: 24 kV, TCD: 10 cm, CT: plate, ED: 30 min).

#### 4.1.4.2. Thermogravimetric Analysis (TGA)

The TGA curves of the samples produced with different solution feed rates are given in Figure 29. The decomposition temperatures of the samples are given in Table 14. According to the results of the thermogravimetric analysis, as the shell solution feed rate increased the decomposition temperature also increased. The increase can be observed between 0.1PEG/0.3PA6 and 0.1PEG/0.5PA6 samples. This is due to the fact that PA6 has higher decomposition temperature with respect to PEG. All the electrospun samples had their decomposition temperature in between the decomposition temperature of PEG and PA6. The fact that all the decomposition curves indicated single mass drop at certain temperatures means successful coaxial electrospinning of PEG and PA6 was achieved.

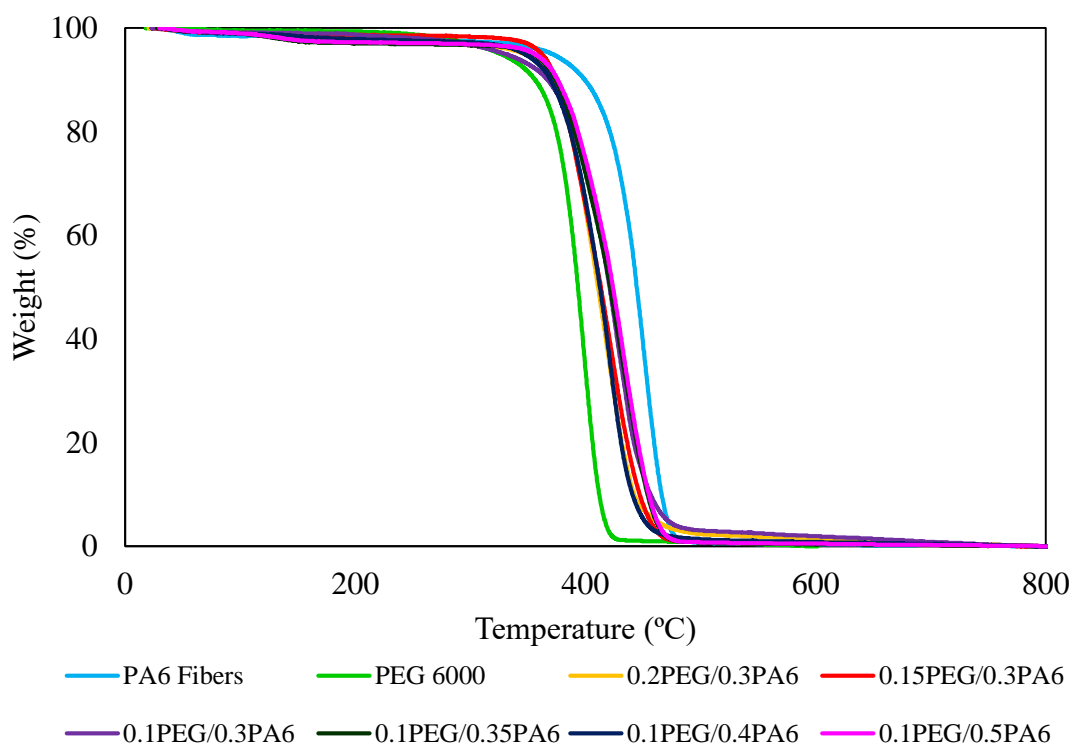


Figure 29. TGA data of nanofibrous samples produced using different core/shell solution feed rates using different solution feed rates (SC: 30 wt. % PEG/12 wt. % PA6, AEP: 24 kV, TCD: 10 cm, CT: plate, ED: 30 min).

Table 14. Decomposition temperatures of nanofibrous samples electrospun using different core/shell solution feed rates (SC: 30 wt. % PEG/12 wt. % PA6, AEP: 24 kV, TCD: 10 cm, CT: plate, ED: 30 min).

Sample	Decomposition Temperature (°C)
Neat PA6 Fibers	453
Neat PEG	400
0.15PEG/0.3PA6	425
0.2PEG/0.3PA6	419
0.1PEG/0.2PA6	420
0.1PEG/0.3PA6	426
0.1PEG/0.35PA6	433
0.1PEG/0.4PA6	430
0.1PEG/0.5PA6	432

#### 4.1.4.3. Differential Scanning Calorimetry (DSC) Analysis

DSC analysis results of the nanofibrous samples electrospun with different core/shell solution feed rates are given in Table 15. Samples that were subjected to DSC analysis were chosen to represent different shell to core solution feed rate ratios from 1.5 to 5. According to the results, the melting temperature of the PEG content in the core/shell nanofibrous samples did not significantly change as the PA6 solution feed rate increased. On the other hand, the melting enthalpy value decreased with increasing shell solution feed rate ratio with respect to core solution feed rate. This is due to the decreasing PEG amount in the nanofibers with higher shell solution feed rate ratio. When the PEG encapsulation efficiency values were considered, the calculations showed similar results except for the 0.1PEG/0.5PA6 sample which showed higher resemblance in melting enthalpy to the theoretical value due to the low amount of PEG in the structure. The encapsulation efficiency was calculated highest for the 0.1PEG/0.5PA6 sample with a value of 87%. This was due to the fact that the theoretical efficiency of enthalpy is calculated by multiplying the melting enthalpy of the neat PEG with its calculated PEG content and since in 0.1PEG/0.5PA6 sample the PEG amount is lower than in the other samples, the experimental value resembles the theoretical value more easily. Since the resulting value in the denominator of the Equation 3.6 is the lowest for this sample, although the experimental value of the melting enthalpy is low with respect to other samples, this does not affect the resulting encapsulation efficiency value significantly. Also, this does not imply a successful production of core/shell nanofibers since the thermal energy storage capacity of the resulting material is dominantly affected by the melting enthalpy of the PCMs encapsulated.

Table 15. DSC data of the samples electrospun using different core/shell solution feed rates (SC: 30 wt. % PEG/12 wt. % PA6, AEP: 24 kV, TCD: 10 cm, CT: plate, ED: 30 min).

Samples	Melting Temperature (°C)			Latent Heat of Melting (J/g)	PEG Encapsulation Efficiency (%)
	Onset	Peak	Endset		
Neat PA6 Fibers	213	222	229	83	-
Neat PEG	58	64	70	210	100
0.15PEG/0.3PA6	50	57	61	80	68
0.2PEG/0.3PA6	52	61	70	105	79
0.1PEG/0.2PA6	51	60	68	78	67
0.1PEG/0.3PA6	51	59	67	76	80
0.1PEG/0.35PA6	50	57	65	68	79
0.1PEG/0.4PA6	50	57	63	61	75
0.1PEG/0.5PA6	49	57	65	61	87

#### 4.1.4.4. Fourier Transform Infrared Spectroscopy (FTIR) Analysis

FTIR spectra of the electrospun samples produced by using different core/shell solution feed rates are given in Figures 30-32. According to the results, it was observed that the characteristic peaks of PEG except at  $2884\text{ cm}^{-1}$  were present in all the samples with only lower intensities. The peaks at  $1097$ ,  $1145$  and  $1341\text{ cm}^{-1}$  all corresponding to  $-\text{CH}_2$  vibration were present in all the spectra. But in samples 0.1PEG/0.2PA6, 0.15PEG/0.3PA6 and 0.2PEG/0.3PA6 as can be seen in Figure 32, intensities of these peaks were higher due to higher core/shell feed rate ratio compared to the other samples. Additionally, FTIR peaks corresponding to  $-\text{CH}_2$  twisting at wavenumbers  $960$ ,  $1241$  and  $1278$  showed increasing intensity with increasing core/shell solution feed rate ratio. Characteristic peaks of PEG at  $840$ ,  $1060$  and  $1466\text{ cm}^{-1}$  belonging to C-O stretching, C-C stretching and  $\text{CH}_2$  scissoring, respectively were also present in all core/shell nanofibrous samples. These peaks can be seen in the zoomed FTIR spectra of the electrospun samples given in Figure 32. Although in all the samples, intensity of the characteristic peak of PEG at  $2884\text{ cm}^{-1}$  corresponding to absorption of C-O bond was decreased, for 0.1PEG/0.35PA6 sample this value was the lowest

indicating successful encapsulation of PEG [11]. On the other hand, peaks belonging to PA6 such as at 3300, 2930  $\text{cm}^{-1}$  representing the  $-\text{NH}$  stretching and  $-\text{CH}_2$  axial deformation also appeared in all the specimens with similar intensities indicating that PA6 was successfully applied as the nanofiber shell material in all samples. These peaks are given in Figure 31.

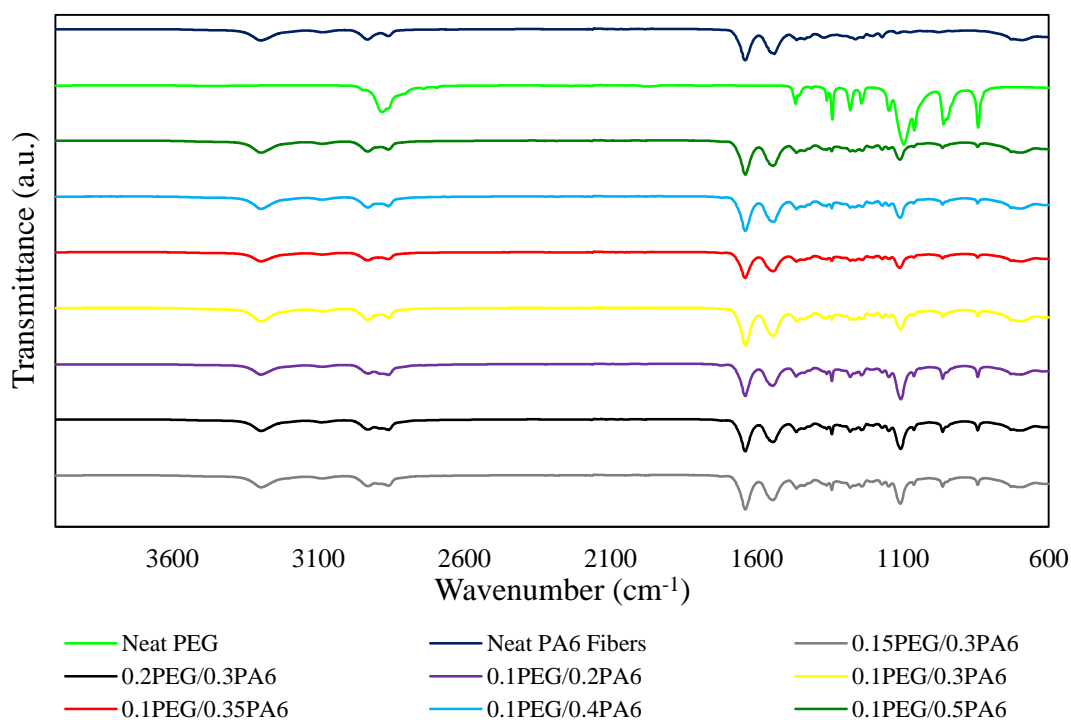


Figure 30. FTIR spectra of nanofibrous samples produced by using different feed rates (SC: 30 wt. % PEG/12 wt. % PA6, AEP: 24 kV, TCD: 10 cm, CT: plate, ED: 30 min).

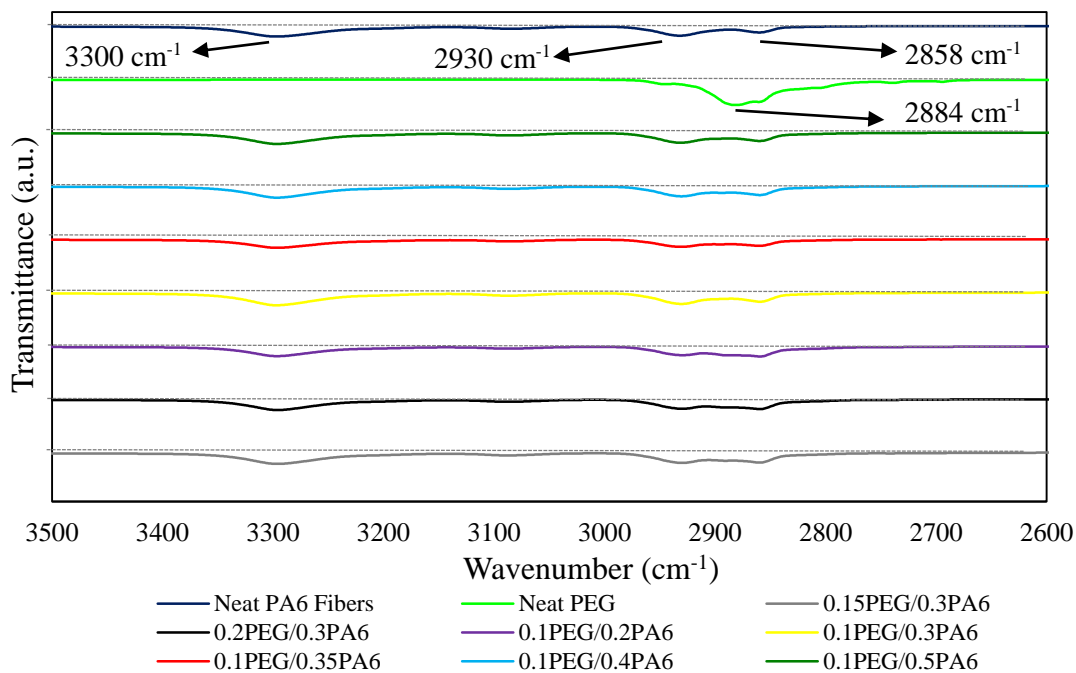


Figure 31. Zoomed FTIR spectra of nanofibrous samples produced by using different feed rates (SC: 30 wt. % PEG/12 wt. % PA6, AEP: 24 kV, TCD: 10 cm, CT: plate, ED: 30 min).

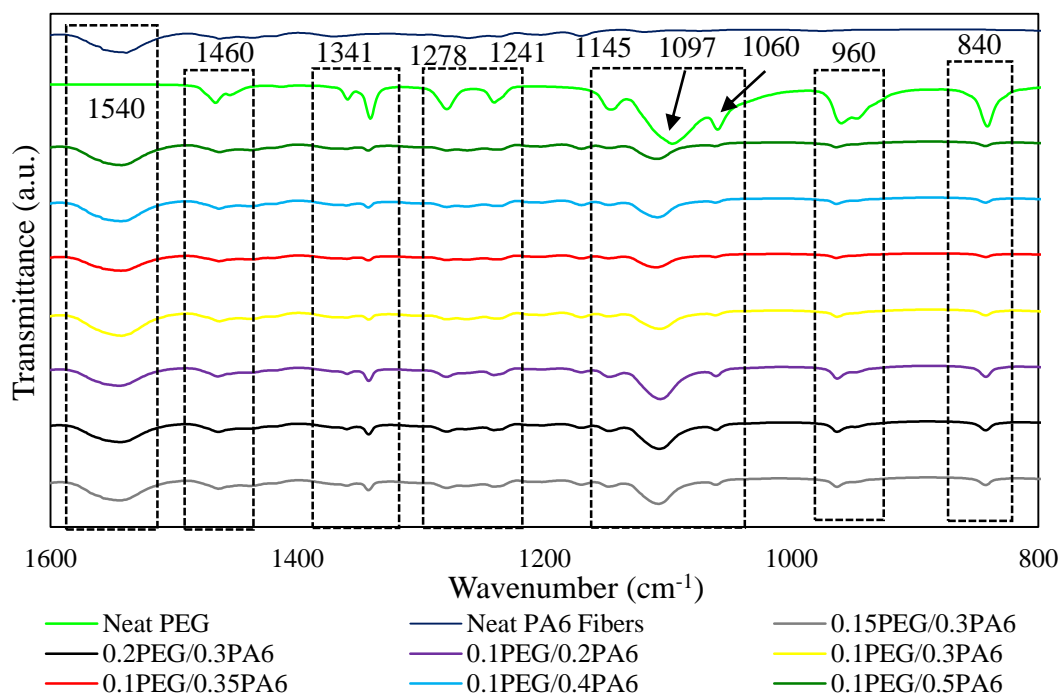


Figure 32. Zoomed FTIR spectra of nanofibrous samples produced by using different feed rates (SC: 30 wt. % PEG/12 wt. % PA6, AEP: 24 kV, TCD: 10 cm, CT plate, ED: 30 min).

## **4.2. Development of Composite Core/Shell Nanofibers**

After optimization of the coaxial electrospinning parameters for obtaining uniform core/shell structured nanofibrous samples, HNTs were introduced into the core solution to develop composite nanofibers and observe the effect of nano additives on the morphology, thermal, mechanical and heat storage properties of the material. HNTs were added to the core solution since utilization of the affinity between PEG and nanotubes was aimed. The affinity between the ether groups in the PEG backbone or the hydroxyl end groups of the PEG molecules and hydroxyl groups on the outer surface of the nanotubes was utilized in enhancing the physical interactions.

Firstly, vacuum dried HNTs were added to the core solution with 0.5, 1, 3 and 5 wt. % concentrations with respect to PEG. Morphology, thermal stability, heat storage property and chemical structure of the nanofibers were investigated by SEM imaging, TGA, DSC and FTIR analysis, respectively. Secondly, HNTs surfaces were activated by piranha etching in order to increase the hydroxyl groups at the surface defects. By this way, further enhancement of the interaction between HNTs and the PEG was aimed. Although PA6 is also a polar polymer due to the amide groups in its structure, the HNTs were only added to the PEG solution and the only interaction of core/shell solutions occur at the needle in an instant where mixing is time limited. Thus, possible interaction between HNTs and PA6 was also kept at minimum, limiting the interaction between the nanoparticles and the PA6.

## **4.3. Characterization of HNTs**

The dried HNTs and piranha etched HNTs were both characterized by XRD, TGA and FTIR given in Figures 33, 34 and 35, respectively. According to the XRD analysis results in Figure 33, both dried and piranha etched HNTs showed diffraction peak at  $12^\circ$  ( $2\theta$ ) in the (001) plane indicating dehydrated halloysite-(7Å) structure having 0.74 nm of interlayer spacing. There was no significant difference between XRD profiles of dried and piranha etched HNTs indicating no alteration in crystal structure of the nanotubes occurred upon surface activation by piranha etching. The XRD peaks in

both specimens were at  $20^\circ$ ,  $24^\circ$ ,  $35^\circ$  and  $38^\circ$  corresponding to d(100), d(002), d(130) and d(131) planes, respectively. Additionally, thermal analysis of the nanotubes was also done by TGA. Results indicated that upon heating up to  $750^\circ\text{C}$ , about 16% weight loss occurred in both specimens. The major weight loss between  $400\text{-}600^\circ\text{C}$  was due to dehydroxylation of the Al-OH groups in the nanotube structures [70]. Upon FTIR analysis, characteristic peaks of HNTs such as at  $3697$ ,  $3622$  and  $912\text{ cm}^{-1}$  were observed corresponding to -OH stretching vibrations of the inner surface Al-OH. Peak at  $1635\text{ cm}^{-1}$  was assigned to deformation vibration of water. Additionally, peaks at  $1114$  and  $1029\text{ cm}^{-1}$  were ascribed to apical Si-O stretching vibration and in-plane Si-O stretching vibrations, respectively. FTIR analysis of the nanotubes revealed that at  $1210\text{ cm}^{-1}$ , a new peak has emerged with piranha etching due to the Si-O-Si asymmetric stretching vibrations. Additionally, increase in the intensity of the peak at  $3450\text{ cm}^{-1}$  was due to the Si-OH vibrations. Moreover, band at  $1114\text{ cm}^{-1}$  almost disappeared, whereas intensities of the peaks at  $1089$  and  $796\text{ cm}^{-1}$  increased due to the appearance of amorphous silica during removal of a part of the alumina by the piranha etching [70]. Since outer surface of the nanotubes are comprised of siloxane groups, upon piranha etching the intensity of the peak at  $1089\text{ cm}^{-1}$  corresponding to in plane Si-O stretching was increased with respect to the peak at  $1114\text{ cm}^{-1}$  which indicates the apical Si-O stretching. This can be considered as a proof towards successful surface activation of the HNTs by piranha solution treatment.

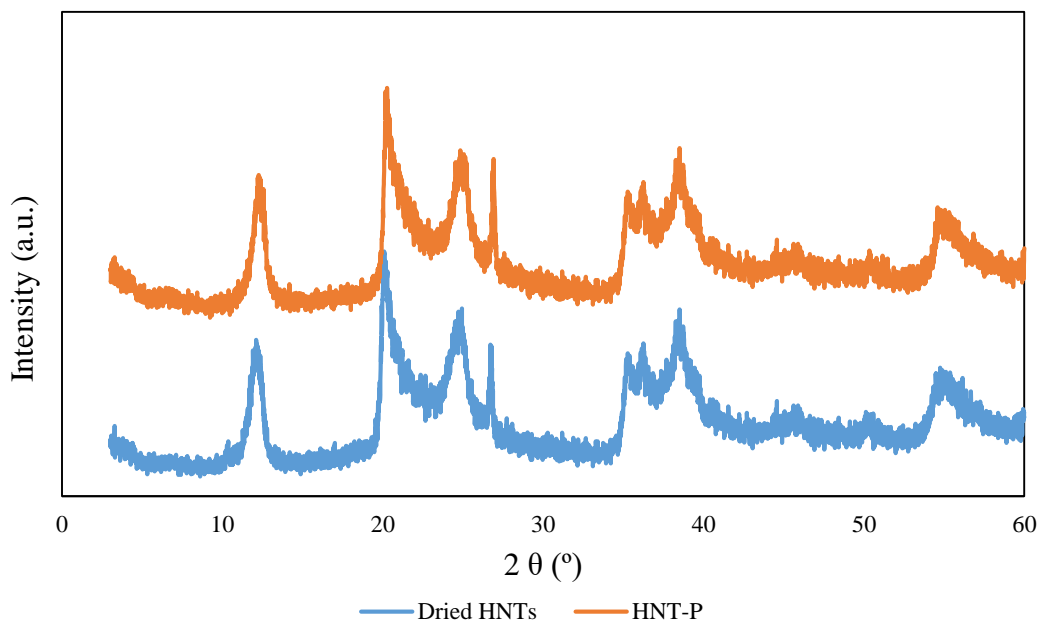


Figure 33. XRD patterns of dried HNTs and piranha etched HNTs (HNT-P).

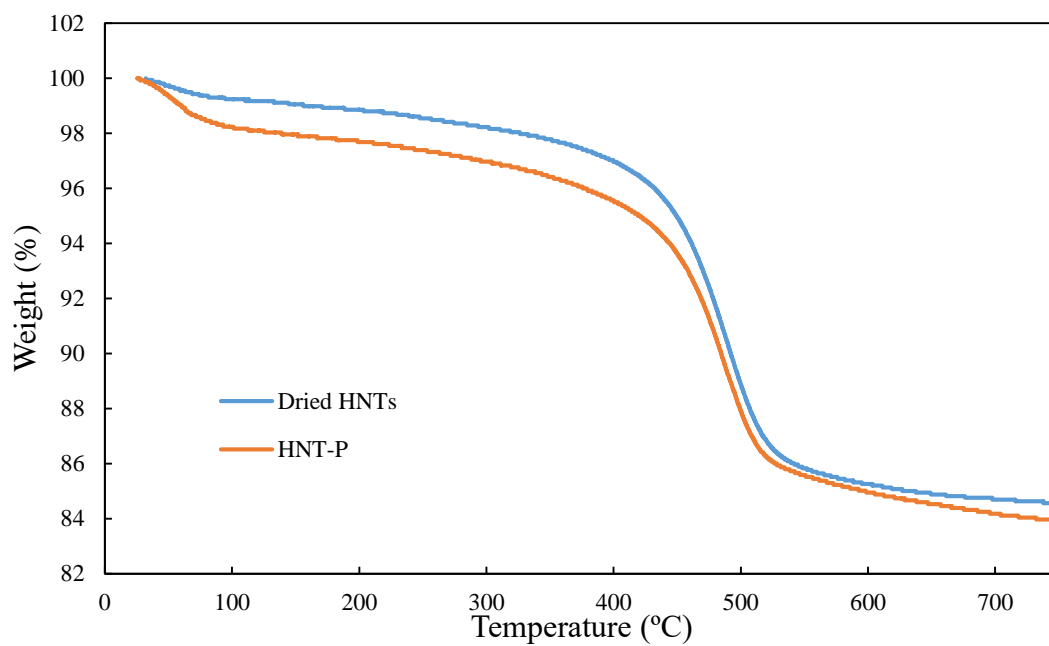


Figure 34. TGA curves of dried HNTs and piranha etched HNTs (HNT-P).

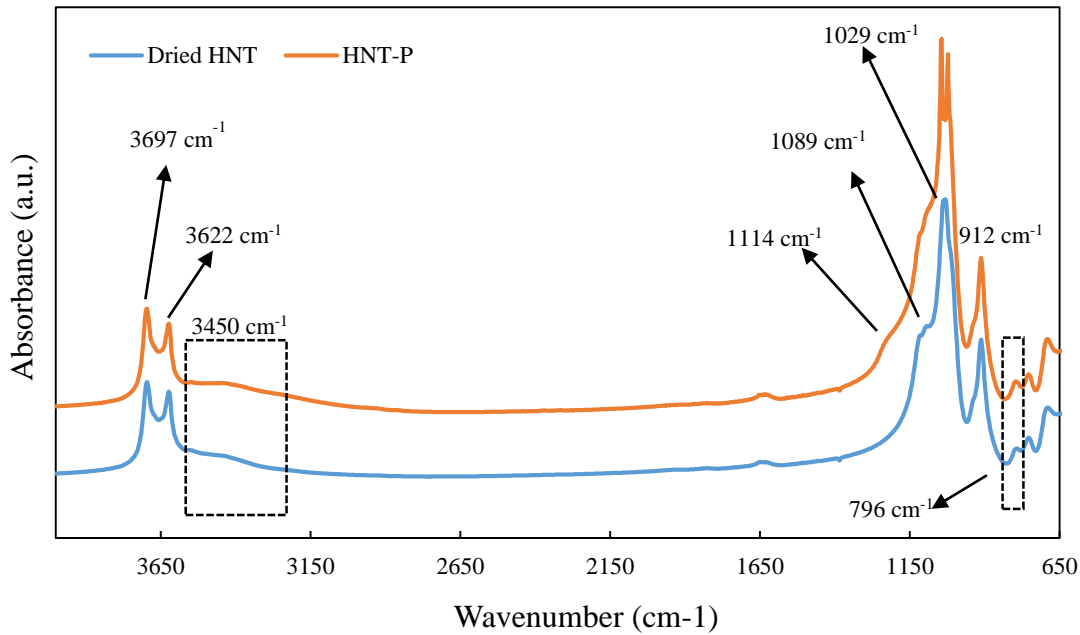
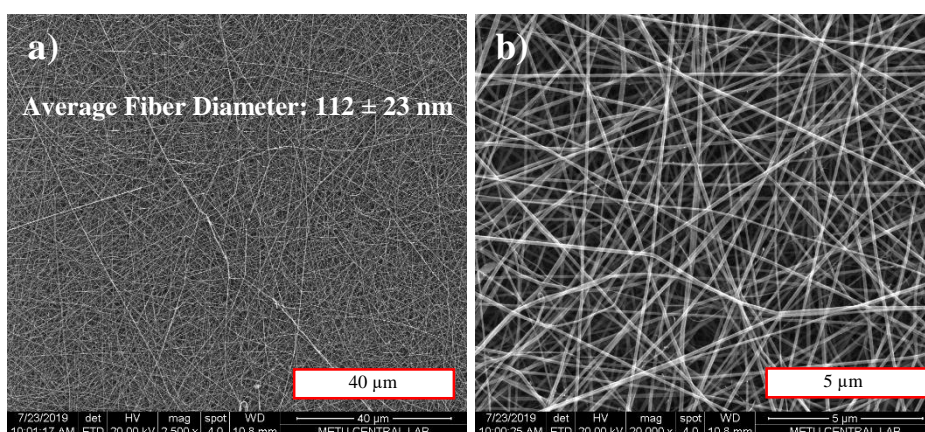


Figure 35. FTIR spectra of dried HNTs and piranha etched HNTs (HNT-P).

#### 4.3.1. Scanning Electron Microscopy (SEM) Analysis

Scanning electron microscopy was initially performed on neat PA6 nanofibrous sample produced by using uniaxial electrospinning. Except for the solution feed rate, previously optimized process and solution parameters were used during electrospinning of neat PA6. Since, uniaxial needle was used rather than coaxial, the PA6 solution feed rate was adjusted accordingly. The diameter of the outer needle of the coaxial spinneret was 1.6 mm with another spinneret having 0.8 mm diameter placed concentrically. On the other hand, the diameter of the uniaxial spinneret was 0.8 mm. Thus, a flux analysis was done in order to acquire the same amount of solution feeding per area per unit time. As a result, feed rate of the PA6 solution through the uniaxial spinneret was determined to be 0.2 ml/h. The resulting morphology can be seen in Figure 36. According to the SEM images, very fine and uniform nanofibers were observed having 112 nm of average fiber diameter and standard deviation of  $\pm 23$  nm. By this experiment, it was seen that stable uniaxial electrospinning of PA6 could be performed with the optimized process and solution parameters.

In order to confirm the core/shell structured nanofiber morphology, SEM imaging was also performed on the coaxially electrospun PEG/PA6 nanofibers with the previously optimized parameters. The only exception was the electrospinning duration. Since the composite core/shell nanofibrous samples were to be subjected to tensile testing, the sample thickness had to be adjusted accordingly. Hence, electrospinning of the composite samples was done for two hours onto cylindrical collector with rotational speed of 100 rpm. All the samples including neat PA6 fibers, neat core/shell and composite nanofibers were produced by using the same electrospinning process parameters. The resulting neat core/shell nanofiber morphology can be seen in Figure 37. It can be said both from the SEM image and the average fiber diameter measurements that with incorporation of PEG solution, the resulting fibers became thicker. This is due to the increase in the amount of polymer fed to the needle tip in unit time during the electrospinning process with the introduction of PEG solution [10]. The average fiber diameter of the neat core/shell fibers was measured to be 173 nm with a standard deviation of 60 nm. Decrease in uniformity of the fibers was due to the instability introduced to the system with utilization PEG as the core material. It was known from the preliminary experiments that regardless of the polymer concentration, PEG solution could not form nanofibers during electrospinning. This was due to the insufficient molecular entanglements in the solution that could not preserve a fiber morphology during spinning from needle tip to the collector. Although this problem was meant to be solved by utilization of PA6 in the shell solution, 100% encapsulation of the PEG in the core of the fibers could not be achieved. FTIR analysis results in Figures 31 and 32 indicated that a portion of PEG resided on the surface of the nanofibers which was a proof towards nonexistence of full encapsulation. Additionally, according to the thermal cyclic test results 100% of the melting enthalpy of PEG could not be preserved over several melting-freezing cycles indicating phase change material residual on the nanofiber surfaces. The fibers with deformed structures in Figure 37 (b) can be shown as indicators of PEG residing on the surface of the nanofibers. This phenomenon can also be shown as a reason of the decreased uniformity in fiber diameter with respect to neat PA6 nanofibers.



*Figure 36.* SEM micrographs of neat PA6 fibers with a) 2500x and b) 20000x magnifications (SC: 12 wt. % PA6, AEP: 24 kV, TCD: 10 cm, SFR: 0.1/0.35 ml/h, CT: cylinder, RS: 100 rpm, ED: 2 h).

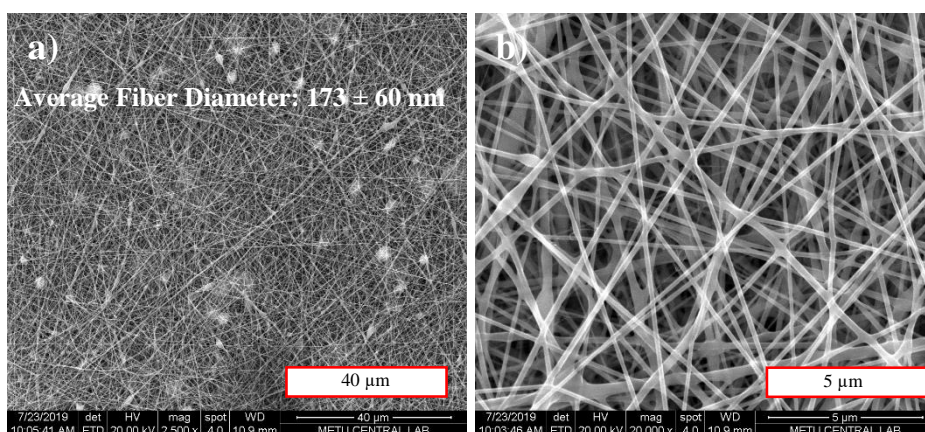


*Figure 37.* SEM micrographs of neat PEG/PA6 coreshell nanofibers with a) 2500x and b) 20000x magnifications (SC: 30 wt. % PEG/12 wt. % PA6, AEP: 24 kV, TCD: 10 cm, SFR: 0.1/0.35 ml/h, CT: cylinder, RS: 100 rpm, ED: 2 h).

In order to observe the effect of nanotube addition to the nanofibers on morphology, firstly, SEM imaging was conducted on the samples in which vacuum dried HNTs were added into the core solution with 0.5, 1, 3 and 5 wt. % concentrations with respect to PEG amount. The SEM images of core/shell nanofibers with 0.5, 1, 3 and 5 wt. % HNTs can be seen in Figures 38, 39, 40 and 41, respectively. In Figure 38, it can be seen that the average fiber diameter was 160 nm with a standard deviation of  $\pm 52$  nm. Also in Figure 38 (b) both thick and very fine nanofibers can be seen contributing to

the non-uniformity of the fiber diameters. In Figure 39 (a), it can be seen that the average fiber diameter was 151 nm with  $\pm 44$  nm of standard deviation. The HNTs in the nanofibers is visible in Figures 38, 39 and 40 (c) proving the nanotubes presence in the samples. Additionally, in Figure 39 (c) the morphology resulting from agglomeration of the HNTs particles can be seen since the fiber structure was disrupted at such points.

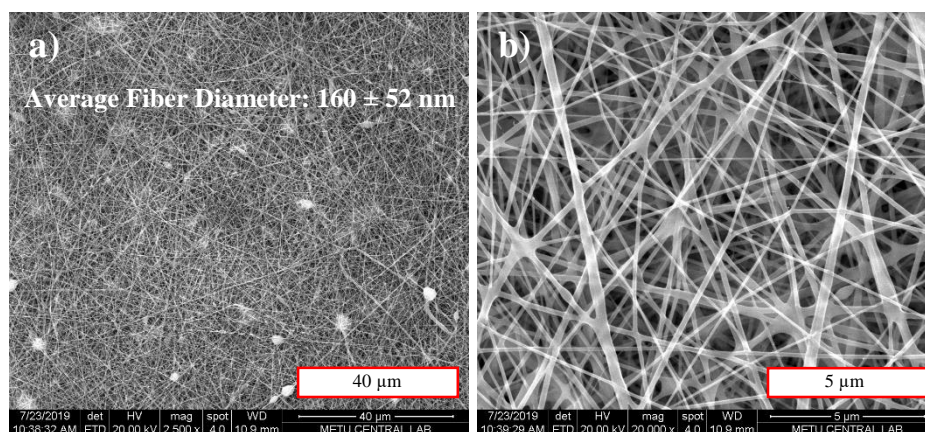


Figure 38. SEM micrographs with magnifications a) 2500x, b) 20000x and c) 50000x of composite nanofibers containing 0.5 wt. % HNT (SC: 30 wt. % PEG/12 wt. % PA6, AEP: 24 kV, TCD: 10 cm, SFR: 0.1/0.35 ml/h, CT: cylinder, RS: 100 rpm, ED: 2 h).

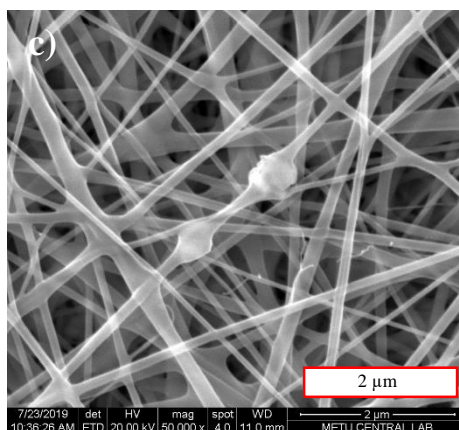


Figure 38. (continued) SEM micrographs with magnifications a) 2500x, b) 20000x and c) 50000x of composite nanofibers containing 0.5 wt. % HNT (SC: 30 wt. % PEG/12 wt. % PA6, AEP: 24 kV, TCD: 10 cm, SFR: 0.1/0.35 ml/h, CT: cylinder, RS: 100 rpm, ED: 2 h).

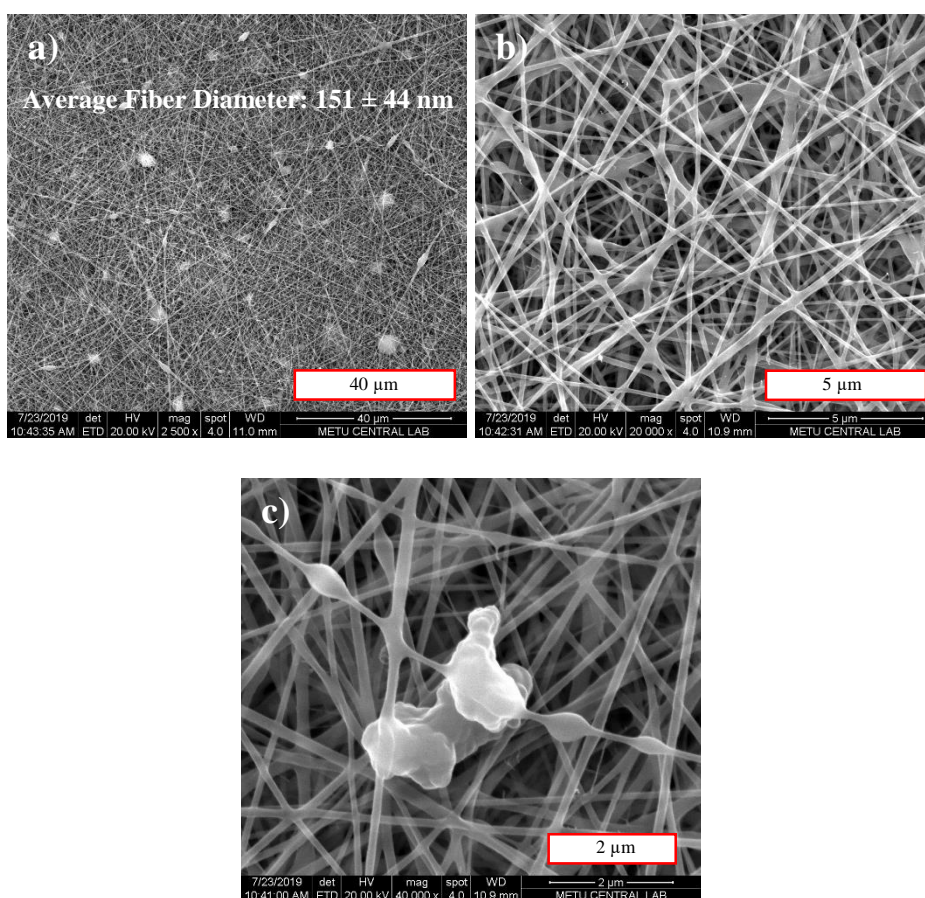
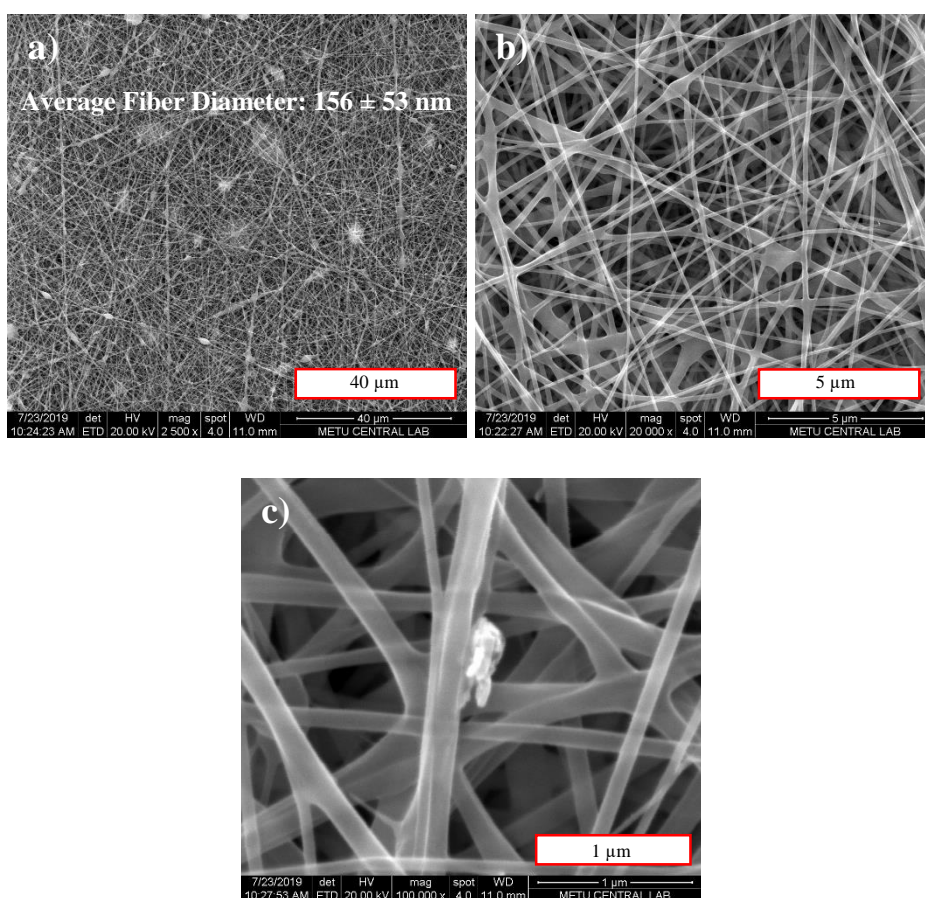


Figure 39. SEM micrographs with magnifications a) 2500x, b) 20000x and c) 40000x of composite nanofibers containing 1 wt. % HNT (SC: 30 wt. % PEG/12 wt. % PA6, AEP: 24 kV, TCD: 10 cm, SFR: 0.1/0.35 ml/h, CT: cylinder, RS: 100 rpm, ED: 2 h).

When the HNTs concentration in the core solution was increased up to 3.0 wt. %, the average fiber diameter did not significantly change with respect to 0.5 and 1 wt. % HNTs added nanofibrous samples. On the other hand, a significant increase in average fiber diameter can be observed with 3 wt. % HNTs addition when compared to neat core/shell fibers. The resulting nanofibers had average diameters of 156 nm and standard deviation of  $\pm 53$  nm. From Figure 40 (c) it can be seen that protrusion of nanotubes from the fiber structure was present at such high additive concentrations. This was due to the weaker interactions between HNTs and PEG matrix when compared to PA6 matrix. At 5 wt. % HNTs concentration, the average fiber diameter further decreased to 149 nm with standard deviation of  $\pm 58$  nm. The resulting morphology is given in Figure 41. Although the average fiber diameter was decreased

with increasing HNTs addition, it can be seen from the diameter measurement results that the standard deviation increased, this can be again attributed to the formation of significantly thick/fine nanofibers concurrently due to the agglomeration and protrusion of the HNTs [71]. The protrusion of the HNTs from the nanofiber structure along with the PEG resulted in thin nanofibers whereas agglomeration of HNTs inside the fibers caused thick nanofibers. When the morphologies and the average fiber diameter values of the HNTs added nanofibers were considered, it was seen that increase in the HNTs concentration in the core solution resulted in effusion of the nanotubes from the core structure to the outer surfaces of the fibers. This was the main reason behind the resulting smooth and fine fibers with lower average fiber diameter value in 5 wt. % HNTs added nanofibrous sample.

The effect of HNTs protruded from the nanofiber structure can also be seen in Figure 41 (b) as thin nanofiber formations occurred due to the lack of nanotubes in the fiber core. Additionally, in Figure 41 (c), it can also be seen that the HNTs were not fully in the fiber structure but rather scattered on the surface. This was due to the excess amount of HNTs in the system and effusion of the HNTs containing PEG material from the fiber structure. Finally, in Figure 41 (d) fracture of the nanofiber shell structure is present revealing the core material which can be shown as a proof of the core/shell system. The presence of a darker region at the point of fiber crack and preservation of fiber's structural integrity despite the crack of the shell material can be acknowledged as a proof of the existence of the core/shell structure.



*Figure 40.* SEM micrographs with magnifications a) 2500x, b) 20000x and c) 100000x of composite nanofibers containing 3 wt. % HNT (SC: 30 wt. % PEG/12 wt. % PA6, AEP: 24 kV, TCD: 10 cm, SFR: 0.1/0.35 ml/h, CT: cylinder, RS: 100 rpm, ED: 2 h).

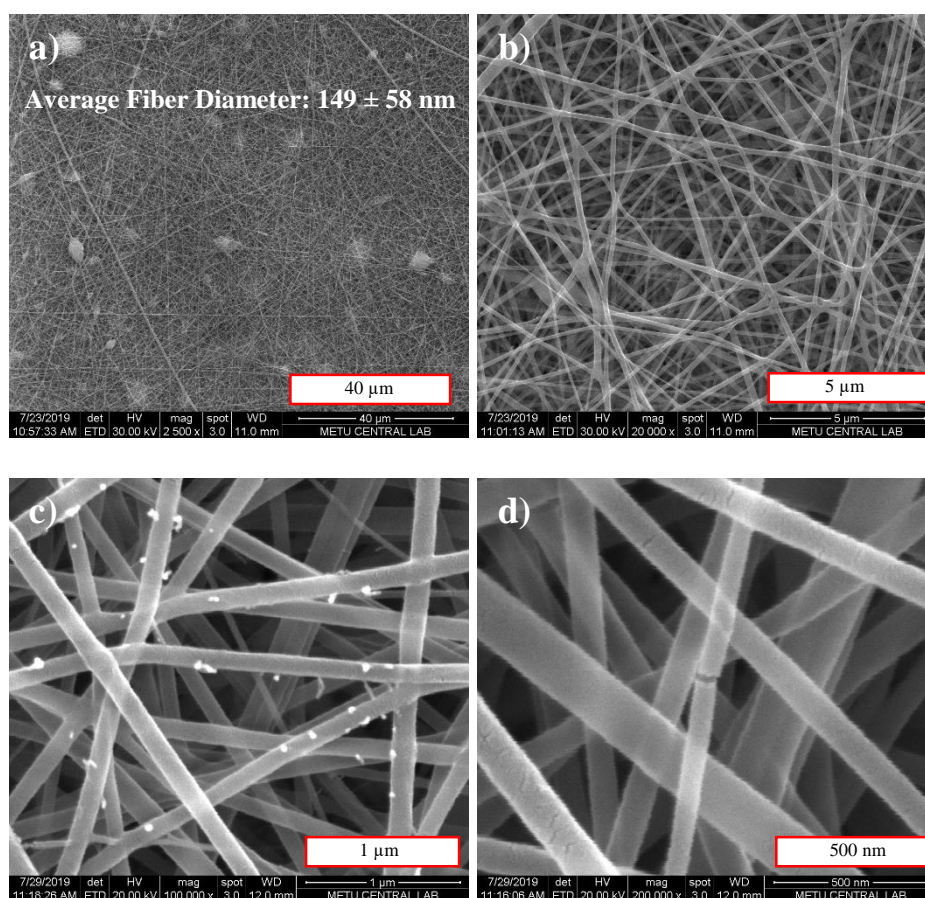


Figure 41. SEM micrographs with magnifications a) 2500x, b) 20000x and c) 200000x of composite nanofibers containing 5 wt. % HNT (SC: 30 wt. % PEG/12 wt. % PA6, AEP: 24 kV, TCD: 10 cm, SFR: 0.1/0.35 ml/h, CT: cylinder, RS: 100 rpm, ED: 2 h).

When the morphologies of the composite nanofibers were analyzed, the main problem resulting in non-uniform nanofibers was determined to be the effusion of the HNTs from the nanofiber core structures. It has been known that HNTs have good affinity towards polar polymers [71]. Although PEG is known to be a polar polymer, the HNTs particles rather preferred each other and formed agglomerates or diffused into the PA6 matrix, eventually effusing entirely from the fiber when they were directly introduced to the solution. As a result of the literature survey, it was figured out that the most convenient way of increasing the affinity of the HNTs towards PEG was to increase the hydroxyl groups at the surface defects of the nanotube structured HNTs [73, 56]. For this purpose, piranha solution was utilized in etching the HNTs. The piranha

etched nanotubes (HNT-P) were added to the core solution with concentrations of 0.5, 1.0, 3.0 and 5.0 wt. % with respect to PEG. The corresponding SEM images of these samples can be seen in Figures 42, 43, 44 and 45.

The morphology of the composite sample containing 0.5 wt. % HNT-P can be seen in the SEM images in Figure 42. It was observed that with introduction of HNT-P, the average fiber diameter was significantly increased with respect to neat core/shell and HNTs added nanofibers. This was due to the better dispersion of the additive in the solution resulting in increased solution viscosity [72]. As the viscosity of the solution increased, less stretching was induced on the electrospinning solution forming thicker nanofibers [72]. When 0.5 wt. % HNT-P was added to the core solution, the resulting nanofibers had average fiber diameter of 196 nm with standard deviation of  $\pm 69$  nm. The SEM images depicting both the morphologies and the average fiber diameter measurement results of the 1 and 3 wt. % HNT-P containing samples are given in Figures 43 and 44, respectively. It was seen that the increasing HNT-P concentration in the core solution resulted in decreasing fiber diameter. This was due to the increasing agglomeration tendency of the HNT-P with increasing concentration. With 1 wt. %, and 3 wt. % HNT-P introduction to the system, the average fiber diameters were 181 and 165 nm, respectively. Also, presence of HNT-P agglomerates residing in the nanofiber structure can be observed in Figures 43 and 44 (c). In Figure 45, the SEM images of the sample containing 5 wt. % HNT-P can be seen. With 5 wt. % HNT-P addition, the resulting average nanofiber diameter was measured to be 161 nm with standard deviation of 50 nm. In Figure 45 (c) and (d), it can be clearly seen that HNT-P agglomerates formed at high concentrations, but the HNT-Ps were fully encapsulated in the polymeric nanofiber. These results indicated that activation of the nanotube surfaces with piranha etching increased the affinity of nanotubes towards both the PEG matrix and other HNTs particles. When the SEM images of the HNTs and HNT-P added composite nanofibers were compared, it was seen that the nanotubes were encapsulated in the fiber cores more successfully when surface activation was performed. On the other hand, due to the increased interaction between the HNTs

particles, agglomerations of the nanotubes were also present. This resulted in higher average fiber diameters with respect to neat and HNTs added core/shell nanofibrous sample. Although agglomerations of HNTs were also present in HNT-P added samples, no protrusion of the particles resulting in thinner nanofibers occurred in HNT-P added samples. This was because of the increased affinity of HNT-P towards PEG upon surface activation.

The average fiber diameters of all the samples both containing HNTs and HNT-P are given in the form of bar chart in Figure 46. The frequency distribution graph of the fiber diameter measurements of the composite nanofibrous samples is given in Figure B.4 in Appendix B. Diameter measurements indicated that although the composite fibers became slightly thicker with respect to the neat PA6 fibers, there was no apparent difference among the average diameters of the composite fibrous samples. When the composite nanofibrous samples with similar additive concentrations were further compared, it was seen that the average fiber diameters slightly increased when HNTs surfaces were piranha etched. The most uniform and smooth fibers were observed to be present in the case of 3 wt. % HNT-P added nanofibrous sample. In Figures 44, 45 and 46 it can be seen that the standard deviation in fiber diameters was lower for the 3 wt. % HNT-P and 5 wt. % HNT-P composite samples with less rough surfaces since less nanotube agglomerations were present due to the possibility of better alignment of nanotubes. The fact that the HNT-P particles are better preserved in the nanofibers enhances the interaction potential of HNTs with PEG in these samples.

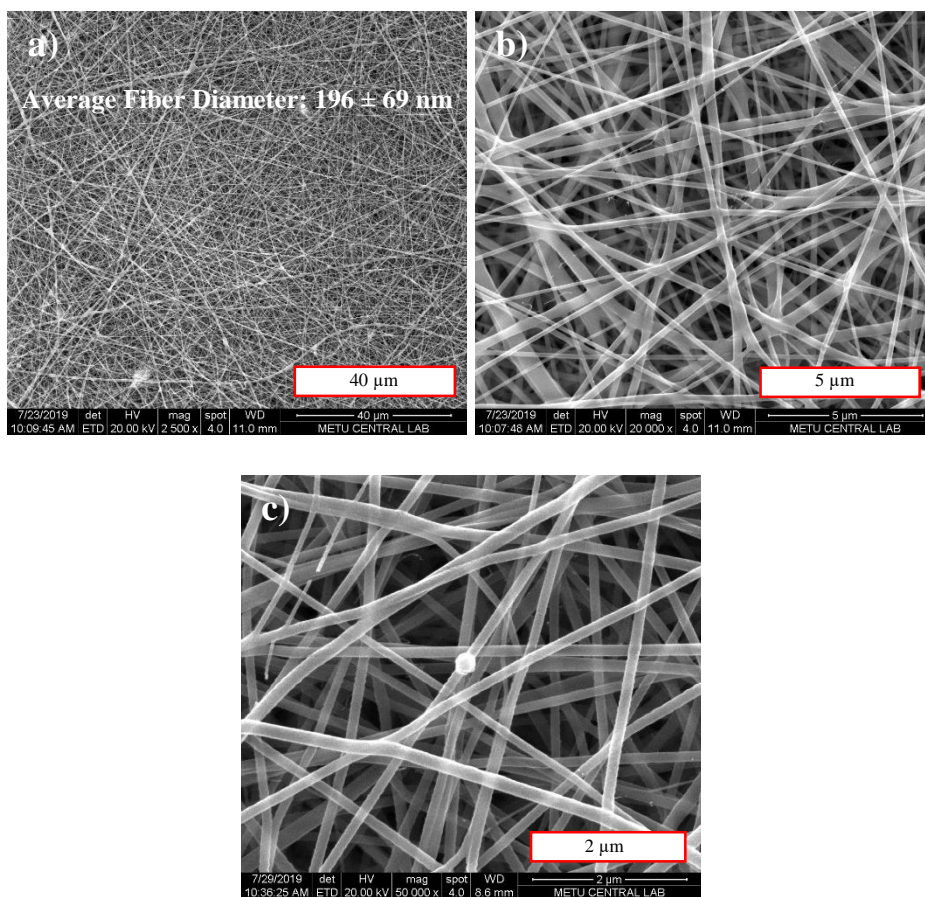
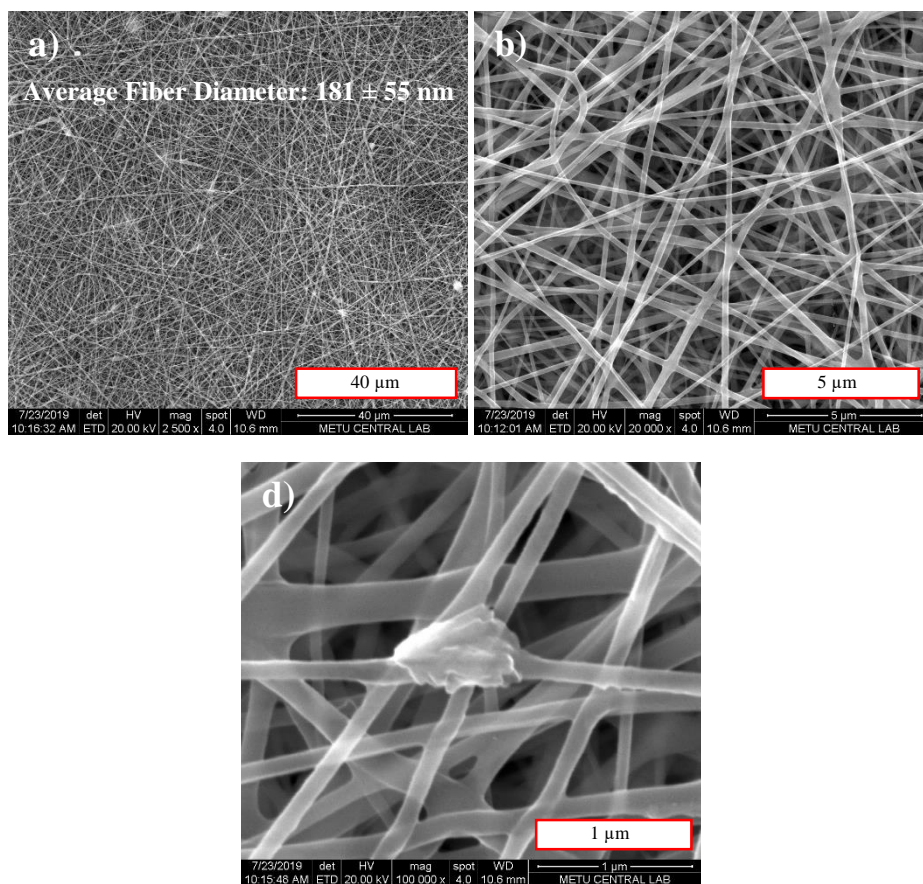
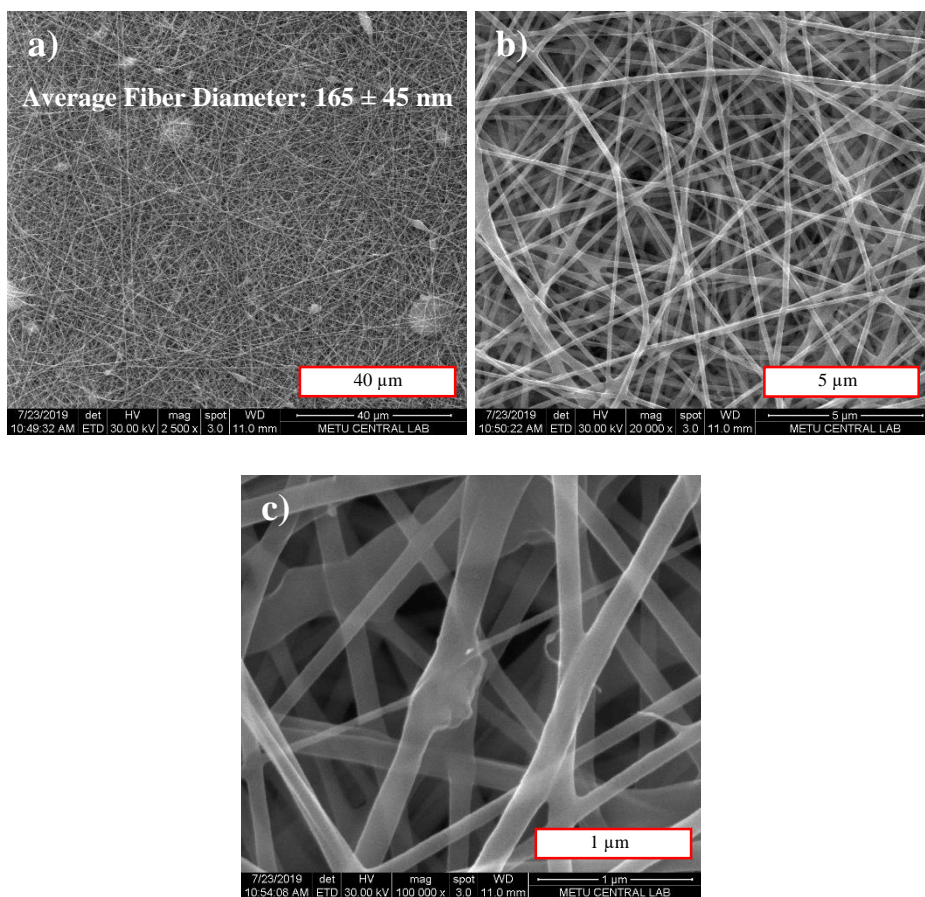


Figure 42. SEM micrographs with magnifications a) 2500x, b) 20000x and c) 50000x of composite nanofibers containing 0.5 wt. % HNT-P (SC: 30 wt. % PEG/12 wt. % PA6, AEP: 24 kV, TCD: 10 cm, SFR: 0.1/0.35 ml/h, CT: cylinder, RS: 100 rpm, ED: 2 h).



*Figure 43.* SEM micrographs with magnifications a) 2500x, b) 20000x and c) 100000x of composite nanofibers containing 1 wt. % HNT-P (SC: 30 wt. % PEG/12 wt. % PA6, AEP: 24 kV, TCD: 10 cm, SFR: 0.1/0.35 ml/h, CT: cylinder, RS: 100 rpm, ED: 2 h).



*Figure 44.* SEM micrographs with magnifications a) 2500x, b) 20000x and c) 100000x of composite nanofibers containing 3 wt. % HNT-P (SC: 30 wt. % PEG/12 wt. % PA6, AEP: 24 kV, TCD: 10 cm, SFR: 0.1/0.35 ml/h, CT: cylinder, RS: 100 rpm, ED: 2 h).

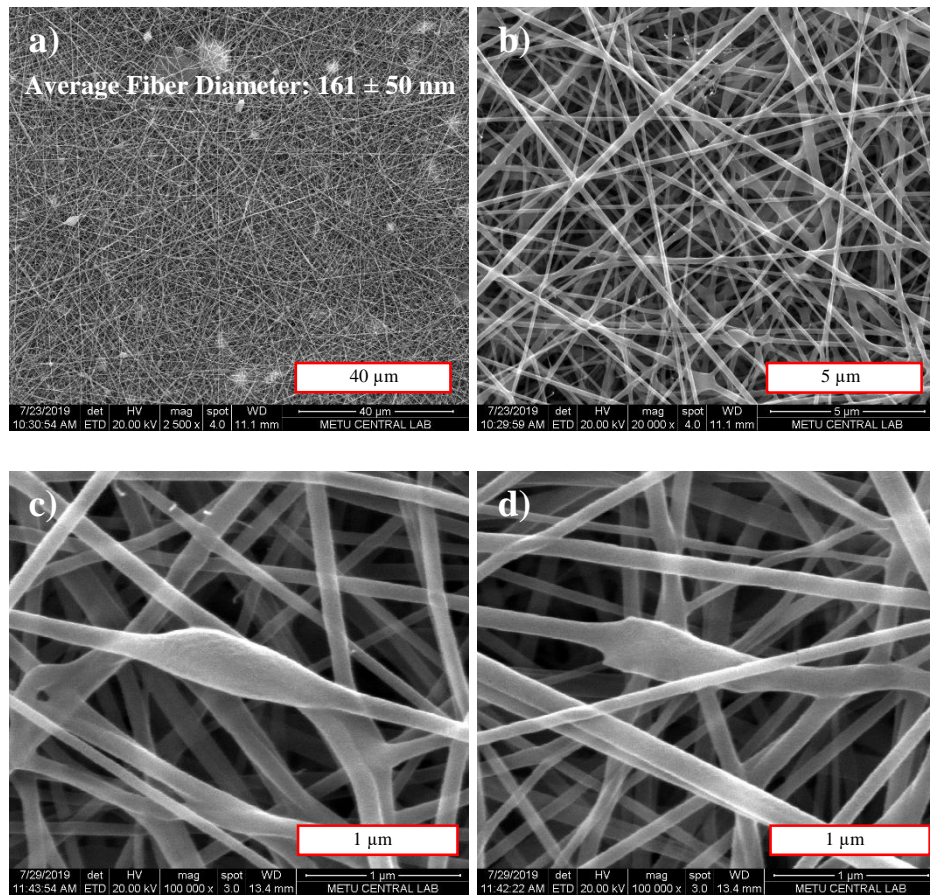


*Figure 45.* SEM micrographs with magnifications a) 2500x, b) 20000x and c-d) 100000x of composite nanofibers containing 5 wt. % HNT-P (SC: 30 wt. % PEG/12 wt. % PA6, AEP: 24 kV, TCD: 10 cm, SFR: 0.1/0.35 ml/h, CT: cylinder, RS: 100 rpm, ED: 2 h).

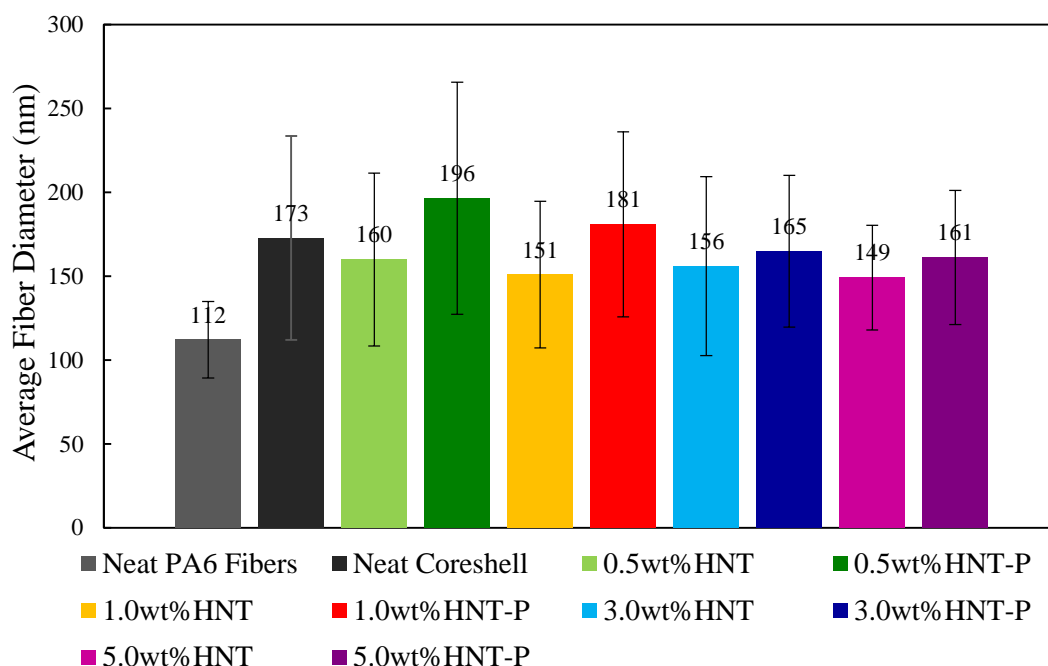


Figure 46. Bar chart depicting the average fiber diameter values of HNT and HNT-P added composite nanofibrous samples (SC: 30 wt. % PEG/12 wt. % PA6, AEP: 24 kV, TCD: 10 cm, SFR: 0.1/0.35 ml/h, CT: cylinder, RS: 100 rpm, ED: 2 h).

#### 4.3.2. Thermogravimetric Analysis (TGA)

In order to observe the effect of HNTs addition on the thermal stability of the nanofibers, thermogravimetric analysis was conducted on both neat and composite samples. TGA curves depicting the temperature versus weight percent data of the neat materials, HNTs and HNT-P added composite nanofibrous samples are given in Figures 47 and 48. Also, the decomposition temperatures of the neat PA6 fibers, neat core/shell structured fibers, HNTs and HNT-P added composite samples can be seen in Table 16. According to the analysis results, it can be said that a single weight loss was observed for all samples. This was due to the effective encapsulation PEG by PA6 shell in the nanofiber morphology. From Figures 47, 48 and Table 16 it can be observed that the neat PA6 fibers had the highest degradation temperature whereas neat PEG had the lowest degradation temperature. With construction of the core/shell structured nanofibers, the decomposition temperature of the sample became between

the two extremes. With introduction of the HNTs, the decomposition temperature of the samples was increased about 7-8°C. This was due to the high thermal stability characteristic of the HNTs residing in the core structure of the nanofibers. The TGA graph of the HNTs and HNT-P are given in Figure 34 indicating only 16% mass loss was present when nanotubes were heated up to 750°C. With activated nanotubes (HNT-P) addition to the core structure, the thermal stability was also increased about 5-11°C. HNT-P had no additional effect on the degradation temperature of the composite nanofibrous samples on top of HNTs itself. On the other hand, when 5 wt. % HNT-P was added to the structure the degradation temperature was the highest. This was due to the less amount of PEG being encapsulated in the nanofibrous structure due to the very high core solution viscosity with 5 wt. % HNT-P addition.

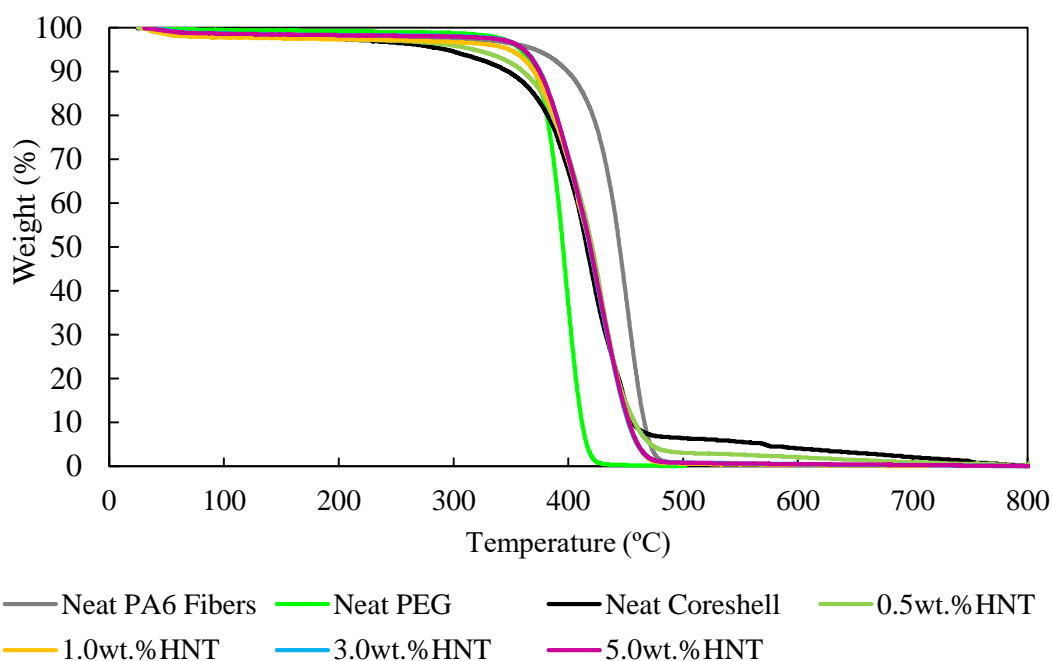


Figure 47. TGA curves of electrospun samples containing different amounts of HNTs (SC: 30 wt. % PEG/12 wt. % PA6, AEP: 24 kV, TCD: 10 cm, SFR: 0.1/0.35 ml/h, CT: cylinder, RS: 100 rpm, ED: 2 h).

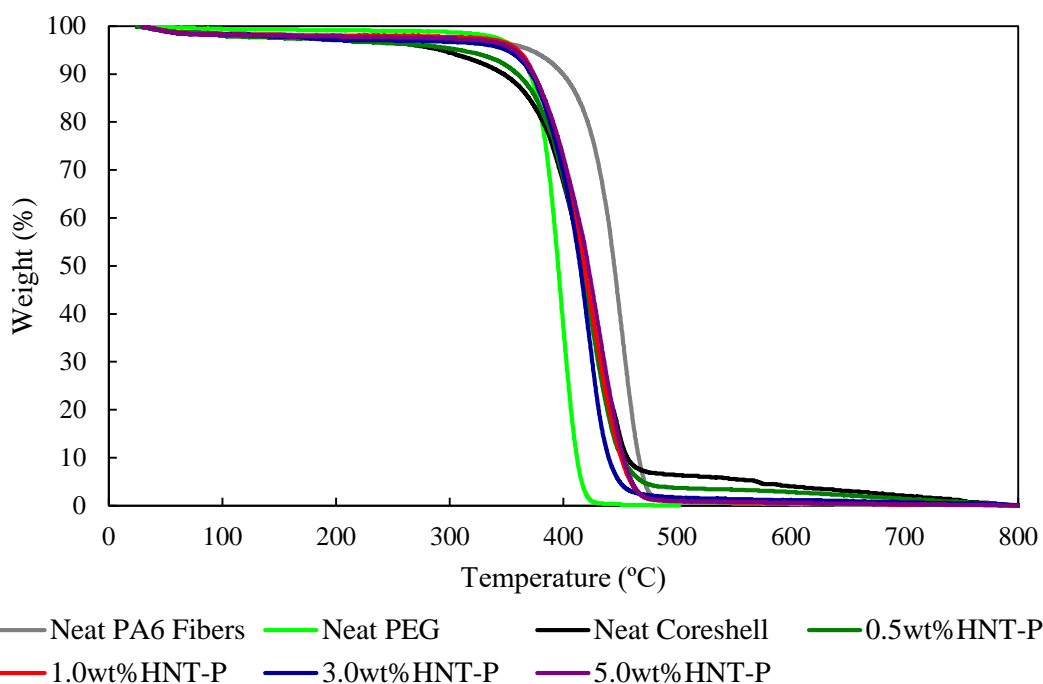


Figure 48. TGA curves of electrospun samples containing different amounts of HNT-P (SC: 30 wt. % PEG/12 wt. % PA6, AEP: 24 kV, TCD: 10 cm, SFR: 0.1/0.35 ml/h, CT: cylinder, RS: 100 rpm, ED: 2 h).

Table 16. Decomposition temperature of nanofibrous samples containing different amounts of HNTs (SC: 30 wt. % PEG/12 wt. % PA6, AEP: 24 kV, TCD: 10 cm, SFR: 0.1/0.35 ml/h, CT: cylinder, RS: 100 rpm, ED: 2 h).

Sample	Decomposition Temperature (°C)
Neat PA6 Fibers	453
Neat PEG	400
Neat Core/shell Fibers	420
0.5 wt. % HNT	428
1 wt. % HNT	428
3 wt. % HNT	426
5 wt. % HNT	427
0.5 wt. % HNT-P	427
1 wt. % HNT-P	425
3 wt. % HNT-P	425
5 wt. % HNT-P	431

### 4.3.3. Differential Scanning Calorimetry (DSC) Analysis

Melting characteristics such as melting temperature and enthalpy of PEG in the nanofibrous samples were determined by DSC analysis. In order to observe the effect of core/shell structure or addition of HNTs and HNT-P into the fibers, DSC analysis was conducted on both neat and composite samples. The DSC analysis results of neat PA6 fibers, neat PEG and neat core/shell fibers additional to HNTs or HNT-P added samples are given in Table 17. Neat PA6 fibers showed melting temperature at 222°C and enthalpy of 83 J/g, whereas neat PEG melted at about 64°C with an enthalpy of 210 J/g. According to the results, the melting temperature of the PEG was significantly decreased due to the difference in degree of crystallinity of the polymer when it was utilized as the core material in production of core/shell structured nanofibers by coaxial electrospinning process. During electrospinning process, PEG solidifies within split seconds inducing a quenching effect. Thus, electrospun PEG could not achieve the same degree of crystallinity as the neat PEG which is in the form of flakes [10]. With the formation of core/shell structured nanofibers, the melting temperature of PEG was decreased from 64°C to 58°C with respect to the neat PEG flakes. This may be due to the negative effect of fast solidification process during electrospinning on the crystallization of PEG. The lower level of crystallinity may have resulted in phase change behavior to take place at slightly lower temperatures. When the melting temperatures of the core/shell nanofibrous samples were analyzed, no significant change was observed with introduction of HNTs or HNT-P into the nanofibers.

Additionally, when the melting enthalpy values of the composite core/shell nanofibers were investigated, it was seen that with HNTs addition, heat storage capacity of the samples increased since the amount of energy absorbed per unit mass of sample increased. This may be both due to the high thermal stability and nucleating effect of the HNTs in the PEG matrix increasing both the crystallinity and the melting temperature of the polymer [73]. 0.5 wt. % HNTs added sample had an enthalpy of 68 J/g whereas with 5 wt. % HNTs addition, this value rose up to 82 J/g. Also by comparing these enthalpy values with the theoretical melting enthalpies calculated

according to their individual PEG contents, the efficiency of enthalpy was determined for all samples. Theoretical enthalpy values of the samples were calculated by multiplying the value obtained from DSC analyses of the neat PEG with their respective PEG mass ratio given in Table 6. The efficiency of enthalpy values also congruently increased with increasing HNTs amount in the system. The 0.5 wt. % HNT added sample showed 78% efficiency of enthalpy whereas 1, 3 and 5 wt. % HNT added samples had 77, 82, 85 and 98% PEG encapsulation efficiency values, respectively. This may be due to the nucleating effect of HNTs in the PEG matrix inducing higher level of crystallization with respect to the PEG content in neat core/shell nanofibers [73]. Since the melting enthalpy of the sample is in the numerator in Equation 3.6, the increase in percent crystallinity of the PEG in the core structure by nucleating agent effect of HNTs increased the encapsulation efficiency.

On the other hand, piranha etched HNTs were also added to the PEG matrix in the core/shell nanofibers. Latent heat of melting and PEG encapsulation efficiency values showed an increasing trend with the addition of piranha etched HNTs except for the 5 wt. % HNT-P sample which had lower enthalpy value even with respect to 5 wt. % HNTs sample. This may be due to the lack of PEG presence in the nanofibrous structure since excess amount of HNT addition to the PEG solvent increased the viscosity to a point where enough PEG could not be dragged by the shell solution during electrospinning. 0.5, 1, 3 and 5 wt. % HNT-P added samples showed efficiencies of 89, 83, 96 and 75%, respectively. This indicates increase in PEG crystallinity in the core structure of the nanofibers, since aligned HNT-P in the core matrix acts as the nucleating agent.

Table 17. DSC data of the nanofibrous samples containing different amounts of HNTs and HNT-P  
(SC: 30 wt. % PEG/12 wt. % PA6, AEP: 24 kV, TCD: 10 cm, SFR: 0.1/0.35 ml/h,  
CT: cylinder, RS: 100 rpm, ED: 2 h).

Samples	Melting Temperature (°C)			Latent Heat of Melting (J/g)	PEG Encapsulation Efficiency (%)
	Onset	Peak	Endset		
Neat PA6 Fibers	213	222	229	83	-
Neat PEG	58	64	70	210	100
Neat Core/Shell Fibers	51	58	66	68	78
0.5 wt. % HNT	51	58	67	68	77
1 wt. % HNT	51	57	64	72	82
3 wt. % HNT	51	57	65	73	85
5 wt. % HNT	52	58	66	82	98
0.5 wt. % HNT-P	51	58	67	78	89
1 wt. % HNT-P	52	59	67	72	83
3 wt. % HNT-P	53	61	65	82	96
5 wt. % HNT-P	51	59	67	63	75

#### 4.3.4. Fourier Transform Infrared Spectroscopy (FTIR) Analysis

The FTIR spectra of the samples produced with different HNTs and HNT-P contents are given in Figures 49- 52. As expected, neat PA6 fibers showed all the characteristic peaks of PA6. High intensity peaks at 1640 and 1540  $\text{cm}^{-1}$  corresponding to C=O axial deformation and N-H bending vibration were apparent in all spectra, respectively. Additionally, peaks at 3300 and 2930  $\text{cm}^{-1}$  were ascribed to N-H stretching and  $\text{CH}_2$  axial deformation, respectively. On the other hand, neat core/shell fibers showed characteristic peaks of both PA6 and PEG suggesting that PEG residue was present on the fiber surfaces. High intensity peaks at 840, 1060, 1097 and 1341  $\text{cm}^{-1}$  were assigned to  $\text{CH}_2$  vibration. Characteristic peaks of PEG were observed at 960 and 1460  $\text{cm}^{-1}$  indicating  $\text{CH}_2$  twisting and C=C atomic stretching, respectively. Significant change in FTIR spectra was not observed for composite core/shell nanofibers with different HNTs content. When the FTIR spectra of HNT-P added samples were

investigated, again characteristic peaks of both PA6 and PEG were observed with no significant change in peak intensities between the samples containing different additive amounts. Finally, as can be seen in Figures 50 and 52, intensity of the characteristic peak of PEG at  $2884\text{ cm}^{-1}$  corresponding to absorption of C-O bond was significantly reduced in all core/shell samples indicating that partial encapsulation of the phase change material was successful.

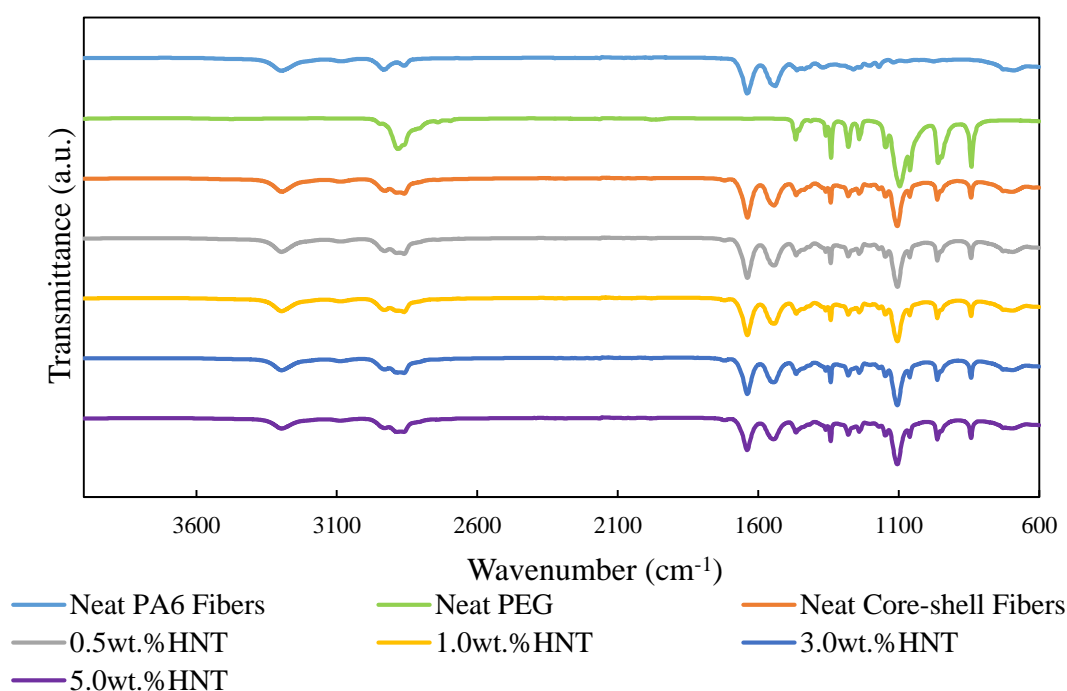


*Figure 49.* FTIR spectra of HNTs added composite nanofibrous samples (SC: 30 wt. % PEG/12 wt. % PA6, AEP: 24 kV, TCD: 10 cm, SFR: 0.1/0.35 ml/h, CT: cylinder, RS: 100 rpm, ED: 2 h).

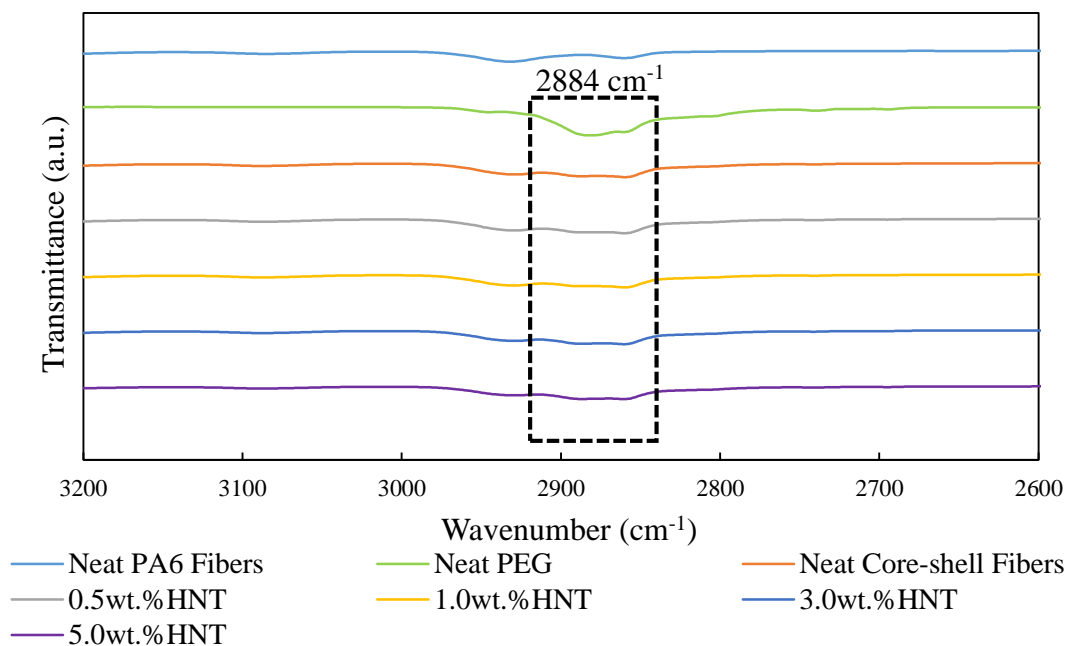


Figure 50. Zoomed FTIR spectra of HNTs added composite nanofibrous samples (SC: 30 wt. % PEG/12 wt. % PA6, AEP: 24 kV, TCD: 10 cm, SFR: 0.1/0.35 ml/h, CT: cylinder, RS: 100 rpm, ED: 2 h).

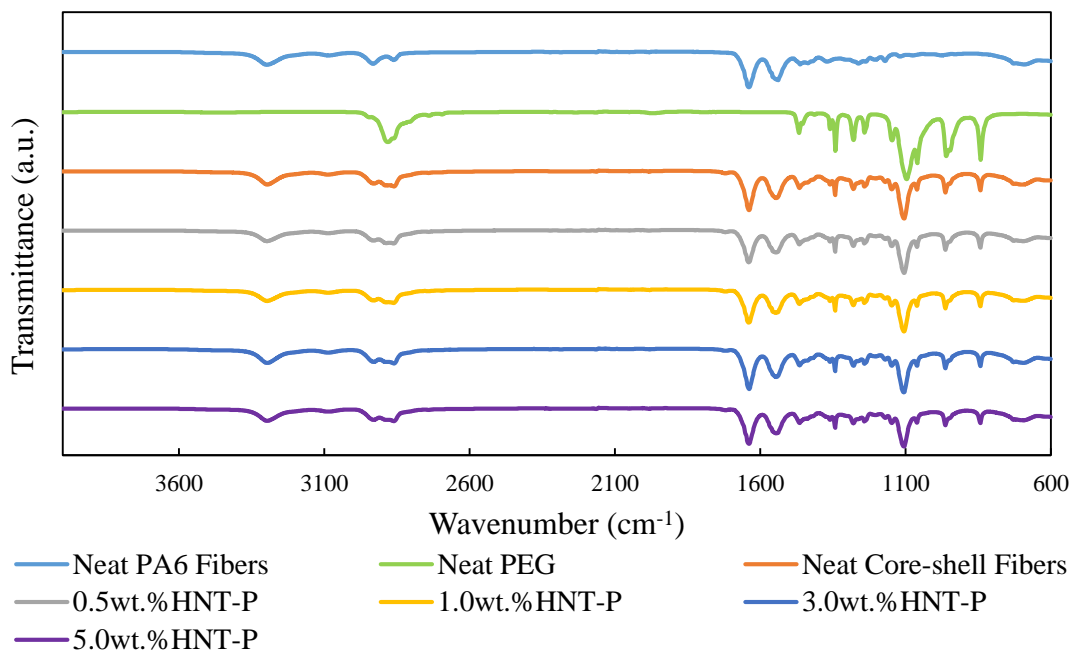
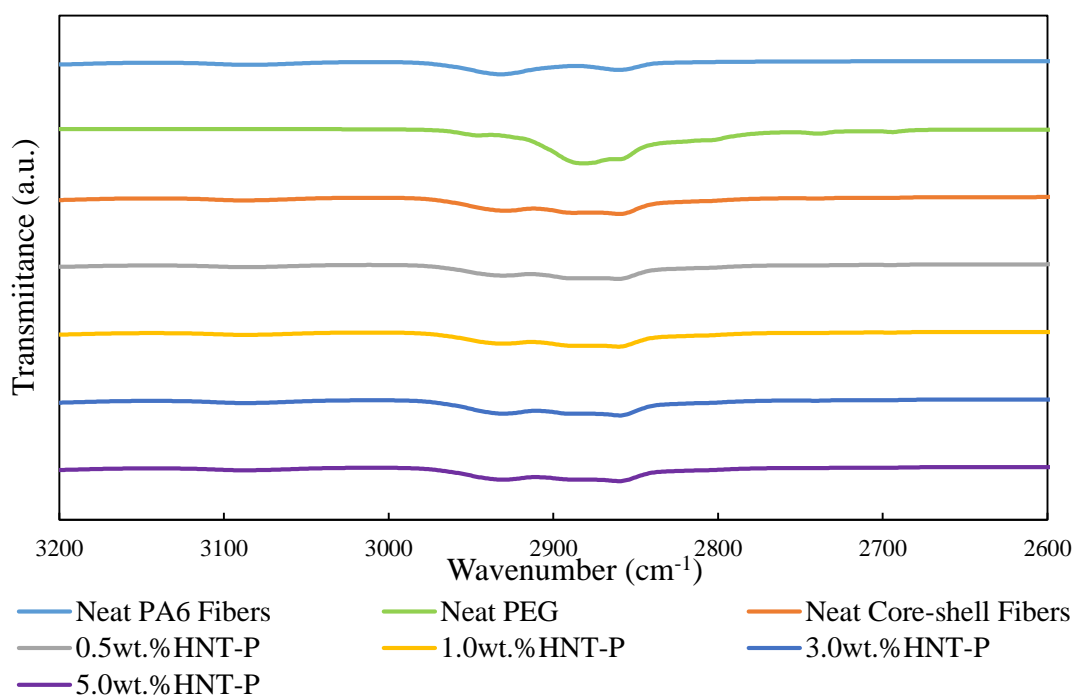


Figure 51. FTIR spectra of HNT-P added composite nanofibrous samples (SC: 30 wt. % PEG/12 wt. % PA6, AEP: 24 kV, TCD: 10 cm, SFR: 0.1/0.35 ml/h, CT: cylinder, RS: 100 rpm, ED: 2 h).



*Figure 52. Zoomed FTIR spectra of HNT-P added composite nanofibrous samples (SC: 30 wt. % PEG/12 wt. % PA6, AEP: 24 kV, TCD: 10 cm, SFR: 0.1/0.35 ml/h, CT: cylinder, RS: 100 rpm, ED: 2 h).*

#### 4.3.5. Tensile Test Results

Tensile testing was conducted on the electrospun nanofibrous mats in order to see the effect of both core/shell morphology and the composite structure on tensile strength, modulus and elongation at break properties. Detailed tensile testing data can be seen in Table C.1 in Appendix C. According to the tensile strength values of the samples that are shown in Figure 53, mat comprised of neat PA6 fibers revealed the highest strength property. As the PEG was introduced into the system, the tensile strength of the sample slightly decreased due to the addition of low molecular weight polymer. Introduction of HNTs or HNT-P did not significantly change the tensile strength of the nanofibrous samples. Tensile strength value of 3 wt. % HNT-P and 5 wt. % HNT-P samples were 7.8 MPa being the closest data to the neat PA6 mat.

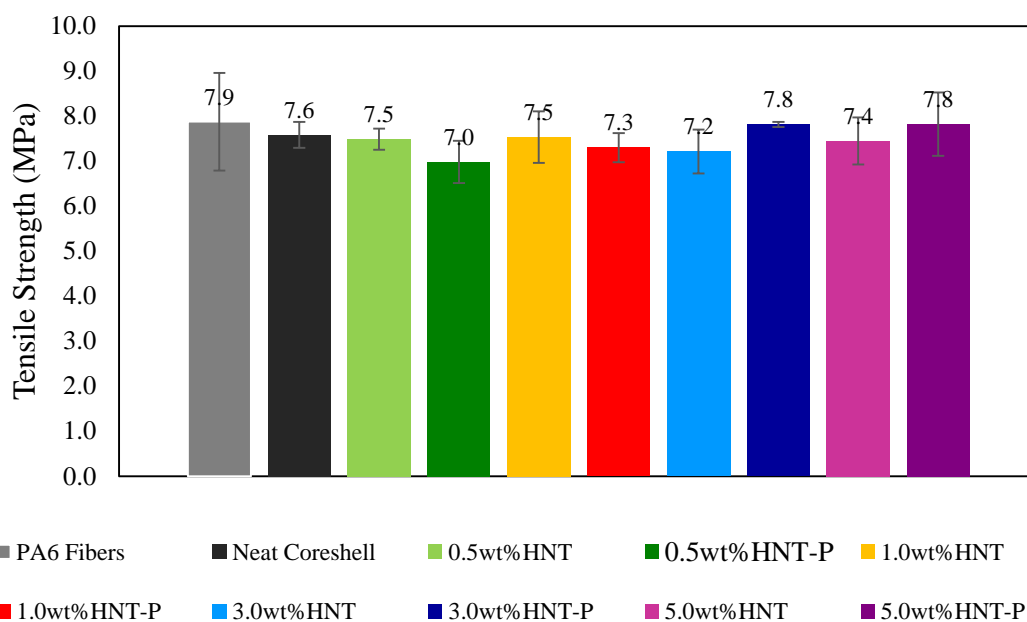


*Figure 53.* Bar chart depicting the tensile strength values of the electrospun nanofibrous samples (SC: 30 wt. % PEG/12 wt. % PA6, AEP: 24 kV, TCD: 10 cm, SFR: 0.1/0.35 ml/h, CT: cylinder, RS: 100 rpm, ED: 2 h).

Tensile modulus values of the neat and composite nanofibrous samples can be seen in Figure 54. Neat PA6 fibrous mat revealed a tensile modulus of 88.5 MPa. Since PA6 was known to be an engineering polymer with high mechanical properties, the low tensile modulus of neat PA6 fibrous mat with respect to composite mats consisting of core/shell fibers was expected. Neat core/shell nanofibers revealed tensile modulus value of 91.5 MPa. Although slight increase in tensile modulus values were observed with the addition of HNTs into the core/shell nanofibers, HNT-P introduction revealed significant effect on the tensile modulus of the samples. Since HNTs have high modulus owing to their inorganic crystalline structure as opposed to polymeric substances, they also increase the modulus of the composites upon introduction to the polymer matrix. As seen in the SEM images of HNTs added samples, effusion of nanotubes from the fiber structures was present resulting in lower increase in modulus values than HNT-P added nanofibrous mats. The drastic increase in tensile modulus of the samples with HNT-P content can be accepted as an evidence towards successful

encapsulation of nano additives in the nanofibers. On the other hand, the 5 wt. % HNT added nanofibrous sample's tensile modulus value was lower with respect to the other samples. This was due to the effusion of the HNTs particles on to the fiber surfaces at such high concentrations. Since nanotubes were not in the polymer matrix they could not fully support the materials during extension revealing decreased tensile modulus values.

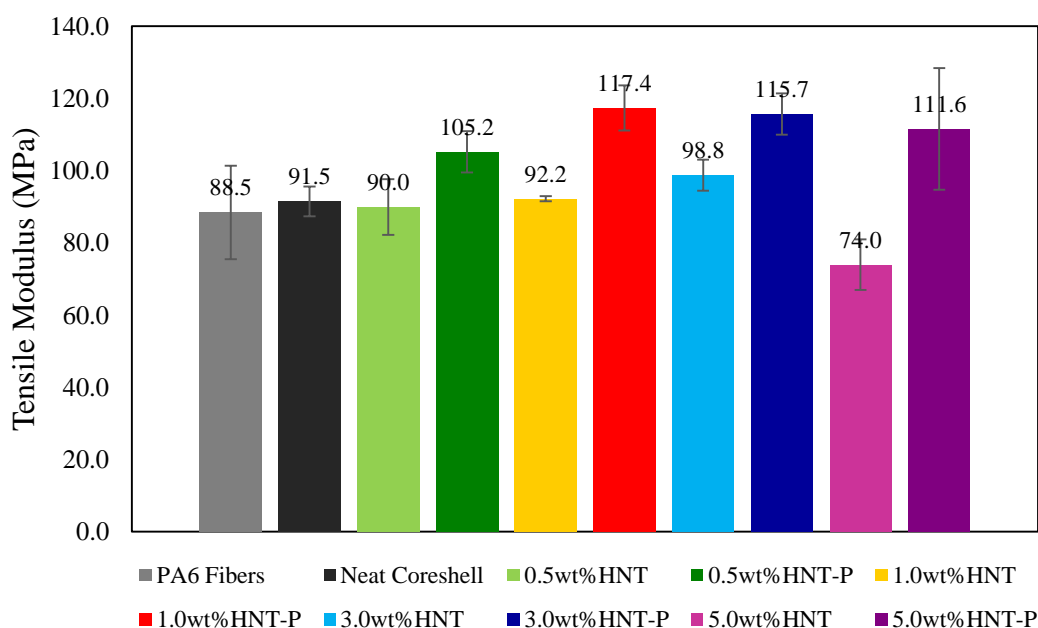


Figure 54. Bar chart depicting the tensile modulus values of the electrospun nanofibrous samples (SC: 30 wt. % PEG/12 wt. % PA6, AEP: 24 kV, TCD: 10 cm, SFR: 0.1/0.35 ml/h, CT: cylinder, RS: 100 rpm, ED: 2 h).

The elongation at break values of both neat and composite nanofibrous samples are given in Figure 55. As opposed to the tensile modulus data, elongation at break values decreased with PEG addition to the nanofibrous system. This is due to the brittle nature of the PEG. Lower elongation at break property of PEG with respect to PA6 was due to its lower molecular weight and less molecular entanglements in its structure. As the HNTs or HNT-P amount was increased in the nanofibers, the elongation at break

values of the nanofibrous mats decreased gradually. In the case of HNTs addition, since effusion of the nano additives was present no significant effect of the composite structure on the elongation at break property of the nanofibrous samples could be observed. Despite better encapsulation of additives with addition of surface activated nanotubes, agglomerations occurred and acted as stress concentrators leading to low elongation at break values. Although the surface activation strengthened the affinity of the nanotubes towards PEG matrix, it also led to formation of agglomerates since the interaction between HNTs increased concurrently. On the other hand, 3 wt. % HNT-P sample showed even higher elongation at break value than neat PA6 fibrous mats due to the better alignment and dispersion of nanotubes in the core structure of nanofibers. It can be said that up to 3 wt. % HNT-P concentration, additive amount was not sufficient for homogeneous dispersion throughout the electrospun mat. As can be seen in the SEM images of the 3 wt. % HNT-P sample, there was less agglomerations and more uniform nanofiber morphology proving better dispersion of HNT-P particles.

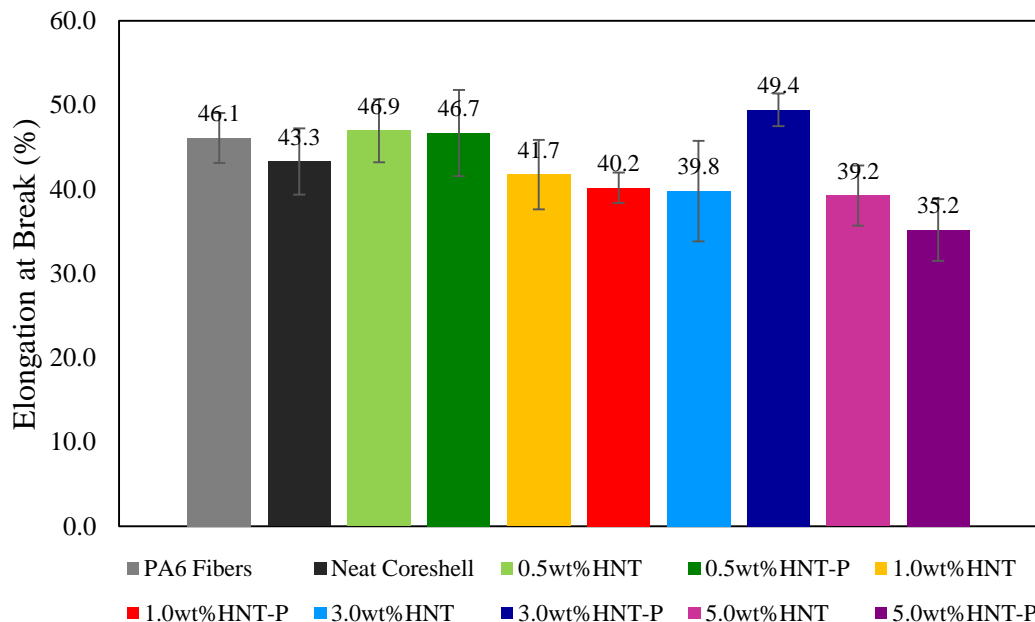


Figure 55. Bar chart depicting the elongation at break values of the electrospun nanofibrous samples (SC: 30 wt. % PEG/12 wt. % PA6, AEP: 24 kV, TCD: 10 cm, SFR: 0.1/0.35 ml/h, CT: cylinder, RS: 100 rpm, ED: 2 h).

#### 4.3.6. Thermal Cyclic Test

Thermal cyclic test was conducted on the produced neat and composite samples in order to determine the effectiveness of the encapsulation of PEG in the nanofiber core structures. Neat core/shell, 3 wt. % HNTs added and 3 wt. % HNT-P added nanofibrous samples were chosen to be subjected to the cyclic test. Resulting thermal cyclic test data of the neat core/shell nanofibrous sample is given in Table 18. It can be seen that the neat sample revealed an initial melting enthalpy of 69.07 J/g and after ten heating-cooling cycles, this value was decreased to 60.86 J/g revealing that 88.11% of the initial PEG melting enthalpy was preserved. This showed that the nanofibrous sample maintained a significant portion of its heat storage ability even after several uses. In Figure 56, the DSC curves of the sample obtained during first and tenth heating are given. From changes in the areas of the melting peaks, the decrease in melting enthalpy upon multiple heating-cooling cycles can be determined. The thermal cyclic test data of 3 wt. % HNT added composite nanofibrous sample are given in Table 19. The DSC curves of the composite sample obtained during first and tenth heating are given in Figure 57. From the figure, again the change in the areas of the melting peaks reveals the decrease in enthalpy upon several heating-cooling cycles. When 3 wt. % HNTs added samples were subjected to the cyclic test, the initial melting enthalpy value was observed to be 78.86 J/g, revealing higher initial melting enthalpy value with respect to neat core/shell nanofibrous sample. It preserved 93.36% of its initial melting enthalpy with a final value of 73.62 J/g. This showed that HNTs addition not only increased the initial PEG encapsulation, but it also enhanced the energy absorption capacity of the sample even after multiple uses. This was due to HNTs acting as nucleating agent increasing the crystallization of PEG during solidification processes. As the % crystallization of the PEG was enhanced or even preserved during solidifications, less portion of melting enthalpy value was lost upon cycles. Finally, 3 wt. % HNT-P added nanofibrous samples revealed a first melting enthalpy of 78.42 J/g. This value was decreased to 72.8 J/g after 10 cycles resulting in preservation of 92.83% of the initial value. The thermal cyclic test data and the resulting DSC curves

of the sample are given in Table 20 and Figure 58, respectively. According to the results it was seen that although incorporation of the HNTs in the nanofiber structure resulted in enhanced durability of the material after many uses, the piranha etching of the HNTs did not further increased this property. Both composite samples showed higher cyclic performance with respect to neat core/shell nanofibers.

Table 18. *Thermal cyclic test data of neat core/shell nanofibrous sample*

(SC: 30 wt. % PEG/12 wt. % PA6, AEP: 24 kV, TCD: 10 cm, SFR: 0.1/0.35 ml/h, CT: cylinder, RS: 100 rpm, ED: 2 h).

<b># of Heating</b>	<b>Onset Temperature (°C)</b>	<b>Peak Temperature (°C)</b>	<b>Endset Temperature (°C)</b>	<b>Melting Enthalpy (J/g)</b>	<b>Enthalpy Maintained (%)</b>
1	51.69	59.02	63.14	69.07	-
2	52.44	59.81	64.05	63.09	91.34
3	54.53	60.79	65.05	61.80	89.47
4	54.51	60.78	64.98	61.79	89.46
5	54.73	60.82	65.06	61.60	89.18
6	54.68	60.94	65.12	61.21	88.62
7	54.78	60.95	65.15	61.05	88.39
8	54.86	60.94	65.15	60.97	88.27
9	54.81	61.04	65.15	60.86	88.11
10	54.82	61.02	65.19	60.86	88.11

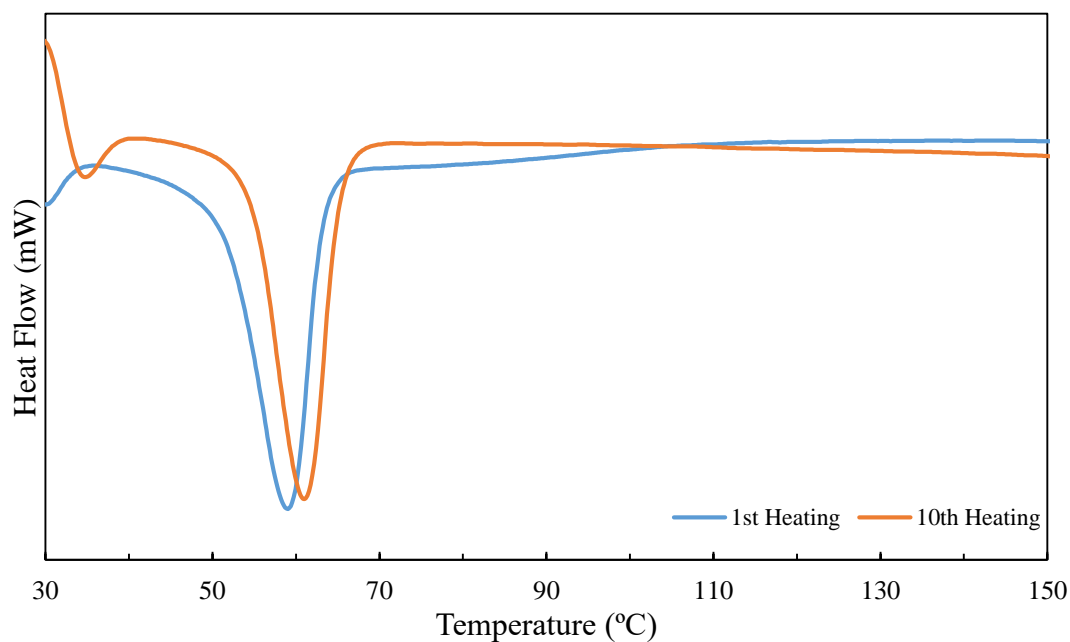


Figure 56. DSC curves of the neat core/shell structured nanofibrous sample during 1<sup>st</sup> and 10<sup>th</sup> heating (SC: 30 wt. % PEG/12 wt. % PA6, AEP: 24 kV, TCD: 10 cm, SFR: 0.1/0.35 ml/h, CT: cylinder, RS: 100 rpm, ED: 2 h).

Table 19. Thermal cyclic test data of the 3 wt. % HNT added core/shell structured nanofibrous sample (SC: 30 wt. % PEG/12 wt. % PA6, AEP: 24 kV, TCD: 10 cm, SFR: 0.1/0.35 ml/h, CT: cylinder, RS: 100 rpm, ED: 2 h).

# of Heating	Onset Temperature (°C)	Peak Temperature (°C)	Endset Temperature (°C)	Melting Enthalpy (J/g)	Enthalpy Maintained (%)
1	50.55	58.19	62.65	78.86	-
2	52.26	59.12	63.56	74.95	95.04
3	53.92	60.13	64.33	74.35	94.28
4	54.16	60.12	64.46	74.44	94.40
5	54.19	60.20	64.51	74.37	94.31
6	54.23	60.13	64.54	74.51	94.48
7	54.13	60.11	64.47	74.60	94.60
8	54.14	60.27	64.56	74.27	94.18
9	54.13	60.08	64.51	74.10	93.96
10	54.00	60.20	64.50	73.62	93.36

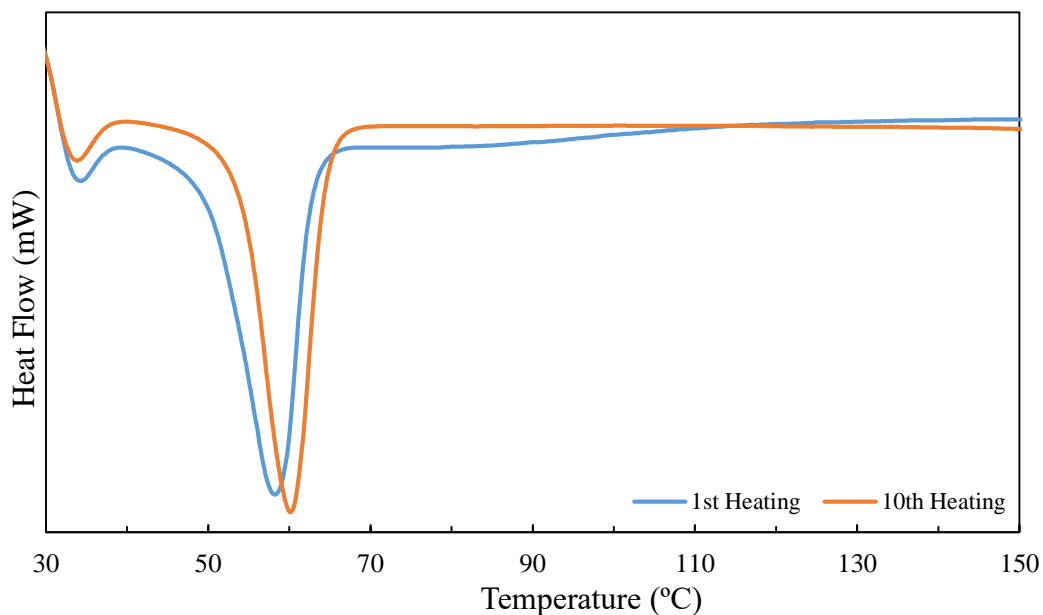


Figure 57. DSC curves of 3 wt. % HNT added core/shell structured nanofibrous sample during 1<sup>st</sup> and 10<sup>th</sup> heating (SC: 30 wt. % PEG/12 wt. % PA6, AEP: 24 kV, TCD: 10 cm, SFR: 0.1/0.35 ml/h, CT: cylinder, RS: 100 rpm, ED: 2 h).

Table 20. Thermal cyclic test data of the 3 wt. % HNT-P added core/shell structured nanofibrous sample (SC: 30 wt. % PEG/12 wt. % PA6, AEP: 24 kV, TCD: 10 cm, SFR: 0.1/0.35 ml/h, CT: cylinder, RS: 100 rpm, ED: 2 h).

# of Heating	Onset Temperature (°C)	Peak Temperature (°C)	Endset Temperature (°C)	Melting Enthalpy (J/g)	Enthalpy Maintained (%)
1	51.57	59.37	63.33	78.42	-
2	54.31	60.55	64.72	75.18	95.87
3	54.34	60.64	64.83	75.52	96.30
4	54.47	60.59	64.84	75.42	96.17
5	54.65	60.74	64.97	75.18	95.87
6	54.46	60.72	64.91	74.14	94.54
7	54.21	60.63	64.89	73.51	93.74
8	54.36	60.57	64.83	72.91	92.97
9	54.07	60.55	64.76	72.7	92.71
10	54.01	60.55	64.66	72.8	92.83

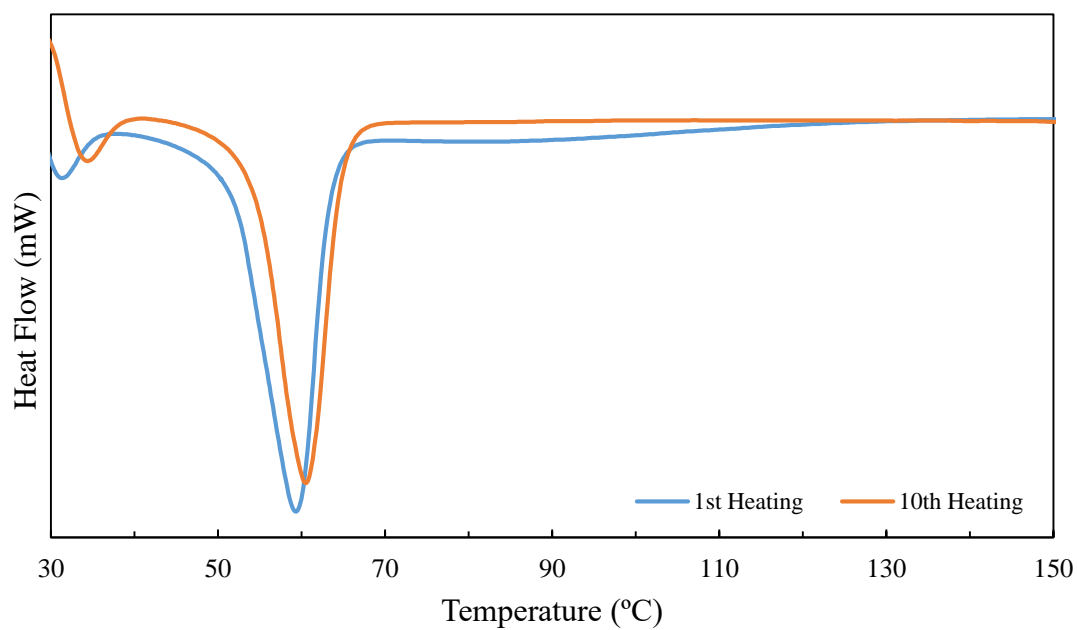


Figure 58. DSC curves of 3 wt. % HNT added core/shell structured nanofibrous sample during 1<sup>st</sup> and 10<sup>th</sup> heating (SC: 30 wt. % PEG/12 wt. % PA6, AEP: 24 kV, TCD: 10 cm, SFR: 0.1/0.35 ml/h, CT: cylinder, RS: 100 rpm, ED: 2 h).

## CHAPTER 5

### CONCLUSIONS

When all the experiments conducted within the scope of the thesis were evaluated, the following results were obtained;

1. Core/shell structured PEG/PA6 and composite PEG/PA6/HNTs nanofibers were successfully produced.
2. Effects of polymer solution concentration on the nanofiber morphology was determined. It was found that when 30 wt. % PEG and 12 wt. % PA6 solutions were used, more stable electrospinning process resulting in uniform morphology was achieved.
3. Applied electrical potential during the coaxial electrospinning process was optimized by considering the nanofiber morphology and heat storage property. It was determined that under 24 kV of applied electrical potential, more uniform nanofibers were observed with higher latent heat of melting with respect to the samples produced under 20 and 28 kV.
4. Feed rate of the core/shell solutions were optimized by morphology analysis. It was found that 0.1 ml/h, 0.35 ml/h of core/shell solution feed rates resulted in more uniform nanofiber structure.
5. The best coaxial electrospinning parameters were determined to be 30 wt. % PEG, 12 wt. % PA6 solution concentrations, 24 kV applied electrical potential, 10 cm tip to collector distance and 0.1/0.35 ml/h core/shell solution feed rates resulting in average fiber diameters of 141 nm with standard deviation of 35 nm. The resulting nanofibrous sample possessed decomposition temperature of 433°C and latent heat enthalpy of 68 J/g.
6. Optimized process and solution parameters of coaxial electrospinning process were also used in production of HNTs containing composite nanofibrous samples.

7. HNTs were successfully added to the core solution with 0.5, 1, 3 and 5 wt. % concentrations with respect to PEG amount in order to acquire a composite material. It was observed that effusion of HNTs from the nanofibers occurred and the average fiber diameters decreased due to the unsuccessful encapsulation of nanoparticles in the fibers.
8. Although the encapsulation of the HNTs were not fully achieved, the melting enthalpy of the nanofibrous samples increased with increasing additive content. 5 wt. % HNTs containing composite sample had melting enthalpy of 82 J/g.
9. HNTs were activated by acid etching. Piranha solution was used in activation of the HNTs. Etched HNTs (HNT-P) were added to the core solution with concentrations of 0.5, 1, 3 and 5 wt. % with respect to the PEG amount. Resulting samples showed increase in decomposition temperature, latent heat enthalpy and tensile modulus values. 3 wt. % HNT-P revealed decomposition temperature of 425°C, melting enthalpy of 82 J/g and tensile modulus of 115.7 MPa. Additionally, 3 wt. % HNT-P sample showed PEG encapsulation efficiency of 96%.
10. Finally, thermal cyclic test was conducted on neat core/shell, 3 wt. % HNTs and 3 wt. % HNT-P samples. Upon ten consecutive melting-cooling cycles, neat core/shell structured, 3 wt. % HNTs and 3 wt. % HNT-P containing nanofibrous samples maintained 88.11%, 93.36% and 92.83% of their initial melting enthalpy values indicating high durability. By this way, development of thermal energy storage material from neat and composite core/shell structured nanofibers was successfully accomplished by utilizing PEG as the phase change material in coaxial electrospinning method.
11. Important contribution to the literature was made since to the best of our knowledge, there was a lack of study on the thermal energy storage, tensile, and thermal properties of coaxially electrospun HNTs added PEG/PA6 nanofibrous mats. Considerable enhancement of thermal energy storage, tensile and thermal properties of the nanofibers upon development of composite structure by addition of HNTs into the core structure constitutes the novelty of the study.

## REFERENCES

- [1] B. S. Kim and I. S. Kim, "Recent nanofiber technologies," *Polym. Rev.*, vol. 51, no. 3, pp. 235–238, 2011.
- [2] N. Bhardwaj and S. C. Kundu, "Electrospinning: A fascinating fiber fabrication technique," *Biotechnol. Adv.*, vol. 28, no. 3, pp. 325–347, 2010.
- [3] Y. Wu, C. Chen, Y. Jia, J. Wu, Y. Huang, and L. Wang, "Review on electrospun ultrafine phase change fibers (PCFs) for thermal energy storage," *Appl. Energy*, vol. 210, no. March 2017, pp. 167–181, 2018.
- [4] J. Pelipenko, P. Kocbek, and J. Kristl, "Critical attributes of nanofibers: Preparation, drug loading, and tissue regeneration," *Int. J. Pharm.*, vol. 484, no. 1–2, pp. 57–74, 2015.
- [5] D. Cho, E. Zhmayev, and Y. L. Joo, "Structural studies of electrospun nylon 6 fibers from solution and melt," *Polymer (Guildf.)*, vol. 52, no. 20, pp. 4600–4609, 2011.
- [6] S. Zhang, W. S. Shim, and J. Kim, "Design of ultra-fine nonwovens via electrospinning of Nylon 6: Spinning parameters and filtration efficiency," *Mater. Des.*, vol. 30, no. 9, pp. 3659–3666, 2009.
- [7] Y. Cai *et al.*, "Electrospun ultrafine composite fibers consisting of lauric acid and polyamide 6 as form-stable phase change materials for storage and retrieval of solar thermal energy," *Sol. Energy Mater. Sol. Cells*, vol. 103, pp. 53–61, 2012.
- [8] G. Cavallaro, R. De Lisi, G. Lazzara, and S. Milioto, "Polyethylene glycol/clay nanotubes composites: Thermal properties and structure," *J. Therm. Anal. Calorim.*, vol. 112, no. 1, pp. 383–389, 2013.

- [9] S. Thanakkasaranee and J. Seo, "Effect of halloysite nanotubes on shape stabilities of polyethylene glycol-based composite phase change materials," *Int. J. Heat Mass Transf.*, vol. 132, pp. 154–161, 2019.
- [10] A. Babapoor, G. Karimi, S. I. Golestaneh, and M. A. Mezjin, "Coaxial electrospun PEG/PA6 composite fibers: Fabrication and characterization," *Appl. Therm. Eng.*, vol. 118, pp. 398–407, 2017.
- [11] A. Babapoor, G. Karimi, and M. Khorram, "Fabrication and characterization of nanofiber-nanoparticle-composites with phase change materials by electrospinning," *Appl. Therm. Eng.*, vol. 99, pp. 1225–1235, 2016.
- [12] Kenry and C. T. Lim, "Nanofiber technology: current status and emerging developments," *Prog. Polym. Sci.*, vol. 70, pp. 1–17, 2017.
- [13] Z. Song *et al.*, "Effects of solvent on structures and properties of electrospun poly(ethylene oxide) nanofibers," *J. Appl. Polym. Sci.*, vol. 135, no. 5, pp. 1–10, 2018.
- [14] M. Milwich, T. Speck, O. Speck, T. Stegmaier, and H. Planck, "Biomimetics and technical textiles: Solving engineering problems with the help of nature's wisdom," *Am. J. Bot.*, vol. 93, no. 10, pp. 1455–1465, 2006.
- [15] C. J. Luo, S. D. Stoyanov, E. Stride, E. Pelan, and M. Edirisinghe, "Electrospinning versus fibre production methods: From specifics to technological convergence," *Chem. Soc. Rev.*, vol. 41, no. 13, pp. 4708–4735, 2012.
- [16] J. Di, Y. Zhao, Y. Song, L. Jiang, and H. Chen, "Nanowire-in-Microtube Structured Core / Shell Fibers via Multifluidic Coaxial Electrospinning," vol. 26, no. 23, pp. 11291–11296, 2010.
- [17] European Union, *Statistical Pocketbook in figures*. 2018.

- [18] I. Sarbu and C. Sebarchievici, "A comprehensive review of thermal energy storage," *Sustain.*, vol. 10, no. 1, 2018.
- [19] A. Kumar and S. K. Shukla, "A Review on Thermal Energy Storage Unit for Solar Thermal Power Plant Application," *Energy Procedia*, vol. 74, pp. 462–469, 2015.
- [20] M. M. Farid, A. M. Khudhair, S. A. K. Razack, and S. Al-Hallaj, "A review on phase change energy storage: Materials and applications," *Energy Convers. Manag.*, vol. 45, no. 9–10, pp. 1597–1615, 2004.
- [21] S. Ayyappan, K. Mayilsamy, and V. V. Sreenarayanan, "Performance improvement studies in a solar greenhouse drier using sensible heat storage materials," *Heat Mass Transf. und Stoffuebertragung*, vol. 52, no. 3, pp. 459–467, 2016.
- [22] A. Kasaeian, F. Pourfayaz, and E. Khodabandeh, "Experimental studies on the applications of PCMs and nano-PCMs in buildings : A critical review," *Energy Build.*, vol. 154, pp. 96–112, 2017.
- [23] A. Sharma, V. V Tyagi, C. R. Chen, and D. Buddhi, "Review on thermal energy storage with phase change materials and applications," vol. 13, pp. 318–345, 2009.
- [24] M. Noro, R. M. Lazzarin, and F. Busato, "Solar cooling and heating plants : An energy and economic analysis of liquid sensible vs phase change material ( PCM ) heat storage Le refroidissement solaire et les installations de chauffage : ' nerge ' tique et e ' conomique de ^ ce l ' analyse e compa," *Int. J. Refrig.*, vol. 39, no. 0, pp. 104–116, 2013.
- [25] O. Al-abbasi, A. Abdelkefi, and M. Ghommem, "Modeling and assessment of a thermochemical energy storage using salt hydrates," no. June, pp. 2149–2161, 2017.

- [26] H. Ge, H. Li, S. Mei, and J. Liu, “Low melting point liquid metal as a new class of phase change material: An emerging frontier in energy area,” *Renew. Sustain. Energy Rev.*, vol. 21, pp. 331–346, 2013.
- [27] H. Kerskes, B. Mette, F. Bertsch, S. Asenbeck, and H. Drück, “Chemical energy storage using reversible solid / gas-reactions ( CWS ) – results of the research project,” vol. 30, pp. 294–304, 2012.
- [28] W. Su, J. Darkwa, and G. Kokogiannakis, “Review of solid-liquid phase change materials and their encapsulation technologies,” *Renew. Sustain. Energy Rev.*, vol. 48, pp. 373–391, 2015.
- [29] S. K. Ghosh, *Functional Coatings by Polymer Microencapsulation*. 2006.
- [30] L. Wei, Z. Xing-xiang, W. Xue-chen, and N. Jian-jin, “Preparation and characterization of microencapsulated phase change material with low remnant formaldehyde content,” vol. 106, pp. 437–442, 2007.
- [31] K. Hong and S. Park, “Melamine resin microcapsules containing fragrant oil : synthesis and characterization,” vol. 58, pp. 128–131, 1999.
- [32] F. Salaün, E. Devaux, S. Bourbigot, and P. Rumeau, “Development of Phase Change Materials in Clothing Part I: Formulation of Microencapsulated Phase Change,” *Text. Res. J.*, vol. 80, no. 3, pp. 195–205, 2010.
- [33] P. Chaiyasat, Z. Islam, and A. Chaiyasat, “RSC Advances,” pp. 10202–10207, 2013.
- [34] S. Alay, C. Alkan, and F. Göde, “Thermochimica Acta Synthesis and characterization of poly ( methyl methacrylate )/ n-hexadecane microcapsules using different cross-linkers and their application to some fabrics,” *Thermochim. Acta*, vol. 518, no. 1–2, pp. 1–8, 2011.
- [35] K. Pielichowska and K. Pielichowski, “Phase change materials for thermal energy storage,” *Prog. Mater. Sci.*, vol. 65, pp. 67–123, 2014.

- [36] J. J. Richardson, M. Björnmalm, and F. Caruso, "Technology-driven layer-by-layer assembly of nanofilms," *Science* (80-. ), vol. 348, no. 6233, 2015.
- [37] M. Naeimirad, A. Zadhoush, R. Kotek, R. Esmaeely Neisiany, S. Nouri Khorasani, and S. Ramakrishna, "Recent advances in core/shell bicomponent fibers and nanofibers: A review," *J. Appl. Polym. Sci.*, vol. 135, no. 21, 2018.
- [38] A. Arecchi, S. Mannino, and J. Weiss, "Electrospinning of poly(vinyl alcohol) nanofibers loaded with hexadecane nanodroplets," *J. Food Sci.*, vol. 75, no. 6, pp. 80–88, 2010.
- [39] E. Zdraveva, J. Fang, B. Mijovic, and T. Lin, *Electrospun nanofibers*. 2016.
- [40] S. Ramakrishna, K. Fujihara, W.-E. Teo, T.-C. Lim, and Z. Ma, *An Introduction to Electrospinning and Nanofibers*. 2012.
- [41] C. Changzhong, W. Linge, and H. Yong, "Role of Mn of PEG in the Morphology and Properties of Electrospun PEG/CA Composite Fibers for Thermal Energy Storage," *AIChE J.*, vol. 59, no. 3, pp. 215–228, 2012.
- [42] N. Wang *et al.*, "Multicomponent phase change microfibers prepared by temperature control multifluidic electrospinning," *Macromol. Rapid Commun.*, vol. 31, no. 18, pp. 1622–1627, 2010.
- [43] J. Yoon, H. S. Yang, B. S. Lee, and W. R. Yu, "Recent Progress in Coaxial Electrospinning: New Parameters, Various Structures, and Wide Applications," *Adv. Mater.*, vol. 30, no. 42, pp. 1–23, 2018.
- [44] S. K. Tiwari and S. S. Venkatraman, "Importance of viscosity parameters in electrospinning: Of monolithic and core-shell fibers," *Mater. Sci. Eng. C*, vol. 32, no. 5, pp. 1037–1042, 2012.
- [45] N. Kaerkitcha, S. Chuangchote, K. Hachiya, and T. Sagawa, "Influence of the viscosity ratio of polyacrylonitrile/poly(methyl methacrylate) solutions on core-shell fibers prepared by coaxial electrospinning," *Polym. J.*, 2017.

- [46] Seeram Ramakrishna, M. Zamani, and Molamma P Prabhakaran, “Advances in drug delivery via electrospun and electrosprayed nanomaterials,” *Int. J. Nanomedicine*, p. 2997, 2013.
- [47] R. P. Gonçalves, F. F. F. da Silva, P. H. S. Picciani, and M. L. Dias, “Morphology and Thermal Properties of Core-Shell PVA/PLA Ultrafine Fibers Produced by Coaxial Electrospinning,” *Mater. Sci. Appl.*, vol. 06, no. 02, pp. 189–199, 2015.
- [48] L. Sisti *et al.*, “Multicomponent reinforcing system for poly(butylene succinate): Composites containing poly(l-lactide) electrospun mats loaded with graphene,” *Polym. Test.*, vol. 50, pp. 283–291, 2016.
- [49] L. Li, L. M. Bellan, H. G. Craighead, and M. W. Frey, “Formation and properties of nylon-6 and nylon-6/montmorillonite composite nanofibers,” *Polymer (Guildf.)*, vol. 47, no. 17, pp. 6208–6217, 2006.
- [50] E. Ozdemir and J. Hacaloglu, “Thermal degradation of Polylactide/Poly(ethylene glycol) fibers and composite fibers involving organoclay,” *J. Anal. Appl. Pyrolysis*, vol. 129, no. August 2017, pp. 181–188, 2018.
- [51] S. I. Golestaneh, G. Karimi, A. Babapoor, and F. Torabi, “Thermal performance of co-electrospun fatty acid nanofiber composites in the presence of nanoparticles,” *Appl. Energy*, vol. 212, no. April 2017, pp. 552–564, 2018.
- [52] Z. M. Huang, Y. Z. Zhang, M. Kotaki, and S. Ramakrishna, “A review on polymer nanofibers by electrospinning and their applications in nanocomposites,” *Compos. Sci. Technol.*, vol. 63, no. 15, pp. 2223–2253, 2003.
- [53] X. Min *et al.*, “Enhanced thermal properties of novel shape-stabilized PEG composite phase change materials with radial mesoporous silica sphere for thermal energy storage,” *Sci. Rep.*, vol. 5, no. June, pp. 1–11, 2015.

- [54] P. Yuan, D. Tan, and F. Annabi-Bergaya, "Properties and applications of halloysite nanotubes: Recent research advances and future prospects," *Appl. Clay Sci.*, vol. 112–113, pp. 75–93, 2015.
- [55] Y. Dong *et al.*, "Polylactic acid (PLA)/halloysite nanotube (HNT) composite mats: Influence of HNT content and modification," *Compos. Part A Appl. Sci. Manuf.*, vol. 76, pp. 28–36, 2015.
- [56] "Tecomid NB40 NL E Technical Data Sheet, (2012) 2012. [http://www.eurotecep.com/s/1404/i/TDS\\_Tecomid\\_NB40\\_NL\\_E.pdf](http://www.eurotecep.com/s/1404/i/TDS_Tecomid_NB40_NL_E.pdf)," 2012.
- [57] Merck, "PEG 6000, Molecular Biology Grade [PDF]. (2017, February 06). Merck.," *Saf. Data Sheet*, no. 1907, pp. 1–13, 2015.
- [58] "Halloysite Nanoclay (CAS 1332-58-7), Product specification, Sigma-Aldrich," *Build. Res. Inf.*, vol. 21, no. 1, pp. 21–22, 1993.
- [59] Z. Liu, X. Fu, L. Jiang, B. Wu, J. Wang, and J. Lei, "Solvent-free synthesis and properties of novel solid-solid phase change materials with biodegradable castor oil for thermal energy storage," *Sol. Energy Mater. Sol. Cells*, vol. 147, no. April 2016, pp. 177–184, 2016.
- [60] P. Heikkilä and A. Harlin, "Parameter study of electrospinning of polyamide-6," *Eur. Polym. J.*, vol. 44, no. 10, pp. 3067–3079, 2008.
- [61] M. Pakravan, M.-C. Heuzey, and A. Ajji, "Core–Shell Structured PEO-Chitosan Nanofibers by Coaxial.pdf." *Biomacromolecules*, Montreal, pp. 412–421, 2012.
- [62] E. C. B. Noyan, E. Onder, N. Sarier, and R. Arat, "Development of heat storing poly(acrylonitrile) nanofibers by coaxial electrospinning," *Thermochim. Acta*, vol. 662, no. February, pp. 135–148, 2018.

- [63] O. Ero-Phillips, M. Jenkins, and A. Stamboulis, "Tailoring Crystallinity of Electrospun Plla Fibres by Control of Electrospinning Parameters," *Polymers (Basel)*, vol. 4, no. 3, pp. 1331–1348, 2012.
- [64] W. Su, J. Darkwa, and G. Kokogiannakis, "Review of solid-liquid phase change materials and their encapsulation technologies," *Renew. Sustain. Energy Rev.*, vol. 48, pp. 373–391, 2015.
- [65] N. S. Vrandečić, M. Erceg, M. Jakić, and I. Klarić, "Kinetic analysis of thermal degradation of poly(ethylene glycol) and poly(ethylene oxide)s of different molecular weight," *Thermochim. Acta*, vol. 498, no. 1–2, pp. 71–80, 2010.
- [66] B. Rezaei, M. Ghani, M. Askari, A. M. Shoushtari, and R. M. A. Malek, "Fabrication of Thermal Intelligent Core/Shell Nanofibers by the Solution Coaxial Electrospinning Process," *Adv. Polym. Technol.*, vol. 35, no. 1, pp. 1–8, 2016.
- [67] C. Zhang, X. Yuan, L. Wu, Y. Han, and J. Sheng, "Study on morphology of electrospun poly(vinyl alcohol) mats," *Eur. Polym. J.*, vol. 41, no. 3, pp. 423–432, 2005.
- [68] S. Huan *et al.*, "Effect of experimental parameters on morphological, mechanical and hydrophobic properties of electrospun polystyrene fibers," *Materials (Basel)*, vol. 8, no. 5, pp. 2718–2734, 2015.
- [69] H. Jiyong, Z. Yinda, Z. Hele, G. Yuanyuan, and Y. Xudong, "Mixed effect of main electrospinning parameters on the  $\beta$ -phase crystallinity of electrospun PVDF nanofibers," *Smart Mater. Struct.*, 2017.
- [70] P. Sun, G. Liu, D. Lv, X. Dong, J. Wu, and D. Wang, "Effective activation of halloysite nanotubes by piranha solution for amine modification via silane coupling chemistry," *RSC Adv.*, vol. 5, no. 65, pp. 52916–52925, 2015.

- [71] S. Habibi, M. Saket, H. Nazockdast, and K. Hajinasrollah, "Fabrication and characterization of exfoliated chitosan–gelatin–montmorillonite nanocomposite nanofibers," *J. Text. Inst.*, vol. 0, no. 0, pp. 1–6, 2019.
- [72] B. Sharma, P. Jain, and R. Purwar, "Preparation and characterization of poly(vinyl alcohol)/modified clay electrospun nanocomposite nanofibrous mats for microbial protection," *J. Text. Inst.*, vol. 0, no. 0, pp. 1–11, 2019.
- [73] R. Qi *et al.*, "Electrospun poly(lactic-co-glycolic acid)/halloysite nanotube composite nanofibers for drug encapsulation and sustained release," *J. Mater. Chem.*, vol. 20, no. 47, pp. 10622–10629, 2010.



## APPENDICES

### A. THERMAL CYCLIC TEST GRAPHS

Temperature versus time graph and data are given in Figure A.1 and Table A.1, respectively. The temperature versus time data was taken at every 10°C of cooling starting from 150°C to 30°C. The curve was split into 12 linear lines each corresponding to 10°C interval. The slopes of these lines were calculated and the average of these slopes were taken in order to determine a representative cooling rate value throughout the cyclic operation.

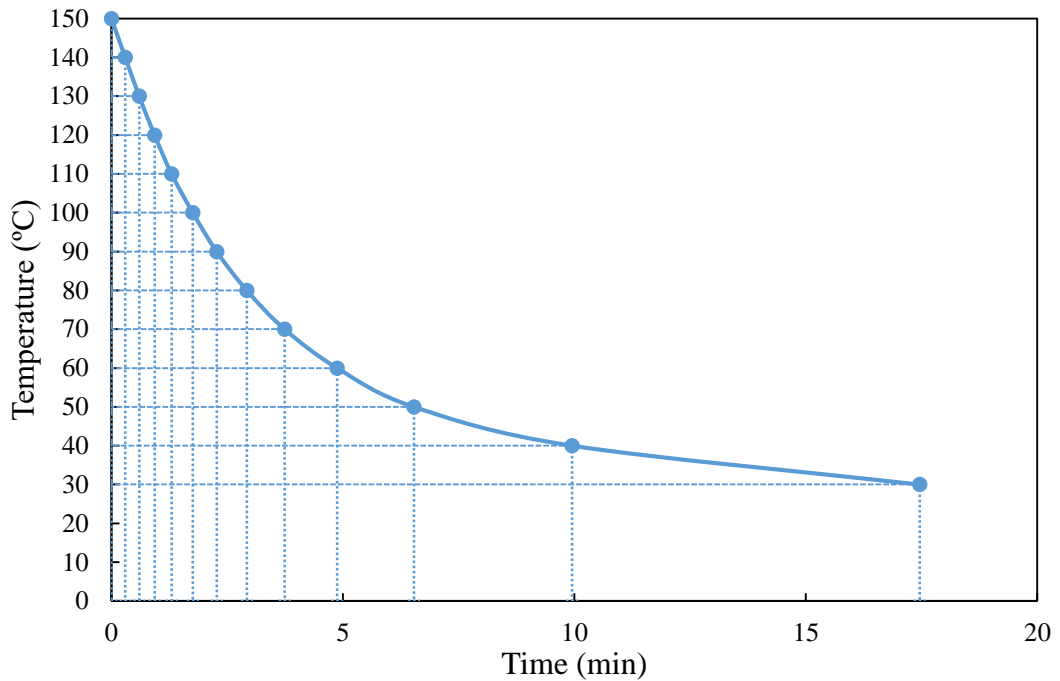


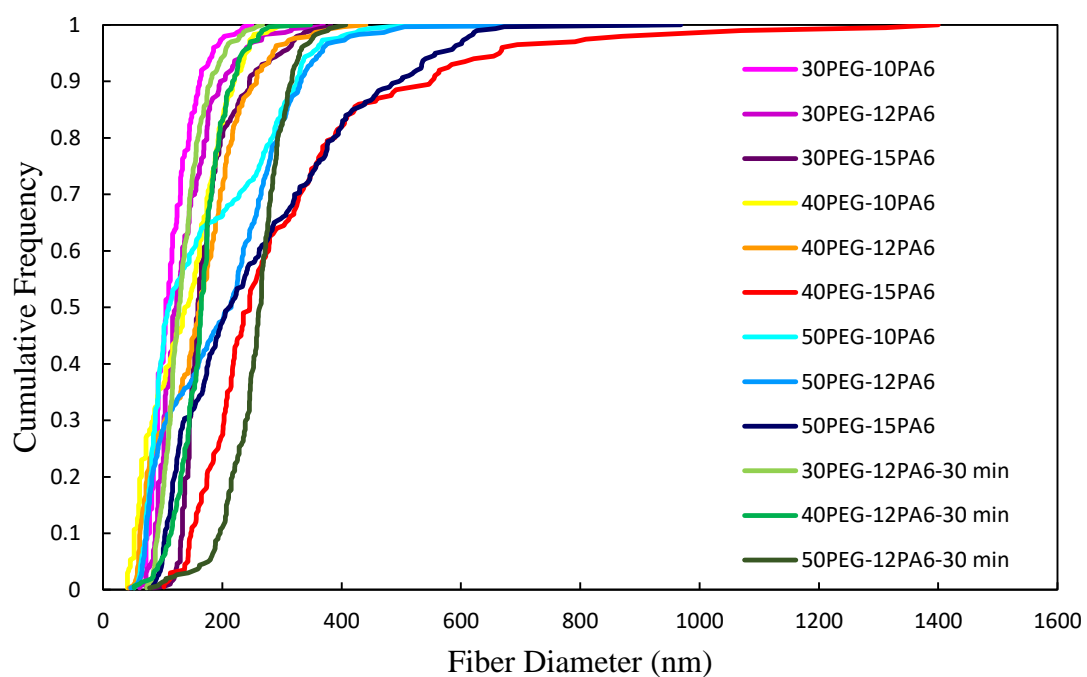
Figure A.1 Representative temperature versus time curve of the cooling samples during thermal cyclic test.

Table A.1 *Representative temperature versus time data of the cooling sample in thermal cyclic test.*

<b>Temperature (°C)</b>	<b>Time (min)</b>
150	0.0
140	0.3
130	0.6
120	0.9
110	1.3
100	1.8
90	2.3
80	2.9
70	3.7
60	4.9
50	6.5
40	10.0
30	17.5

## B. FREQUENCY DISTRIBUTION GRAPHS

Frequency distribution graphs of the data obtained from every average fiber diameter measurement were drawn in order to depict the diameter distribution of the fibers throughout the specimens more clearly. Frequency distribution graph of data from solution concentration optimization, applied electrical potential optimization, solution feed rate optimization and composite nanofiber development experiments are given in Figures B.1, B.2, B.3, B.4, respectively.



*Figure B.1* Fiber diameter frequency distribution graph of the samples produced with different solution concentrations.

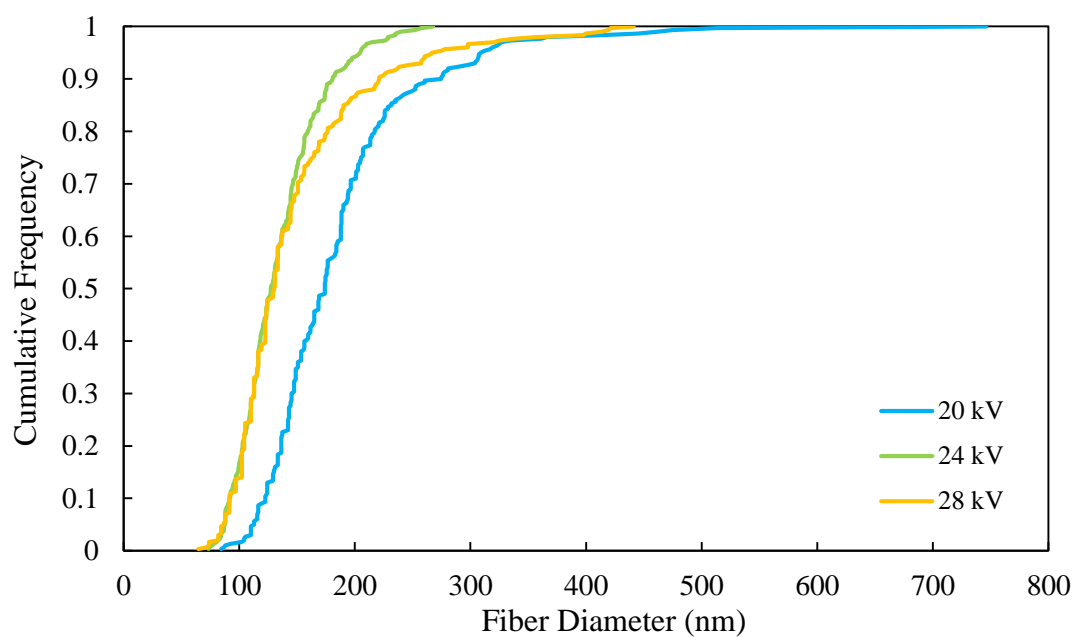


Figure B.2 Fiber diameter frequency distribution graph of the samples produced under different applied electrical potentials.

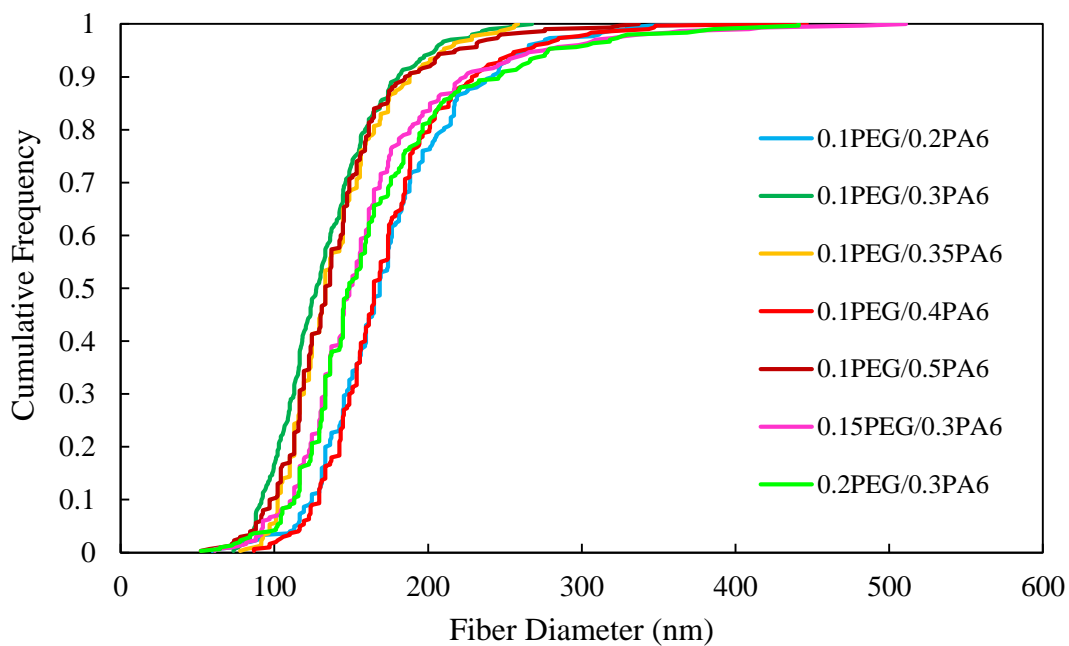


Figure B.3 Fiber diameter frequency distribution graph of the samples produced with different core/shell solution feed rates.

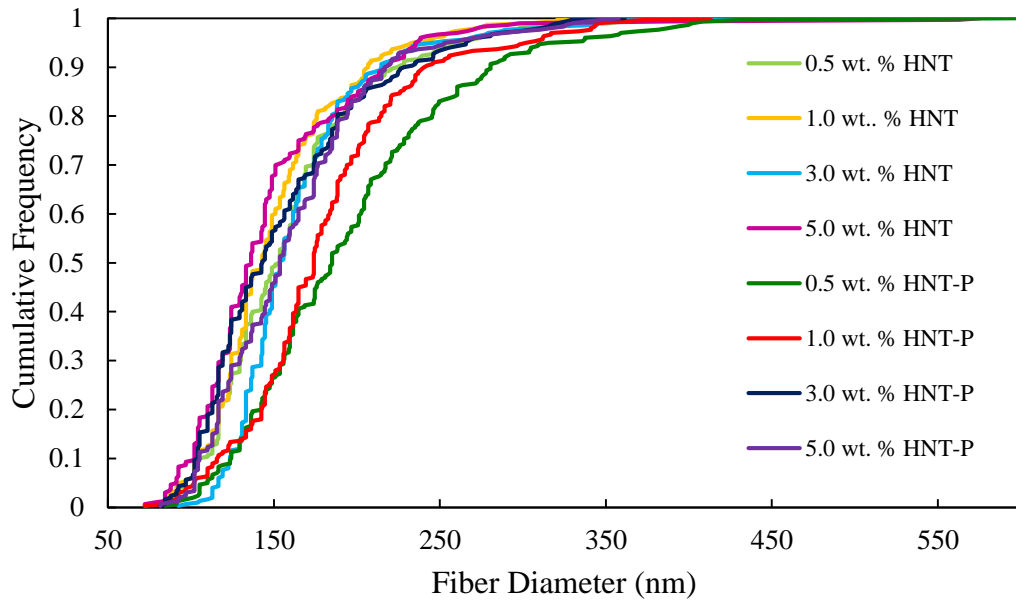


Figure B.4 Fiber diameter frequency distribution graph of the samples produced with different amount of HNTs and HNT-P addition.

### C. TENSILE TEST RESULTS

Table C.1 *Tensile test results of the electrospun nanofibrous samples.*

<b>Sample</b>	<b>Tensile Strength (MPa)</b>	<b>Tensile Modulus (MPa)</b>	<b>Elongation at Break (%)</b>
Neat PA6 Fibers	7.9 ± 1.1	88.5 ± 13.0	46.1 ± 3.0
Neat Core/Shell Fibers	7.6 ± 0.3	91.5 ± 4.1	43.3 ± 3.9
0.5 wt. % HNT	7.5 ± 0.2	90.0 ± 7.7	46.9 ± 3.8
1.0 wt. % HNT	7.5 ± 0.6	92.2 ± 0.7	41.7 ± 4.1
3.0 wt. % HNT	7.2 ± 0.5	98.8 ± 4.3	39.8 ± 6.0
5.0 wt. % HNT	7.4 ± 0.5	74.0 ± 7.0	39.2 ± 3.6
0.5 wt. % HNT-P	7.0 ± 0.5	105.2 ± 5.7	46.7 ± 5.1
1.0 wt. % HNT-P	7.3 ± 0.3	117.4 ± 6.2	40.2 ± 1.8
3.0 wt. % HNT-P	7.8 ± 0.1	115.7 ± 5.7	49.4 ± 1.9
5.0 wt. % HNT-P	7.8 ± 0.7	111.6 ± 16.9	35.2 ± 3.7